Mathematical Modelling of the Electrical and Mechanical Properties of Cardiac Cells Coupled with Non-Muscle Cells

Peter Bliss Mortensen

Submitted in fulfilment of the requirements for the
Degree of Doctor of Philosophy

Institute of Cardiovascular and Medical Sciences
College of Medical, Veterinary and Life Sciences
University of Glasgow

January 2021

Abstract

The heart is arguably the most important organ in the body. It works tirelessly every minute of our lifespan, supplying blood throughout the body, with maximum efficiency. The heart is composed of a large number of distinct cell phenotypes that are coupled together and interacting via a complex system of electrical and mechanical processes. The work in this thesis explores the interactions between cardiac cells, and how these interactions and connections impact both the mechanical and electrical behaviour of the heart. Specifically, novel results on three distinct research projects are presented.

Firstly, a mathematical model of contractile units, coupled in series and suspended between two springs, is constructed. This was done to investigate a problem posed by experiments, in which monolayers of cardiomyocytes were cultured onto substrates with a range of stiffnesses. It was discovered that the stiffness of the substrate impacts the nature of the contraction in the cells. In particular, on soft substrates, like a flexible hydrogel, the cells can contract freely with a regular motion. However if the substrate is stiff, like glass or plastic, multi-peaked behaviour in the recorded motion of the cells appears. The mathematical model of this system confirms that the substrate stiffness is in fact the cause of the multiple peaks in the contraction profiles, but also highlights that when many contractile units are coupled in a chain the contraction of the unit is dependent on its position within the chain.

The second piece of research presented coupled electrophysiology models of cardiomyocytes and fibroblasts. This work explores action potential propagation as a function of the fundamental patterns of fibroblast density that appear in fibrotic regions, and how these patterns and the fibroblast density can result in the failure of the action potential propagation. Primary action potential biomarkers including: conduction velocity, peak potential and triangulation index are estimated from direct numerical simulations. Through these simulations, it is shown that the action potential propagation is blocked by the fibroblast density and the pattern of their distribution. This work also investigates how these results are affected by the differentiation between fibroblasts and myofibroblasts. Furthermore, the asymptotic separation of fast and slow time scales, that are typical in electrophysiological models, is exploited to estimate the threshold number of fibroblasts per myocyte that will allow propagation.

The final research project explores a problem presented by experiments which co-cultured human induced pluripotent stem cell derived cardiomyocytes (hiPSC-CM) with human embryonic kidney cells (HEK cells). In particular, this work addresses the question of, if the cells were cultured together and the HEK cells were expressing the inward rectifying current, can the spontaneous activity of the hiPSC-CM be suppressed? To this end, a novel model of the HEK cell electrophysiology was coupled with an electrophysiology model of the hiPSC-CMs. This work shows that the coupling of the cells can cause the spontaneous nature of the hiPSC-CM to fail as hypothesised in the original experiments. Specifically, coupling the cardiomyocytes with HEK cells that are expressing the inward rectifying current, I_{K1}, increases the time between individual

action potentials, known as the cycle length, in comparison to the system with wild type HEK cells coupled with the cardiomyocytes. Also, the spontaneous activity is stopped entirely when sodium current of the cardiomyocytes is adjusted.

The ultimate aim of this work is to outline the significance of intercell interactions that appear in cardiac tissue and that these interactions must be considered to properly model cardiac behaviour. As well as elucidating significant details of cell behaviour, all three pieces of work show that if these interactions are imbalanced, the primary function of action potential propagation or muscle contraction can be affected to the extent of failing to perform.

Acknowledgements

I would like to thank my supervisors, Dr Radostin Simitev, Prof Godfrey Smith and Dr Hao Gao. You have been a constant source of guidance and patience. I have really enjoyed my PhD and it would not have been possible without you.

To the whole SofTMech team, I want to thank you not only for your generous funding, but also for providing me with inspiration and irreplaceable experiences that will last a lifetime.

Thank you, to my fellow PhD students, for your reassurance, especially those who were always available for a cup of tea and a rant.

To Mum & Dad, thank you for all your help and encouragement over all these years of study. Without you it would not have been possible and I would not be where I am today.

Finally, to Grant, thank you for your support in the fight against Titivillus and for always keeping me laughing, especially when things seemed impossible.

Contents

Abbreviations

AP	Action Potential
APA	Action Potential Amplitude
APD_{90}	Action Potential Duration, at 90% repolarisation
AV node	Atrioventricular node
BCL	Basic Cycle Length
CL	Cycle Length
CM	Cardiomyocytes
CRN	Courtemanche-Ramirez-Natel
CV	Conduction Velocity
DNSs	Direction Nnumerical Simulations
ECM	Extracelluar Matrix
EP	Electrophysiological
EM	Electromechanical
HEK cells	Human Embryonic Kidney cells
HEK-WT	Wild Type HEK cells
HEK-K1	I_{K1} expressing HEK cells
hiPSC-CMs	Human induced pluripotent stem cell-derived cardiomyocytes
IV curve	Current-Voltage Curve
LV	Left Ventricle
ODE	Ordinary Differential Equation
PDE	Partial Differential Equation
RC	Resistor-Capacitor
SA node	Sinoatrial node
SL	Sarcomere Length
SNR	Signal to Noise Ratio
TCP	Tissue Culture Plastic

List of Figures

List of Tables

Declaration

The work presented in this thesis is the work of the author. Anything that is the published work of others is clearly attributed.

Novel research is carried out in Chapters 4, 6, 7, and 8. This work has utilised and adapted generated computer code from the online repository of biological systems in the Physiome Project https://models.physiomeproject.org/.

Published Works

The methods discussed in Chapter 5 are published in the conference proceedings of the 6th European Conference on Computational Mechanics (ECCM 6), Mortensen et al. [64].

The results in Chapters 6 and 7 have been peer-reviewed and published in the Journal of Mathematical Medicine and Biology, Mortensen et al. [65].

Chapter 1

Introduction

The heart is arguably the most important organ in the body. Through a complex system of electrical and mechanical processes, that are all coupled together, the heart works tirelessly to supply blood throughout the body, with maximum efficiency. These processes rely on interactions between the various cells that appear in cardiac tissue. It is these intercell interactions, and how they impact the function of the cells, that will be the focus of the work presented in this thesis. The intercell interactions are investigated through the use mathematical models of the electrical and mechanical processes of cardiac cells that have been coupled together. Particularly, the impact of these interactions are explored in three novel pieces of work which have been performed as follows.

1. **Cardiomyocyte Contraction when Attached to a Substrate:** Mechanical models of sarcomere contraction are coupled in series and suspended between two springs, to model a problem presented by a set of experiments in which a monolayer of cardiac muscle cells are cultured on various substrates [41]. This investigated if the contraction of the system was affected by the substrate stiffness.

2. **Action Potential Propagation with Coupled Myocytes and Fibroblasts:** Myocyte and fibroblast electrophysiology models are coupled to investigate how the pattern and density of the fibroblast distribution in fibrotic tissue does or does not affect the propagation of the action potential in cardiac tissue. These results have been published in Mortensen et al. [65]. This work also looks at the differences in the electrophysiology of fibroblasts and myofibroblasts.

3. **Human Induced Pluripotent Stem Cell Derived Cardiomyocytes Coupled with Human Embryonic Kidney Cells:** Human induced pluripotent stem cell derived cardiomyocytes (hiPSC-CM) are coupled with a novel model of human embryonic kidney cells (HEK cells) to explore a problem presented by Costa et al [17], in which hiPSC-CM are co-cultured with HEK cells, in an effort to overcome the spontaneous character of these particular cardiomyocytes.

When addressing these questions, there are many complex systems in cardiac tissue that must be considered. Chapter 2 is dedicated to introducing all the crucial background of the biological systems at play, that is required to begin to mathematically model cardiac tissue and the relevant cell interactions. In this chapter, the function of the heart is described, with a focus on the myocardium and its cells. In particular, myocytes, fibroblasts and their electrical and mechanical processes. This chapter also discusses heart failure, and the impact heart failure has on cardiac function, as well as the process of fibrosis.

1.1 Project 1: Cardiomyocyte Contraction on a Substrate

The first piece of novel work constructs a mathematical model of a monolayer of cardiomyocytes on a substrate. This was done in order to model a problem presented by the work performed by Huethorst et al. [41]. This work asks the question, is the contraction of the cardiomyocyte monolayer impacted by the substrate stiffness?

Models of muscle contraction, or more specifically models of sarcomere contraction, are introduced in Chapter 3. This involves discussion of the various steps of the contraction process and their formulation, with a particular focus on the Rice model [88]. It is this model of the sarcomere contraction that is adapted in the novel model that is used in Chapter 4. To construct the model of the cardiomyocyte monolayer the Rice model is coupled to form a chain of contracting units, using a coupling scheme based on work by Timmermann et al. [116]. This scheme defines each unit's change in length to be dependent on their own internal mechanisms and the length changes of the adjacent units.

The work by Huethorst et al. [41], is concerned with the contraction of monolayers of hiPSC-CM and recorded the motion of these cardiomyocytes when they are cultured on a rigid substrate, for example glass or plastic, or a flexible substrate like a hydrogel, and substrate-free cultures. These experiments found that spatio-temporal features of hiPSC-CM contraction are dependent on the rigidity of the substrate that the monolayers of hiPSC-CMs are attached to. Specifically, it was found that if a monolayer of cardiomyocytes is attached to a rigid substrate, the contraction of the monolayer shows multi-peaked behaviour, meaning that multiple peaks appear in the motion of contraction. However, if the monolayer is substrate-free or attached to a flexible substrate, the number of contraction traces with multiple peaks is significantly reduced. These phenomena are summarised in Figure 1.1.

By constructing a chain of contracting units and defining the two units at the ends of the chain as simple springs, a simple model of the monolayer of cardiomyocytes on a substrate is produced. The springs on the either end of the chain represent the attachments to the substrate, and has a spring constant that is varied to reflect the changes in the substrate stiffnesses. Using this model the length changes of the units and the positions of the unit ends are explored. The model successfully exhibits the key behaviour of the experiments, namely an increase in the

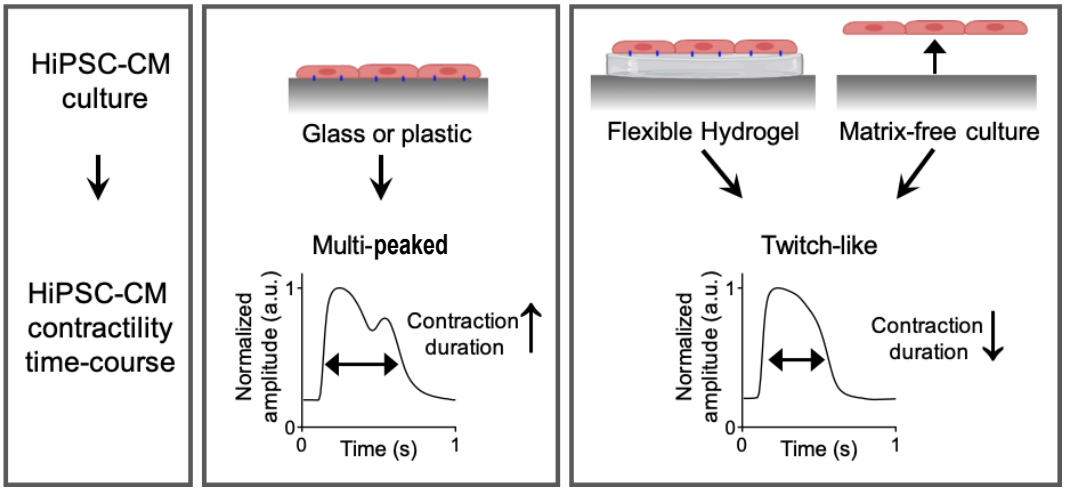

Figure 1.1: A summary of the motion time courses of cardiomyocyte monolayers as seen on the different types of substrate from Huethorst [41]. With the second panel showing if the human induced pluripotent stem cell derived cardiomyocytes (hiPSC-CM) are cultured on a stiff substrate (glass or plastic), then multi-peaked behaviour is seen in the normalised amplitude of the motion recordings of the cell cultures. The third panel shows that if the hiPSC-CM are cultured on a flexible substrate, like a hydrogel, the multi-peaked behaviour is not seen in the motion recordings.

prevalence of multi-peaked behaviour as the spring constant increases. This work confirms that the substrate stiffness is directly linked to the multi-peaked behaviour. It also sheds light on possible mechanisms at play in regular muscle tissue, specifically that if the chain of contracting units is too long waves appear in the chain, which do not appear in muscle tissue.

1.2 Project 2: Action Potential Propagation with Coupled Myocytes and Fibroblasts

The latter half of this thesis focusses on mathematical models of electrophysiology. Starting in Chapter 5, in which mathematical models of cardiac electrophysiology are introduced. Here the types of ion channels and their formulation are discussed, as well as specific features of myocyte models, and a summary of the monodomain model and its derivation. This chapter also includes details of the numerical methods used to solve the EP models in question. There is then a discussion of the types of coupling that can be utilised at a tissue level, particularly the differences between “attachment" models and “insertion" models.

The second project presented in this thesis couples electrophysiological models of cardiomyocytes and fibroblasts, and asks, does the pattern and density of the fibroblast distribution in fibrotic cardiac tissue affect the action potential propagation? This work is presented in Chapters 6 and 7 and was published in the paper Mortensen et al. [65].

There has already been extensive work on mathematical modelling of the coupling of my-

ocyte and fibroblast electrophysiology. Namely, work by Kohl et al. [50] and MacCannell et al. [52] coupled myocyte EP models with passive and active fibroblasts EP models, respectively. These two models of the coupled myocyte and fibroblast cells are the basis of many subsequent myocyte-fibroblast models. Through these models and newer models, the importance of the intercell connections has been explored at the single cell level, showing significant impacts of the action potential. There has also been extensive work at the tissue level.

When cardiac tissue is damaged the process of fibrosis takes place in order to repair the myocardium. This fibrosis process causes an increase in the number of fibroblasts in the system, which produce collagen to repair the damaged tissue. However, the repaired region can cause arrhythmia. These arrhythmogenic properties of fibrotic tissue have been previously explored, using 2D slabs with spiral waves [68, 106]. Sridhar et al. [106] coupled myocytes and fibroblasts to show how increasing the conductance of the L-type calcium channel increases arrhythmogenesis. As well as fibroblasts, they also model myofibroblasts, which are distinguished by having an increased cell capacitance and an increased uncoupled diastolic potential. Nayak et al. [68] use a passive model to show that as the intercell conductance (or coupling strength) is increased, the AP plateau amplitude decreases and the resting potential increases. They also show that if the number of coupled fibroblasts increases the resting potential and action potential duration (APD) decrease. They also show that if the number of coupled fibroblasts is too high the AP can not be generated and autorhythmic properties or oscillatory behaviours appear.

Beyond single-cell EP dynamics and 2D spiral waves, more realistic 3D geometries of atria have also been studied [62, 63]. In the study by Morgan et al. [62] they compare the arrhythmogenic properties of fibrosis and ionic remodelling as well as the combination of these two features and investigate the corresponding changes in action potential wave length. To model fibrosis they coupled the Courtemanche, Ramirez and Nattel model of human atrial myocytes [16] (referred to as the CRN model) and developed the fibroblast model by MacCannell et al. [52] to be specific to atrial fibroblasts. They showed an increased number of fibroblasts also decreases the wave length. In the paper by Morgan et al. [63] they consider four causes of atrial fibrillation: 1) ionic remodelling [15], 2) uniform myocyte-fibroblast coupling 3) uniform myocyte-fibroblast coupling with increased tissue anisotropy and 4) patchy fibrosis defined by patient specific atrial fibrosis. In the first three cases atrial fibrillation-like patterns were only seen in the case with combined myocyte-fibroblast coupling and increased anisotropy. The patient specific fibrosis case shows evidence again of sustained rotors seen in atrial fibrillation patterns.

These pieces of work are important, however they overlook the patterns that appear in the fibrotic tissue. In previous work the fibroblasts are either randomly or uniformly distributed, or there is a complex patient specific pattern, which are too complicated to inform on how the pattern of fibrosis is related to the changes in behaviour. The work presented in Chapter 6, addresses this gap in the understanding relating to the pattern of the fibroblast distribution

and how it impacts the action potential propagation. This work highlights three fundamental patterns of fibrosis, namely: uniform fibrosis, a fibrotic barrier and a myocyte strait. Each case highlighted that successful action potential propagation is dependent on both the fibroblast density and pattern of the fibrotic regions.

This chapter is then followed by Chapter 7, which discusses the fast and slow subsystems of the myocyte-fibroblast monodomain model. These subsystems can be exploited to reduce the model and find analytical solutions that shed light on the problem of AP propagation in the presence of fibroblasts, and it is shown that it is possible to find a good prediction of the threshold number of fibroblasts that will stop the propagation to a reasonable accuracy. Both of these chapters also consider the how differences between fibroblasts and myofibroblasts impact the AP propagation.

1.3 Project 3: Human Induced Pluripotent Stem Cell Derived Cardiomyocytes Coupled with Human Embryonic Kidney Cells

As discussed, there has been extensive work done analysing the effects of the intercell coupling of myocytes and fibroblasts at the single-cell level. However, this is not the only intercell EP relationship of interest. In the final piece of work, in Chapter 8, a model of the electrophysiology of human induced pluripotent stem cell derived cardiomyocytes (hiPSC -CMs) is coupled with a novel EP model of human embryonic kidney cells (HEK cells). This was done in an effort to investigate the problem presented in work by A. da Silva Costa et al [17], which, in an attempt to overcome the spontaneous nature of the hiPSC-CM, co-cultured with HEK cells, both the wild-type cells and HEK cells that are expressing I_{K1}. This work aimed to answer, why has the spontaneous activation not been overcome? And under what conditions can spontaneous activation be suppressed?

Human iPSC-CMs have the potential to be used as an alternative to cardiomyocytes taken from animal tissue, in a range of fields, for example pharmatoxicity and regenerative medicine [9, 13, 39, 57, 60, 119]. A key feature of hiPSC-CMs is the spontaneous electrical activity which is considered to be an immature electrical phenotype [5, 39]., rather than waiting to be triggered by an external stimulus, like with an adult ventricular cardiomyocyte. This is due to the presence of the pacemaker (or funny) current, I_f, [119] and a lack of the inward rectifying current, I_{K1}, [39, 40, 119], which maintains a stable resting transmembrane potential [22, 40]. With a normal adult level of expression of inward rectifier the resting potential is held close to the equilibrium potential of K^+ (EK) [31].

The work done by Costa et al [17] developed an experimental model, co-culturing a partner cell (HEK cell) to the culture, coupling them with the cardiomyocytes. This work found that

coupling to wild type HEK alone caused APD shortening. Coupling the cardiomyocytes to HEK cells expressingI_{K1} (HEK-K1 cells) caused further shortening, although not in the APD_{90}. It was also shown that the presence of the HEK-K1 cells caused the cycle lengths to increase, and although the cells are less excitable, the spontaneous nature of the hiPSC-CM was not stopped entirely. A mathematical model has been created to see if this phenomena can be explained.

The coupling of electrophysiology models of hiPSC-CMs and HEK cells does not occur in the literature. There is an established model of the hiPSC-CM, by Paci et al [75] and is commonly used to simulate the hiPSC-CM and successfully models the spontaneous nature of the cells. However, there is no EP model of HEK cells, and thus using established forms of EP models and published data, from Thomas and Smart [112] and de Boer et al. [20], an EP model of the wild-type HEK cells and HEK cells expressing I_{K1} was derived. This coupled system recreates the key features of the problem and also sheds light on the cause of some of these features.

1.4 Aims

There are many advantages to using mathematical modelling to explore the nature of biological processes, which are highlighted in the novel work presented in this thesis. First of all, once a mathematical model is constructed, it is a fast and cost effective method of conducting research. Another benefit of mathematical modelling is that it gives valuable insight into measurements of mechanisms that are not always available experimentally, which can in turn inform the direction of future experimental research. Finally, a mathematical model is a non-invasive way to explore a biological process thus reducing the necessity for expensive and dangerous surgeries, or repetitive animal testing. Beyond research, mathematical models are also considered to be the future of medical treatment, as they can allow clinicians to see the long term outcomes without waiting and thus treat patients early to reduce long term problems. For all these reasons, it is very exciting to be part of this innovative and necessary research.

The ultimate aim of this work is to outline the significance of intercell interactions that appear in cardiac tissue and that these interactions must be considered to properly model cardiac behaviour. Both electrophysiological and mechanical models are used in the work presented. As well as informing on the nature of the cells' behaviours, all three pieces of work show that if these interactions are imbalanced the primary function of AP propagation or muscle contraction can be affected to the extent of failing to perform.

Chapter 2

Biology of The Heart

In this chapter, the function of the heart is described, with a focus on the myocardium and its cells. In particular, myocytes, fibroblasts and their electrical and mechanical processes. This chapter also discusses heart failure, and its impact on cardiac function, as well as the process of fibrosis.

2.1 Introduction

Arguably the most important organ in the body, the heart works continuously to supply nutrients to the whole body. The heart is comprised of four chambers; two atria and two ventricles, as well as numerous valves separating the chambers and blood vessels. Figure 2.1 shows the anatomy of the heart.

The blood is pumped through the heart with maximum efficiency. To achieve this efficiency the heart beats with a particular pattern. Starting at the sinoatrial node (also known as the pacemaker of the heart) in the right atrium, an electrical wave is stimulated and passes across the atria until is reaches the atrioventricular node (AV node) at the top of the septum. This causes the muscle cells of the atria to contract, expelling the blood out of the atria and into their respective ventricles. The AV node momentarily slows the electrical signal before passing it down the purkinje fibres in the septum of the heart, to the apex, and finally up and around the outside of the ventricles. Again, as the electrical signal passes through the tissue, the muscle contracts, forcing the blood out of the ventricles and out of the heart.

The right ventricle and atrium receive deoxygenated blood from the body and pumps the plump to the lungs to become reoxygenated. The oxygenated blood then returns to the heart and specifically into the left atrium and then the ventricle, which then pumps it to the rest of the body. Since the left half of the heart has to pump the blood at high pressures, the left ventricle is much bigger and stronger than the right.

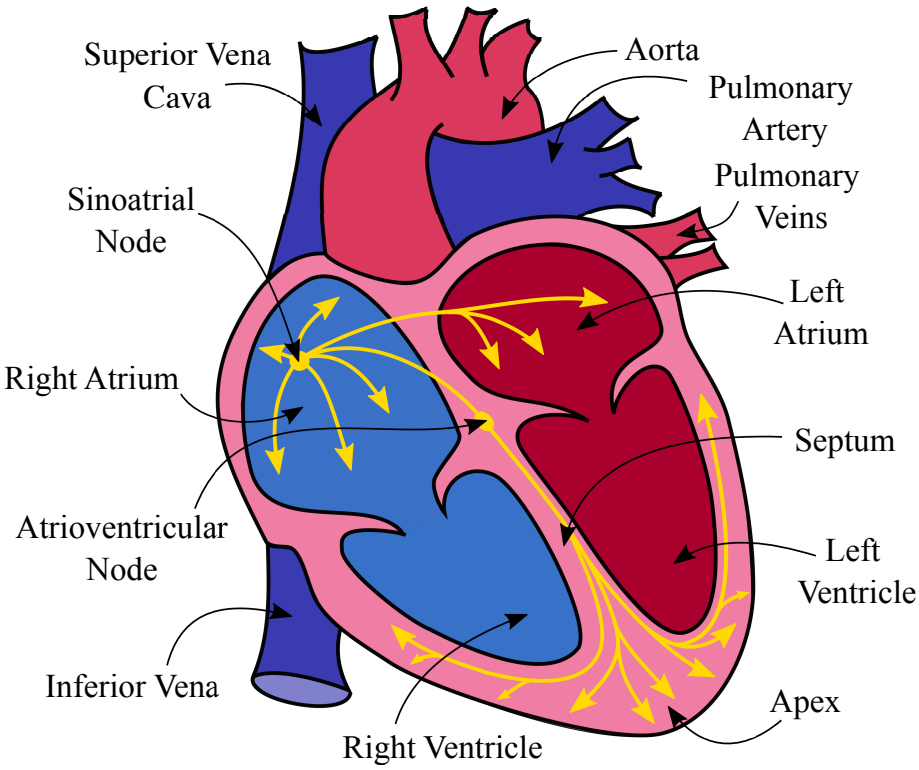

Figure 2.1: Anatomy of the heart.

2.2 Cardiac Tissue

The ventricular and atrial walls both have three key layers. The middle layer is the myocardium, which makes up the majority of the heart wall, and the epi- and endocardium, which are much thinner than the myocardium and are found on the outside and inside of the heart wall, respectively [55]. The myocardium contains numerous types of cell: myocytes, fibroblasts, endothelial cells and vascular muscle cells [77, 104]. By volume, the tissue is comprised of approximately 75% myocytes. However, the number of myocytes only make up 30% of the total number cells. The remaining 90% of cells are fibroblasts [10, 14]. Intercell connections are formed between these two types of cells, as well as between cells of the same type [49]. These cells are then surrounded by the extracellular matrix (ECM) which supports the cells and gives the tissue its structure and shape, and aids in mechanical, electrical and chemical signals [8]. This structural part of the ECM, in which the cells reside, is made up of collagen and elastins [91] assuring contraction is in the correct direction and the myocytes work together and not against one another. However, as well as structure, the ECM also accommodates growth factor and cellular receptor-binding properties [91].

2.2.1 Myocytes

Myocytes are muscle cells and there are three types: smooth, skeletal and cardiac. Naturally, this work will focus on cardiac myocytes, also referred to as cardiomyocytes. The size and shape of

cardiomyocytes can vary greatly, and can even include branches, but generally they are longer in the force direction, with a length of 50-200μm and a width of 10-40 μm [2]. Within the myocyte there is a range of organelles, such as the nucleus, the sarcomeres, the sarcoplasmic reticulum, and mitochondria. The sarcomeres are the contractile units and account for a majority of the mass and are surrounded by the sarcoplasmic reticulum, which stores Ca^{2+} ions. The process by which the sarcomeres contract is a cycle that starts with the electrical stimulation of the myocyte. When sufficiently stimulated, the cardiomyocytes are depolarised, creating a change in the transmembrane potential with has a particular profile, known as an action potential (AP) [107].

The stimulation of the myocyte triggers a release of calcium ions from the sarcoplasmic reticulum into the cytoplasm of the myocyte (or the sarcoplasm). These calcium ions then bind to filaments in the sarcomeres that dis-inhibits the interaction between contractile filaments of the sarcomere allowing generation of active force and contraction of the myocyte. This process will be discussed further in Section 2.5.

Human-induced Pluripotent Stem Cell Derived Cardiomyocytes

An interesting and relevant type of cardiomyocyte is the human induced pluripotent stem cell derived cardiomyocyte (hiPSC-CM). This cardiomyocyte is derived by inducing stem cells to create cardiomyocytes, rather than extracting them from animal or human tissue. There are numerous advantages to deriving cardiomyocytes from stem cells. Firstly, they are far more accessible than regular human cardiomyocytes. They can also be transplanted into patients without the risk of rejection [61]. This makes them desirable for ex-vivo experimentation. However, some key features are considered to be immature, such as the fact that hiPSC-CMs spontaneously activate, rather than being stimulated by an external trigger. Human iPSC-CMs are explored further in Chapter 8, in which they are co-cultured with human embryonic kidney cells, in an attempt to overcome this behaviour.

2.2.2 Fibroblasts

Fibroblasts produce the collagen and the extracellular matrix. In healthy tissue, fibroblasts actively maintain this collagen matrix, but they are not electrically inert. Like myocytes, fibroblasts can conduct electricity. However, unlike myocytes, the electrical response is electrotonic, rather than active. Meaning, that when the fibroblast is stimulated, the depolarisation does not create an action potential, rather the potential simply decays away once the stimulation has ended. Fibroblasts create intercell connections with myocytes and thus their electrical behaviour are undoubtedly linked. Examples of the intercell connections in cardiac tissue are seen in Figure 1, in work by Kohl and Camelliti [49] which shows immunolabeling of myocytes, fibroblasts and their gap connections, specifically in a rabbit atrium. This paper also shows examples of the

same connections appearing in the ventricles and AV node.

Fibroblasts in healthy tissue have the ability to differentiate themselves and become myofibroblasts [118]. Myofibroblasts differ from fibroblasts in that they are much bigger and express smooth muscle cell actin [3]. The process of differentiation can occur when the heart must repair itself if it has been damaged through some form of heart failure.

2.3 Cellular Electrophysiology

Electrophysiology is the study of the electricity that passes through the body, by way of the movement of ions. For example, electricity passes through neurons in the brain and through muscle tissue. This work will focus on the electrophysiology of cardiac tissue. More specifically, the electrophysiology of the key electrically conducting cells in the myocardium and how these cells interact.

The cell membrane is said to be selectively permeable, meaning only certain ions can pass through it. This allows the cell to maintain its internal environment. The wall of the membrane is comprised of a double layer of phospholipids whose heads face outward and are hydrophilic and the tails are within the structure and are hydrophobic. Throughout the membrane wall are proteins that can move within the wall and channels which allow passage through the wall of certain molecules. An image of the cell membrane can be seen in Figure 2.2.

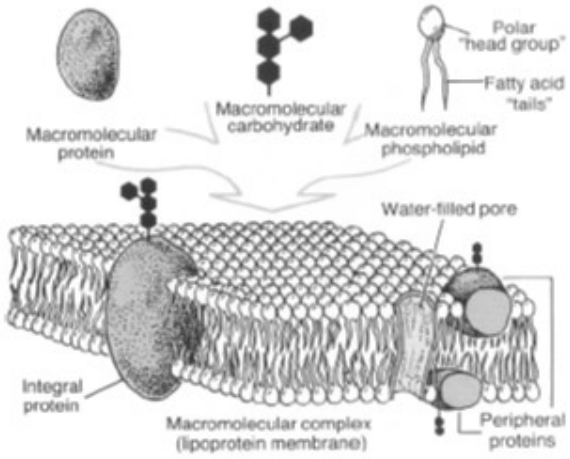

Figure 2.2: The cell membrane, from Keener and Sneyd [45].

Some of these channels are ion channels, which allow ions to cross the membrane either actively or passively. Active processes expend energy, whereas passive processes do not, but rather rely on osmosis. The concentration differences of the ions that arise across the cell membrane creates a difference in potential over the membrane, as they are, by definition, charged particles. It is this potential difference caused by the flow and movement of the ions that is studied in electrophysiology.

2.3.1 Cardiomyocyte Action Potential Dynamics

The function of cardiomyocytes is dictated by the dynamics of the action potential, which is in turn dictated by the altered membrane permeability and changes in ionic current flow. The movement of ions is powered by the chemical potential and the electrical potential. The cardiomyocyte operates with three types of ion: sodium ions, potassium ions and calcium ions. However, there are more than 3 channels for these ions. The number of channels and their variety is dependent on the species and if it is in the atria or ventricles. There is also a range of ion transport systems and complexities. Most channels simply move a single ion across the membrane and is dictated by the chemical potential. Whereas others can exchange one type of ion for another or act as a pump working against the chemical potential. Also, within the cardiac myocytes have subregions and organelles that themselves have ion channels, for example the sarcoplasmic reticulum and the mitochondria.

These ion channels each are involved in controlling a different part of the action potential. The movement of the ions is driven by two means, the chemical potential and the electrical potential. There are 5 phases of the action potential, as seen in Figure 7.1 in the book Computational Cardiology, by Sachse [94]. Initially, the action potential is at rest, the calcium and sodium channels are minimally active, while the potassium rectifying currents keep the transmembrane potential at its rest state. Then, when the myocyte is activated by an adjacent cell (either a myocyte or pacing cell), the action potential enters its second phase. There is a depolarisation that causes an increase in the sodium channel permeability, which increases the transmembrane potential to its maximum value before the channel inactivates, entering the third phase of early repolarisation. In the early repolarisation phase, potassium channels open allowing an increase in membrane permeability to potassium, reducing the transmembrane potential. The next phase is the plateau phase, during which there is movement of calcium and potassium ions which hold the transmembrane potential approximately constant. It is this change in calcium that triggers the release of more calcium from the sarcoplasmic reticulum which can then bind with filaments in the sarcomere and the muscle contraction process can take place. Once the plateau phase ends, the system enters its final phase. During which calcium channels inactivate and delayed rectifier potassium channels stay open to repolarise the cell membrane and the cell returns to the initial state [94].

2.4 Calcium Storage and Release

The electrical and mechanical processes of cardiac tissue are intrinsically linked through the concentration of the calcium ions. The uptake, storage and release of the calcium ions not only are crucial in maintaining the action potential profile, but also in the process of muscle contraction. Out side of the cell the calcium concentration is much higher, which allows the cell open its calcium channels in its membrane and letting the calcium ions to cross the membrane passively

and dramatically increasing the internal calcium concentration. However, since the external calcium concentration is much higher, energy must be expended to maintain the lower calcium ion level. The calcium ions leave the sarcoplasm of cardiomyocyte by either pumping the calcium back out through the membrane, or pumping the calcium ions internal compartments, like the mitochondria or the sarcoplasmic reticula [45].

As mentioned in Section 2.3.1, during the action potential, the calcium ions play a role in maintaining the plateau region. When the cell is activated the increase in calcium in the cytoplasm triggers the ryanodine receptors releasing the stored calcium ions, dramatically increasing the calcium ion concentration in the sarcoplasm, often referred to an “explosion". These calcium ions can then attach to the myofilaments, facilitating the contraction of the myocyte (which is described in more detail in the Section 2.5). Then once the contraction is complete the calcium ions detach from filaments and either leave the cell via the membrane or are pumped back into the sarcoplasmic reticulum [45]. This process of calcium transport in myocytes is depicted in Figure 1 in the review by Bers [4].

2.5 Crossbridge Formation and Muscle Contraction

The process of myocyte contraction is complex, but also crucial in accurately modelling the behaviour of said myocytes. The contraction occurs in the contractile units called sarcomeres which are made of myofilaments known as the thin and thick filaments. The thin filaments are themselves made up of three proteins called actin, troponin and tropomyosin. The thick filament is made up of proteins called myosin which, when permitted, form bonds (or crossbridges) with the actin and pull the two filaments together and contract the cell. However, there are many mechanisms that control whether this process can take place or not.

The system by which the sarcomeres contract is initiated when calcium ions are present in the sarcoplasm, they can bond to the troponin complexes on the thin filament. This exposes the binding sites where myosin can bond to create crossbridges. Once the myosin are bound to the actin the myosin rotates from a perpendicular position to a bent position, moving the thin and thick filaments past one another, in a move called the power stroke [45]. When the rotation is over the myosin detaches from the actin, returns to its pre-rotated state, and either forms another bond to pull the filaments further or the calcium ions have started to detach from the thin filament and leave the sarcoplasm again and the contraction is over and the sarcomere is pulled apart and restored to its initial position and length. This restoration is done, in part by the external pressures on the cell, but also internal structures called titin, which hold the sarcomere in place. This process is illustrated in Figure 3.4.

2.6 Heart Failure

In short, heart failure is the state in which the heart is unable to function as effectively as it should and can have various causes [12, 27] and is the leading cause of death in the western world [18]. In 2012 it was estimated that worldwide, there 26 million patients with heart failure, costing an estimated £22.5billion [98]. In the average middle-aged man or woman, there is an annual incidence of over clinical heart failure is 0.1-0.2%, which doubles for every additional decade in age [54]. Projections show that in the coming decades the problem will only increase [98] and so it is a keen area interest for people the world over.

2.6.1 Myocardial Infarctions

A common cause of heart failure is myocardial infarctions, commonly known as heart attacks, which inflict irreversible necrosis on the myocardium [114]. For a myocardial infarction to occur, a cardiac blood vessel is blocked, stopping the blood flow all together. The lack of blood flow in the muscle tissue starves the area of oxygen and causes the death of the myocytes. However, there is often a surviving layer of tissue on the endocardium, which receives the necessary flow of blood from the chambers themselves. The damage to the heart tissue results in, not only, abnormal mechanical properties but it often disrupts electrical signalling patterns in the tissue and, in a significant portion of patients, leads to sudden cardiac death.

In 2015, roughly 15.9 million myocardial infarctions happened, worldwide [1]. There are five major risk factors of coronary heart disease: hypertension (high blood pressure), smoking, dyslipidemia (abnormal levels of lipid e.g. cholesterol), diabetes, and family history of coronary heart disease, with 85% of patients who present with an MI having at least 1 of these risk factors [11].

After a myocardial infarction occurs a scar is left on the myocardium. The infarct scar is not electrically inert. Regions of normal myocardium extend into the infarct through the border zone and islands of surviving cardiomyocytes located within the infarct scar are observed. Further, the healed infarct is neovascularised and the surviving cardiomyocytes support electrical activity by linking to an extensive fibroblast network.

From experiments performed by Myles et al [66, 67], it is clear that the scar caused by a myocardial infarction affects several aspects of the AP propagation. In these experiments, sections of rabbit left ventricles were removed, from both healthy rabbits and those that have had induced myocardial infarctions and been allowed to heal over 8 weeks. These transmural sections were then stimulated on the endocardium, and using fluorescent dye, that varies based on the potential of the surface, the propagating action potential was recorded. Figure 2.3 shows examples from these experiments. Notably it can be seen in the healthy case (top row) the activation times of the tissue moves with a constant wave from the endocardium to the epicardium. Whereas in the scarred case (bottom row), the AP takes longer to propagate into the scarred region, on the

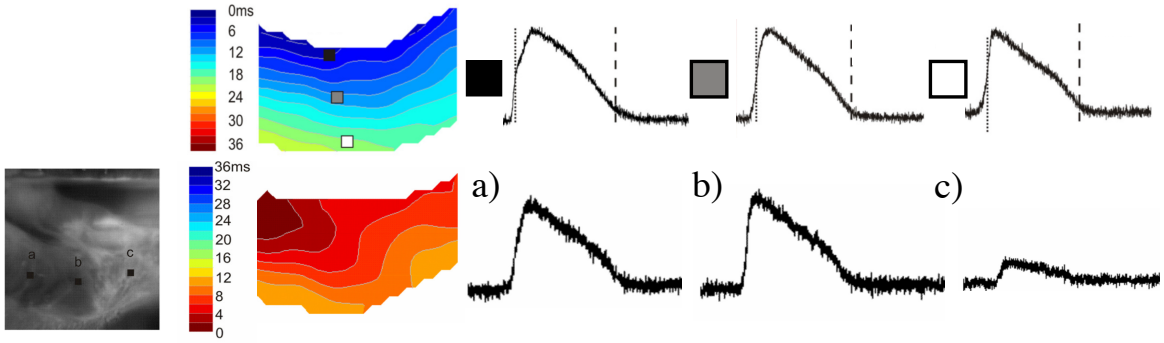

Figure 2.3: The top row (from left to right) shows the activation times across a section of healthy myocardium taken from the left ventricle of a rabbit after being stimulated on the endocardium. Then the fluorescence recordings at the endocardium, the middle of the myocardium, and the epicardium, respectively, from [67]. The bottom row (from left to right) shows an image of a transmural section of the left ventricle of a rabbit that has had an induced myocardial infarction. Here the right side of the image is lighter in colour and indicates the scarred region. The next panel is the activation times of this tissue, again with an endocardial stimulation (note that the legend colouring is reversed). The final three panels show fluorescence traces in (a) the healthy region, (b) the border zone, and (c) the scarred region from [66].

right. Although, it can be seen that the endocardium is activated almost simultaneously (as was the case in the healthy tissue), implying that the endocardial layer is still healthy. Also, from the recorded AP profiles, in the healthy case the APs do not vary much, although the AP in the epicardium was marginally shorter. However, in the scarred case the AP has a significantly reduced AP amplitude, due to the remnant myocardium.

These experiments were repeated, with the same tissues, but with epicardial stimulation. These results can be seen in Figure 2.3. As with the profiles recorded from the endocardial stimulation, the APs remain largely unchanged, with the exception of the AP recorded in the scarred region, which has a reduced amplitude. However, when the tissue is stimulated from the epicardium, the activation patterns that are recorded in both the healthy and scarred cases are very different, to those recorded with the endocardial stimulation. Here the AP is much slower to propagate, and moves slower as it propagates to the right, compared how it propagates to the left.

2.6.2 Fibrosis

When cardiac tissue is damaged or diseased, myocytes die and a healing process, known as fibrosis, starts [43]. This process has three key stages: inflammation and necrosis, fibrosis and proliferation, and finally long-term remodelling with maturation [89]. There are a range of factors that contribute to cardiac fibrosis, such as mechanical pressure overload, damage to the tissue (for example a myocardial infarction), age, and congenital heart disease [77].

Initially dormant fibroblasts start to proliferate, form intercellular connections with myocytes [49] and create collagen to repair the damaged tissue and form a scar [70]. The process of fibrosis

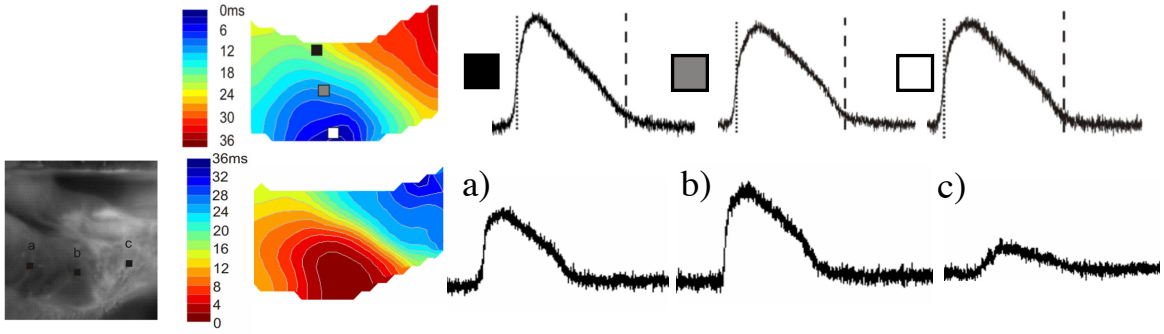

Figure 2.4: The top row (from left to right) shows the activation times across a section of healthy myocardium taken from the left ventricle of a rabbit after being stimulated on the epicardium. Then the fluorescence recordings at the endocardium, the middle of the myocardium, and the epicardium, respectively, from [67]. The bottom row (from left to right) shows an image of a transmural section of the left ventricle of a rabbit that has had an induced myocardial infarction. Here the right side of the image is lighter in colour and indicates the scarred region. The next panel is the activation times of this tissue, again with an epicardial stimulation (note that the legend colouring is reversed). The final three panels show fluorescence traces in (a) the healthy region, (b) the border zone, and (c) the scarred region from [66].

forms a scar with a decreased number of myocytes and an increased number of fibroblasts and an increased collagen density, compared to healthy tissue [90].

The fibrotic region is comprised primarily of collagen fibres and fibroblasts or myofibroblasts with a few pockets of surviving myocytes, which may be insulated by the connective tissue. The scarred region is thinner than the surrounding healthy myocardium and effectively does not contract, due to the increase in collagen and the decrease of myocytes, although the new myofibroblasts do have some contractile ability. There is also a surviving layer of myocytes at the endocardium, known as the endocardial rim which is due to the configuration of the coronary circulation [58]. Fibrosis can be characterised by the density of conductive tissue and collagen [70], and at four levels of intensity. Diffusive fibrosis (the least fibrotic tissue) has some increased levels of collagen, interstitial and patchy fibrosis have a mixture of conductive tissue and collagen and are the most arrhythmogenic, finally compact fibrosis (the most fibrotic tissue) is primarily collagen. Examples of fibrosis histology are shown in Figures 1 in the paper by Nguyen et al. [70] shows examples of the histology of these four categories of fibrosis. Similarly, in Figure 1 from the paper by Yamamura et al. [123], there is a closer example of fibrosis and the complex patterns that occur. These two figures show collagen dyed red with conductive tissue as yellow. Myocytes and fibroblasts can not be dyed separately in such figures and so they can not be distinguished at this scale. However, the regions with denser collagen have experienced cell death and then increased levels of fibroblasts and regions without denser collagen will have a fewer fibroblast cells. The key properties of fibrosis are: the fibroblast density, the size of the fibrotic region and the amount of collagen. In experimental work, it has been shown that if fibroblasts occupy a larger volume than in healthy tissue the conduction velocity of the AP

is decreased, the maximum diastolic potential of the AP is increased and the AP amplitude is decreased [59, 66, 105].

Between the healthy cardiac tissue and the infarcted zone there is a border zone, which is neither healthy nor just scar tissue. Here, the tissue contains cardiomyocytes and myofibroblasts. The regions of myofibroblasts are not evenly distributed in this border zone, but instead are in patches that appear with increasing frequency closer to the infarcted zone. This patchy variation of cardiomyocyte and myofibroblast density causes a fingering pattern between the two zones [66]. The shape of these border zones disrupts the wave of electricity and have been linked to the induction of ventricular tachycardia.

Chapter 3

Mathematical Models of Muscle Contraction

In this chapter the history and fundamentals of mathematical models of muscle contraction are introduced.

3.1 Introduction to Mathematical Models of Muscle Contraction

One of the most fundamental models for muscle contraction is the Hill model [33]. In this model, the muscle fibre is considered to be a contractile unit attached in series to an elastic element, as seen in Figure 3.1a). This model can then be extended to the three-element Hill model, that can be considered as an elastic element in series with a contractile element, which are both parallel to another elastic element, this includes the myofilament structure in the model, as seen in Figure 3.1b). For some time, an alternative form of the three-element model was also considered, in which there was a contractile unit and elastic unit in parallel and then the second elastic unit was in series to the two units in parallel. However, by varying the parameters of the system both forms of the three-element model can be shown to be equivalent, as seen in [28]. The two forms of the three element model can be seen in Figures 3.1b) and 3.1c)

The contractile unit is characterised by a force-velocity relationship, which is derived by considering the rate of change of the energy that is released from a muscle, that is allowed to shorten quickly [45, 46]. The muscle is assumed to be tetanised, meaning that it is in a state of sustained contraction. This gives the equation,

$$v(p+a) = b(p_0+a) \tag{3.1}$$

where p is the muscle tension and v is the contraction velocity. The constants a and b are parameters, found by fitting the system to data and p_0 is the muscle tension when $v = 0$. The

(a) Hill's Two-element Model (b)Hill's Three-element Model (c) Alternate form of Hill's Three-element Model

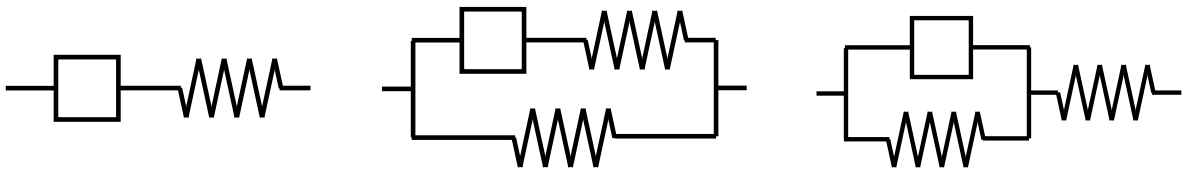

Figure 3.1: Schematic diagrams of the forms of Hill's model of muscle contraction adapted from [28]. Where the squares represent contractile units and the resistance symbols (or zig-zag symbols) represent the elastic units. a) The original two-element form of Hill's model, b) the 3-element form of Hill's model and c) The alternate form of the 3-element form of Hill's model.

length of the system is denoted L, the summation of the length of the elastic unit is x, and the length of the contractile unit, l. Thus $L = x + l$ and the velocity of the contractile unit (seen in Equation 3.1) is $v = -dl/dt$.

Since the elastic element and the contractile unit are in series, they experience the same force. By assuming the elastic force is a function of its length, $p = P(x)$, an equation of its change in time can be found,

$$\frac{dp}{dt} = \frac{dP}{dx}\frac{dx}{dt} = \frac{dP}{dx}\left(\frac{dL}{dt} - \frac{dl}{dt}\right) = \frac{dP}{dx}\left(\frac{dL}{dt} + v\right). \tag{3.2}$$

By assuming that the elastic element's tension is linear, $P = \alpha(x - x_0)$, and rearranging Equation 3.1 it is found that,

$$\frac{dp}{dt} = \alpha\left(\frac{dL}{dt} + \frac{b(p_0 - p)}{p + a}\right), \tag{3.3}$$

where x_0 is the resting length of the elastic element, and α is the spring constant [29, 45]. To find values of the constants, this model is fitted to data of the velocity of shortening after being released from a prescribed load, as seen in Figure 3.2. Despite its simple form, it can be used to model a range of behaviours of muscle tissue. For example, experiments with isometric conditions. By repeatedly stimulating the resting tissue, isometric tension can be built up. To measure the tension, the tissue is held at a constant length, and so $dL/dt = 0$, thus the differential equation of muscle tension can be solved to find the change in tension over time,

$$-P - (P_0 + a)\log\left(\frac{P_0 - P}{P_0}\right) = \alpha b t. \tag{3.4}$$

Similarly the system can model the change in tension if it is allowed to decrease with a constant velocity, $dL/dt = u$. Again substituting in the velocity and solving to find an equation of the change in tension with time.

The Hill model provides insight into the mechanics of muscle tissue, however it does not include the forces from the active contraction that is created by crossbridge formation, as described in Section 2.5. The crossbridge formation process was first considered in 1957, by A.

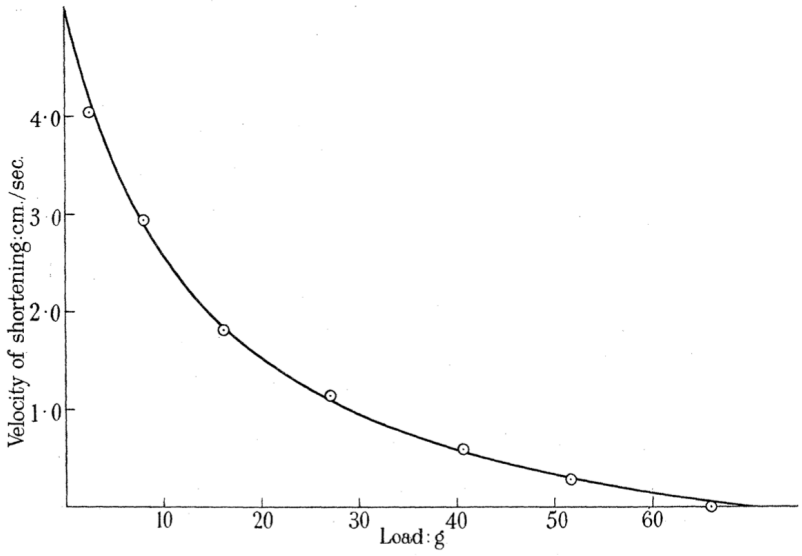

Figure 3.2: The Hill model fitted to data of the shortening velocity against the load on the muscle [33].

F. Huxley [42], which combined the work by Hill, with understanding of the attachment and detachments of myosin in the myofilaments. This model considered the system of crossbridge formation to have only two states, bound and unbound, unlike the four that are seen in more modern models of muscle contraction, for example those by Rice et al. [88] and Land et al. [51]. These more recent models include states that distinguish not only between the rotated and un-rotated bounds states, but also unbound states for which a bond is and is not permitted. It is the distinction between these non-permissive and permissive states that includes the dependence on the calcium ion concentration. This dependence allows the mechanical model to be coupled with a model of the cells electrophysiology, which, if it is a suitable ion current model, will include a profile of the calcium concentration, although this coupling will not be utilised in this work.

The Rice model by Rice et al. [88] is a model of sarcomere contraction based on the cross-bridge formation discussed in Section 2.5. This model is the basis of many updated models. For example, the model by Land et al. [51]. This model utilises a different system of forces, as seen in Figure 3.3, which shows the force systems of the Rice model and the Land model. Crucially, the Land model does not include the effects of the mass. It should also be noted, the parallels between the Rice and Land model force systems and the two forms of the Hill three-element models, seen in Figures 3.3(b) and (c), which were shown to be identical. It may be of worth in future work to investigate if there is a difference between the Rice model form and Land model form if the Rice model did not include the mass. There is also an updated form of the length dependence of the system, although there is little difference between the two length dependences. These updates are not sufficient to warrant using the updated models over the more established and accepted Rice model, which will be used in the subsequent work.

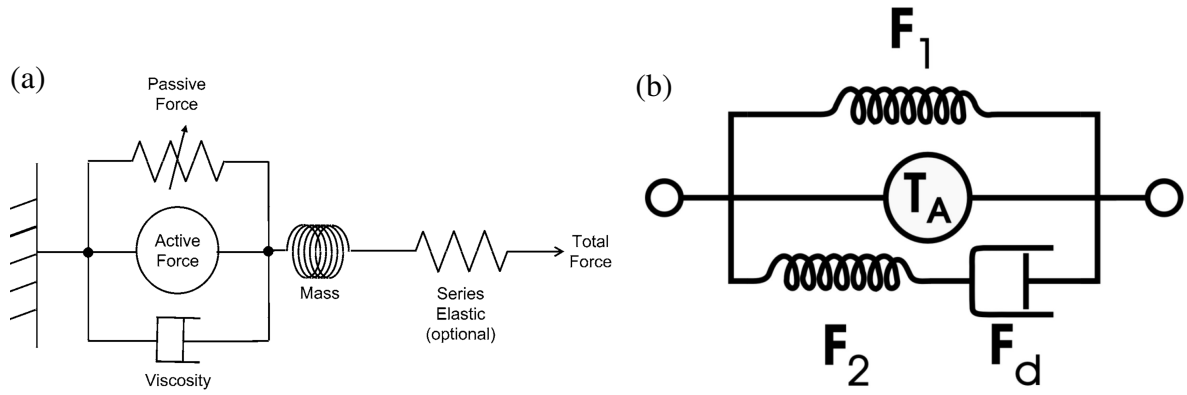

Figure 3.3: a) The force components of the contraction model, from Rice et al. [88] and b) the forces components, from Land et al. [51]. T_A is the active force, F_1 is the passive force from the external structure. F_2 is the series elastic force, which is also linear. F_d is a dashpot, which is the viscosity.

3.2 The Rice Model

The single cell model of the cardiac myofilament, developed by Rice et al. [88], has been used to simulate a wide variety of experimental muscle characterisations such as Force-Calcium relations and twitches under isometric, isosarcometric, isotonic and auxotonic conditions [88]. Their model includes the effects of mass, viscosity and passive restoring forces, as well as an active force based on crossbridge theory. Starting with the mechanisms of the calcium attaching to the troponin, and the rates of attachment, before mathematically describing the transitions between the four states involved in crossbridge formation. These then inform the overlap filaments and the forces involved in a cycle. All of these mechanisms culminate in defining the changes in the sarcomere length.

In this section the equations and formulation of the Rice model are outlined.

3.2.1 Calcium Binding

As discussed in Sections 2.4 and 2.5, the process of muscle contraction is facilitated by the presence of calcium ions binding to the troponin regulatory units. There are two types of these regulatory units, the high affinity sites, $\mathrm{CaTrop_H}$, and the low affinity sites, $\mathrm{CaTrop_L}$. They both have a proportion of the calcium ions bound to them, which are calculated to be the fractional population with calcium ions bound to these sites,

$$\frac{d}{dt}\mathrm{CaTrop_H} = k_{\mathrm{onT}}[\mathrm{Ca}](1-\mathrm{CaTrop_H}) - k_{\mathrm{offHT}}\mathrm{CaTrop_H}, \tag{3.5}$$

$$\frac{d}{dt}\mathrm{CaTrop_L} = k_{\mathrm{onT}}[\mathrm{Ca}](1-\mathrm{CaTrop_L}) - k_{\mathrm{offLT}}\mathrm{CaTrop_L}, \tag{3.6}$$

where k_{onT} the bind rate of the calcium, [Ca], is the concentration of calcium ions, and k_{offHT} and k_{offHT} are the unbinding rates of the calcium ions at the high and low affinity binding sites respectively.

Although these binding and unbinding rates are distinct, they have the same essential form,

$$k_{\text{xT}} = k_{\text{x}} \times kxmod \times kxmod_{\text{species}} \times Qk_{\text{x}}^{((\text{TmpC}-37)/10)}, \tag{3.7}$$

where k_{x} is the base rate constant under the default conditions; $kxmod$ is a modifier that is based on other parameters or states, $kxmod_{\text{species}}$ is modifier based on species. These modifiers are not always included as the modification may not be necessary. Finally, Qk_{x} is the $Q10$ value for 10° changes in the temperature as specified by TmpC.

The binding rate, k_{onT}, is defined to be,

$$k_{\text{onT}} = k_{\text{on}} \times Qk_{\text{on}}^{((\text{TmpC}-37)/10)}, \tag{3.8}$$

where $k_{\text{on}} = 50\mu M^{-1}s^{-1}$ and $Qk_{\text{on}} = 1.5$.

Similarly, the unbinding rates of the high and low affinity cases are,

$$k_{\text{offHT}} = k_{\text{offH}} \times koffmod_{\text{species}} \times Qk_{\text{x}}^{((\text{TmpC}-37)/10)}, \tag{3.9}$$

$$k_{\text{offLT}} = k_{\text{offL}} \times koffmod_{\text{species}} \times Qk_{\text{x}}^{((\text{TmpC}-37)/10)}, \tag{3.10}$$

where $k_{\text{offH}} = 25\text{s}^{-1}$, $k_{\text{offL}} = 250\text{s}^{-1}$ and Qk_{pff}=1.2. The species dependent values, $koffmod_{\text{species}}$ is 1 for rats, and 0.9 for rabbits. In the following work, this value was set to the rabbit values. This choice was arbitrarily chosen as the model constructed in Chapter 4 is not species specific.

3.2.2 Binding Site States and Crossbridge Cycling

Based on the mechanism of muscle contraction, it is assumed that there are four individual states of the binding sites. The first is the non-permissive state. This is the initial and resting state of the binding site, where the calcium has not bound to the troponin and thus the crossbridge cannot form. Second, the permissive state, in which the calcium ions are bound to the troponin and made the binding site accessible but a crossbridge has not yet formed. Thirdly, there is the state in which the myosin is bound but has not yet rotated, known as the bound state (or pre-rotated state) and finally the rotated state where the myosin rotates to pull the two filaments past each other, thus generating a force that acts to shorten the sarcomere. The crossbridge then rotates back to its original state or unbinds. The proportions of the four sites in these states are given by N, P, B and R, respectively[1]. These variables vary within the set $[0,1]$ and initially are set to be, $N = 1$ and $P = B = R = 0$. An illustration of this process and the four states are shown in Figure

[1] In the original paper, [88], the states were denoted by N_{XB}, P_{XB}, XB_{PreR}, and XB_{PostR}, respectively.

3.4, in this figure the rate of change from one state to another is labelled on the arrows between the states.

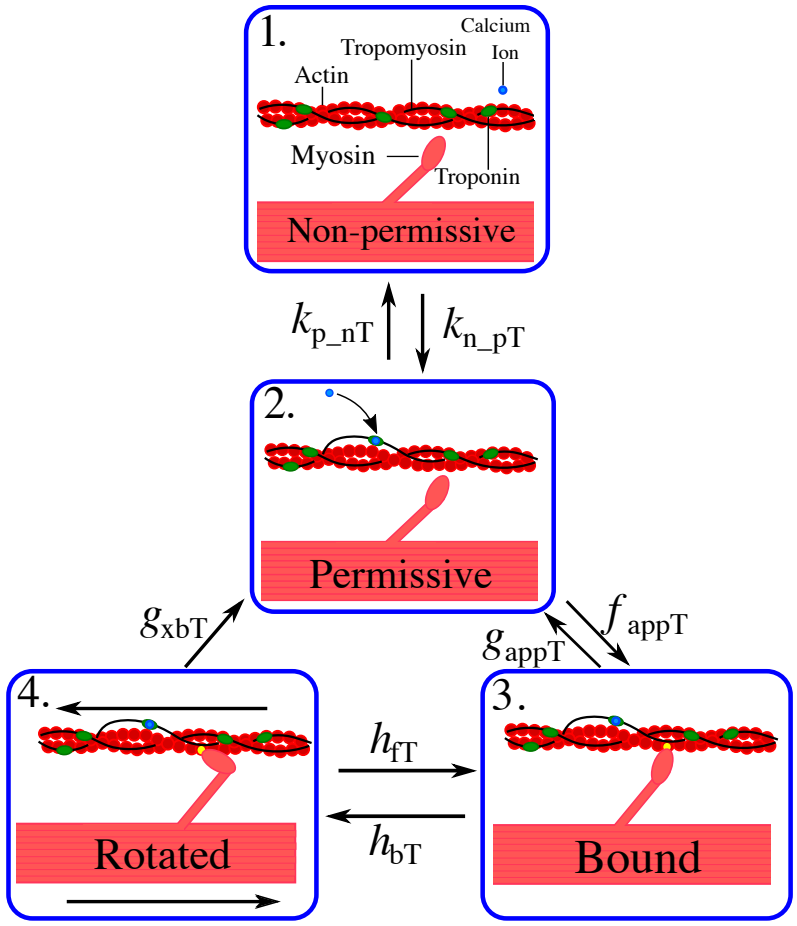

Figure 3.4: Illustration of the four stages of crossbridge formation and rotation, and the respective rates of transition between the states, as described in [88].

Whether or not the binding sites can transition into the bound states is dependent on if there is a single overlap of the thin and thick filaments. The Rice model can also account for those binding sites that fall outside the regions that will allow binding, and defines the proportion of said non-permissive and permissive states, in the regions that do not have a single overlap of the thin and thick filaments, respectively defined as,

$$\frac{d}{dt}N_{\text{NoXB}} = -k_{\text{n\_pT}} \times N_{\text{NoXB}} + k_{\text{p\_nT}} P_{\text{NoXB}}, \tag{3.11}$$

$$\frac{d}{dt}P_{\text{NoXB}} = k_{\text{n\_pT}} \times N_{\text{NoXB}} - k_{\text{p\_nT}} P_{\text{NoXB}}, \tag{3.12}$$

where $k_{\text{n\_pT}}$ and $k_{\text{p\_nT}}$ are the rate of change from the non-permissive and permissive states and vice versa, respectively. These rates are defined with a non-linear function of the regulatory units with bound calcium ions.

$$\text{Trop}_{\text{Regulatory}}(x) = (1 - SOVF_{\text{thin}}(x)) \times \text{TropCa}_{\text{L}} + SOVF_{\text{thin}}(x) \times \text{TropCa}_{\text{L}}, \tag{3.13}$$

where, $\text{Trop}_{\text{Regulatory}}(x)$ is the fraction of thin filament regulatory units with bound calcium ions, x is the sarcomere length, and $SOVF_{\text{thin}}(x)$ is the single-overlap function for the thin filament, which is defined and discussed further in Section 3.2.3. Rice et al assume the co-operativity of the nearest-neighbours shifts the regulatory units to the permissive state with the following non-linear function,

$$permtot = (1/(1+(perm_{50}/\text{Trop}_{\text{Regulatory}}(x))^{\text{n}_{\text{perm}}}))^{0.5}, \tag{3.14}$$

where, $perm_{50}$ = 0.5 is the half-activation constant and n_{perm}= 15 is the Hill coefficient. This function is included in the rate from the non-permissive to the permissive state,

$$k_{\text{n\_pT}} = k_{\text{n\_p}} \times permtot \times Qk_{\text{n\_p}}^{((\text{TmpC-37})/10)}, \tag{3.15}$$

where, $k_{\text{n\_p}} = 50\text{s}^{-1}$ and $Qk_{\text{n\_p}}$=1.6.

Whereas, in the reverse direction, the rate from the permissive to the non-permissive states is defined as,

$$inversepermtot = \min\left(\frac{1}{permtot}, 100\right), \tag{3.16}$$

$$k_{\text{p\_nT}} = k_{\text{p\_n}} \times inversepermtot \times Qk_{\text{p\_n}}^{((\text{TmpC-37})/10)}, \tag{3.17}$$

where $k_{\text{p\_n}}$=500s^{-1} and $Qk_{\text{p\_n}}$=1.6.

Similarly to those in regions that will not allow crossbridges to form, the four binding sites in the region that allows crossbridges are defined as a system of ODEs, which are derived by considering the transactions that are illustrated in Figure 3.4 using the law of mass action,

$$\frac{dN}{dt} = -k_{\text{n\_pT}}N + k_{\text{p\_nT}}P, \tag{3.18}$$

$$\frac{dP}{dt} = k_{\text{n\_pT}}N - (k_{\text{p\_nT}} + f_{\text{appT}})P + g_{\text{appT}}B + g_{\text{xbT}}R, \tag{3.19}$$

$$\frac{dB}{dt} = f_{\text{appT}}P - (g_{\text{appT}} + h_{\text{fT}})B + h_{\text{bT}}R, \tag{3.20}$$

$$\frac{dR}{dt} = h_{\text{fT}}B - (h_{\text{bT}} + g_{\text{xbT}})R. \tag{3.21}$$

Again, the rates of change have the same form and are dependent on the temperature and species.

The rate of change from the permissive to bound state, f_{appT}, is defined to be,

$$f_{\text{appT}} = f_{\text{app}} \times xbmod_{\text{species}} \times Qf_{\text{app}}^{((\text{TmpC}-37)/10)}, \tag{3.22}$$

where $f_{\text{app}} = 500\text{s}^{-1}$ and Qf_{app} = 6.7. It should be noted other than the species and temperature dependence, the rate is fixed.

The rate of change returning from the bound state to permissive bound state, g_{appT}, is defined to be,

$$g_{\text{appT}} = g_{\text{app}} \times g_{\text{app}}slmod \times xbmod_{\text{species}} \times Qg_{\text{app}}^{((\text{TmpC}-37)/10)}, \tag{3.23}$$

$$g_{\text{app}}slmod = 1 + (1 - SOVF_{\text{thick}}(x)) \times gslmod, \tag{3.24}$$

where $g_{\text{app}} = 70^{-1}$ and Qg_{app}=2.5, and $gslmod$=6 scales the thick filament effects. The function $g_{\text{app}}slmod$ increases the rate of detachment at shorter sarcomere lengths.

The rate of change from the bound to rotated states, h_{fT}, is defined to be,

$$h_{\text{fT}} = h_{\text{f}} \times h_{\text{f}}mod \times xbmod_{\text{species}} \times Qh_{\text{f}}^{((\text{TmpC}-37)/10)}, \tag{3.25}$$

$$h_{\text{f}}mod = \exp\left(-\text{sign}(\eta_B) \times hfmdc \times \left(\frac{\eta_B}{\text{x}_0}\right)^2\right), \tag{3.26}$$

where, h_{f}=2000^{-1}, Qh_{f}=6.25, and $hfmdc$=5 is the extent of the mean strain of the bound state affects the isomerisation rate. η_B is the mean distortion, and is defined in Section 3.2.4.

The reverse rate from the rotated to bound states, h_{bT}, is,

$$h_{\text{bT}} = h_{\text{b}} \times xbmod_{\text{species}} \times Qh_{\text{b}}^{((\text{TmpC-37)/10})}, \tag{3.27}$$

where h_{b}=400s^{-1} and Qh_{b}=6.25.

The rate from the rotated to the permissive state, g_{xbT}, is,

$$g_{\text{xbT}} = g_{\text{xb}} \times gxbmd \times xbmod_{\text{species}} \times Qg_{\text{xb}}^{((\text{TmpC}-37)/10)} \tag{3.28}$$

where g_{xb}=70s^{-1} and Qg_{xb}=6.25. The term $gxbmd$ is the strain-dependence defined as,

$$gxbmd = \begin{cases} \exp(\sigma_{\text{p}}((x_0 - \eta_{\text{R}})/x_0)^2) & \text{if} \quad \eta_{\text{R}} < x_0, \\ \exp(\sigma_{\text{n}}((x_0 - \eta_{\text{R}})/x_0)^2) & \text{if} \quad \eta_{\text{R}} \geq x_0, \end{cases} \tag{3.29}$$

where σ =8 and σ_{n}=1 set the effects of strain in positive and negative shortening velocities. The value η_R is the mean distortion of the rotated state, and is described further in Section 3.2.4.

3.2.3 Sarcomere Geometry

Beyond the state of the binding sites and the crossbridges, another key part of the mechanism is the length of the sarcomere, or more specifically the extent to which the thin and thick filaments overlap. The cross-section of the filaments is arranged in a hexagonal pattern, with the filaments suspended next to each other, held in place by titin, an illustration of the sarcomere geometry is seen in Figure 3.5a.

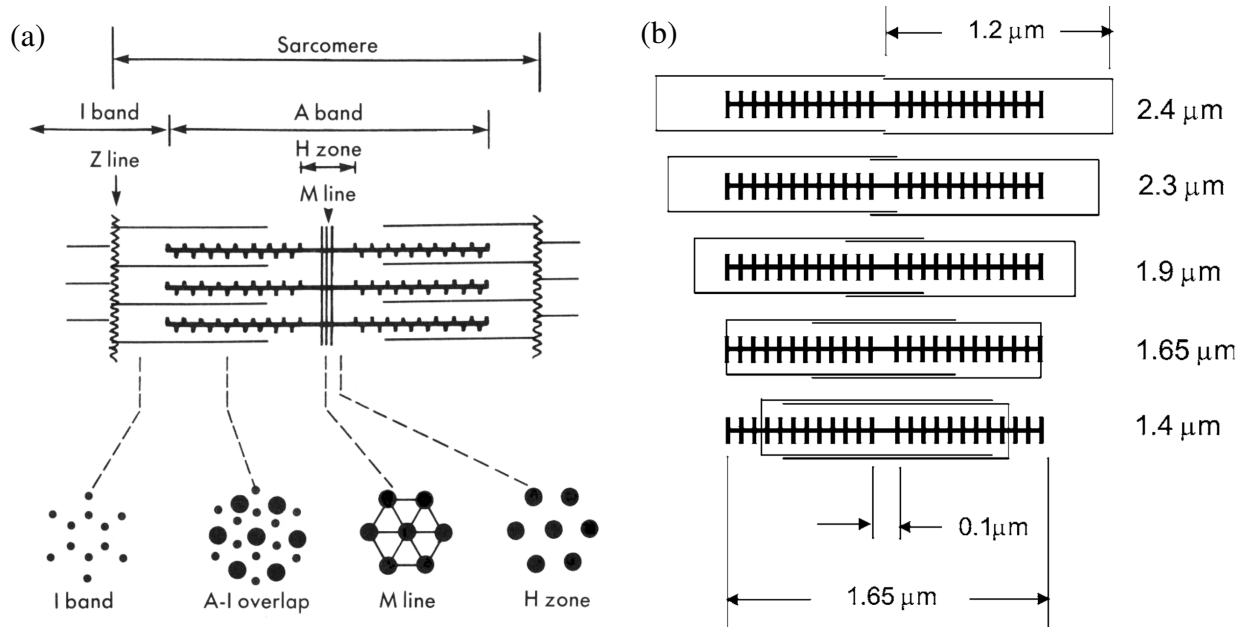

Figure 3.5: a) Longitudinal and cross-sectional illustrations of the geometry and filaments of the sarcomere, from [45]. b) Sarcomere Geometry of the filament length and movements [88].

It is assumed that for the crossbridges between the filaments to form, there must only be a single overlap of the filaments. Meaning, if the sarcomere is stretched too far, the filaments stop overlapping and the region that will allow crossbridges begins to reduce, but if the sarcomeres contract too far the filaments from adjacent units begin to overlap the same region too and the area that is viable for bonding begins to reduce also. An illustration of the how the overlap changes with the sarcomere length is seen in Figure 3.5b.

In the Rice model, there are functions of the proportion of the thin and thick filaments that have a single overlap, denoted $\text{SOVF}_{\text{thin}}$ and $\text{SOVF}_{\text{thick}}$, respectively. The thin filaments have length 1.2μm and the thick filaments have a length of 1.65μm, with the section in the myosin with no crossbridges, $\text{length}_{\text{hbare}}$, with a length 0.1μm. The key equations for this these single overlap regions are,

$$\text{SOVF}_{\text{thick}}(x) = \frac{2 \times \text{length}_{\text{sovr}}(x)}{\text{length}_{\text{thick}} - \text{length}_{\text{hbare}}}, \tag{3.30}$$

$$\text{SOVF}_{\text{thin}}(x) = \frac{\text{length}_{\text{sovr}}(x)}{\text{length}_{\text{thin}}}. \tag{3.31}$$

3.2.4 Mean Distortion

The mean distortions of the bound and rotated states[2] are given respectively as,

$$\frac{d}{dt}\eta_B = \frac{1}{2}\frac{dSL}{dt} + \frac{\phi}{B^{\text{DutyFract}}}\left[k_{p-b}(-\eta_B) + k_{r-b}(\eta_R - x_0 - \eta_B)\right],$$
$$\frac{d}{dt}\eta_R = \frac{1}{2}\frac{dSL}{dt} + \frac{\phi}{R^{\text{DutyFract}}}\left[k_{b-r}(\eta_B + x_0 - \eta_R)\right],$$

where η_B and η_R the mean distortion of the bound and the rotated states, x_0 is the mean distortion between the two states. SL is the sarcomere length and ϕ is an empirically derived scaling term. Finally, $B^{\text{DutyFract}}$ and $R^{\text{DutyFract}}$ are steady state populations of the bound and rotated states, which are defined using the King-Altman rule [47] and are defined to be,

$$B^{\text{DutyFract}} = \frac{f_{\text{appT}}h_{\text{bT}} + f_{\text{appT}}g_{\text{xbT}}}{g_{\text{xbT}}h_{\text{fT}} + f_{\text{appT}}h_{\text{fT}} + g_{\text{appT}}h_{\text{bT}} + g_{\text{appT}}g_{\text{xbT}} + f_{\text{appT}}h_{\text{bT}} + f_{\text{appT}}g_{\text{xbT}}}$$
$$R^{\text{DutyFract}} = \frac{f_{\text{appT}}h_{\text{fT}}}{g_{\text{xbT}}h_{\text{fT}} + f_{\text{appT}}h_{\text{bT}} + g_{\text{appT}}h_{\text{bT}} + g_{\text{appT}}g_{\text{xbT}} + f_{\text{appT}}h_{\text{bT}} + f_{\text{appT}}g_{\text{xbT}}}.$$

The inverses are used in the mean distortion definitions as scaling factors to represent the dependence on the time a crossbridge is in a particular state. By considering the optimal conditions, the maximum state occupancies can be found,

$$B^{\text{Max}} = \frac{f_{\text{app}}h_{\text{b}} + f_{\text{app}}g_{\text{xb}}}{g_{\text{xb}}h_{\text{f}} + f_{\text{app}}h_{\text{f}} + g_{\text{app}}h_{\text{b}} + g_{\text{app}}g_{\text{xb}} + f_{\text{app}}h_{\text{b}} + f_{\text{app}}g_{\text{xb}}}$$
$$R^{\text{Max}} = \frac{f_{\text{app}}h_{\text{f}}}{g_{\text{xb}}h_{\text{f}} + f_{\text{app}}h_{\text{b}} + g_{\text{app}}h_{\text{b}} + g_{\text{app}}g_{\text{xb}} + f_{\text{app}}h_{\text{b}} + f_{\text{app}}g_{\text{xb}}}.$$

3.2.5 Force Components

With the sarcomere geometry and the contraction mechanisms outlined, the forces of the system can be defined. There are many forces at play in this system, not only from the contraction by the sarcomeres, but also from the internal and external structures of the sarcomere. As well as damping effects from the viscosity and mass.

The active force from the sarcomere is given by,

$$F_a(x) = \text{SOVF}_{\text{thick}}(x)\left(\frac{\eta_B B + \eta_R R}{x_0 R^{\text{Max}}}\right), \tag{3.32}$$

where η_B and η_R are the mean distortions of the bound pre-rotated and rotated states, and are themselves defined by a first order ODE. Also, x_0 is the initial value of η_R and R^{Max} is the fraction of strongly-bound crossbridges under the optimal conditions. The optimal conditions, which

[2] In the original paper, [88], the mean distortions were denoted xXB_{PreR}, and xXB_{PostR}, respectively.

give the maximum possible values, are high calcium activation, isosarcometric, a physiological temperature of 37°C and a maximal single overlap of thick and thin filaments ($SL > 2.3\mu$m).

In the Rice model the passive force is defined so that when the length of the sarcomere is below the rest length there is a negative passive force trying to stretch the sarcomere back to the rest length, acting against the total muscle force and vice versa when the length is longer than the rest length. This stops the sarcomere from becoming too compressed or stretched and is the influence of the internal mechanisms in the sarcomere, primarily titin but also collagen can be included if a trabeculae is being considered rather than an isolated cell. This collagen does not stretch much and restricts the sarcomere from stretching to a length much more than 2.25μm. These functions are defined below, and are plotted in Figure 3.6.

$$F_{\text{Ti}}(x) = \begin{cases} PCon_{\text{titin}} \times (\exp(PExp_{\text{titin}} \times (x - SL_{\text{rest}})) - 1) & \text{if} \quad x \geq SL_{\text{rest}}, \\ -PCon_{\text{titin}} \times (\exp(PExp_{\text{titin}} \times (SL_{\text{rest}} - x)) - 1) & \text{if} \quad x < SL_{\text{rest}}, \end{cases} \tag{3.33}$$

$$F_{\text{Col}}(x) = \begin{cases} PCon_{\text{col}} \times (\exp(PExp_{\text{col}} \times (x - SL_{\text{col}})) - 1) & \text{if} \quad x \geq SL_{\text{rest}}, \\ 0 & \text{if} \quad x < SL_{\text{col}}, \end{cases} \tag{3.34}$$

$$F_{\text{Pass}}(x) = \begin{cases} F_{\text{Ti}}(x) & \text{if} \quad \text{isolated cell}, \\ F_{\text{Ti}}(x) + F_{\text{Col}}(x) & \text{if} \quad \text{trabeculae}. \end{cases} \tag{3.35}$$

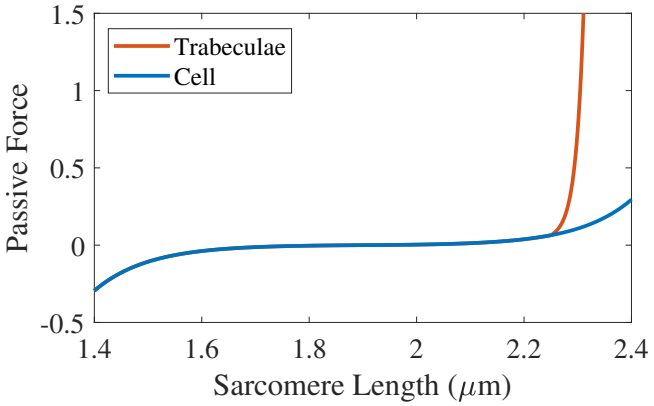

Figure 3.6: Plot of the two forms of the passive force.

The afterload force is defined by,

$$F_{\text{Aft}}(x) = \begin{cases} F_{\text{Aft}}^{\text{const}} & \text{if isotonic}, \\ KSE \times (x - SL_0) & \text{if isometric}, \\ 0 & \text{otherwise}, \end{cases} \tag{3.36}$$

when the conditions are isotonic then the afterload is constant, $F_{\text{Aft}}^{\text{const}}$, where SL_0 is the initial

length of the sarcomere and KSE is the stiffness in units of normalised force per μm. The forces are normalised, specifically around the peak twitch force found by Daniels et al [19], where they obtain the peak value to be 101.8kPa, relative to the sarcomere cross-section of the muscle in the region of measurement. It is this value that all the other are relative to. Thus, when KSE=1(unit normalised force)μm^{-1}, the non-normalised value is KSE=101.8kPa mm^{-1}.

Visco-elastic elements are also included. The muscle is assumed to have a Newtonian viscosity element, which is set to a mean value ($0.3\%F_{\max}\mu$m^{-1}s^{-1}), which was found experimentally.

A mass term is included to prevent instantaneous changes in muscle shortening velocity for quick release protocols, this improves the stability of the integration of the model equations. This also improves response times. Choosing the damping correctly is important as the wrong choice can lead to over and under damping. The mass is assumed to be constant, for a rabbit the mass is 0.00025(unit normalised force)s$^2\mu$m^{-1}.

Finally a series linear elastic element can be included to simulate the effects of compliant end connections that occur in muscle preparations, so the muscle can internally shorten while the total muscle length remains fixed. All of the components can be seen in Figure 3.3a).

3.2.6 Sarcomere Length Change

The final component of the model is the change in the sarcomere length, given by,

$$\frac{d}{dt}SL = \frac{p+(SL_0-SL)\nu}{m}, \tag{3.37}$$

$$p = \int_0^t (F_{\mathrm{a}}(x)+F_{\mathrm{Pass}}(x)-F_{\mathrm{Pre}}-F_{\mathrm{Aft}}(x))dt, \tag{3.38}$$

where SL is the sarcomere length, SL_0 is the rest sarcomere length, ν is the viscosity (a constant), m is the mass (a constant). Note the exclusion of the mass would lead to instantaneous changes in the sarcomere length, which is of course not biologically possible. Also, p is the integral of the forces with respect to time, thus it is a momentum term, F_a is the active tension (defined earlier), F_{Pass} the passive force, also defined earlier, F_{Pre} the preloaded force is defined as the initial passive force (a constant) and F_{Aft} is the afterload force.

3.3 Numerical Methods

The model of cardiac myofilaments presented by Rice et al. [88] is a system of first order ODEs. Specifically, it is a system of 11 ODEs. Cardiac myofilament contraction is dependent on the change in calcium of the cell, which in turn is dependent on the cardiac action potential, which is discussed in Section 2.3.1 and will be discussed further in Chapter 5, this involves very sharp changes in value from the fast initial upstroke and thus the system can be described as stiff. This requires a numerical method that can resolve the wave fronts. To this end a variable step,

variable order solver may be suitable, for computational efficiency. One such method is utilised in the MATLAB solver `ode15s` [99]. This solver is a quasi-constant step size implementation of the in built numerical difference formulas, with backward differences. In the next Chapter, the Rice model is adapted to construct a model on contracting units on a substrate, with the model script being adapted from the Rice model code in the CellML repository.

3.4 Discussion

In conclusion, there are many systems involved in mathematically modelling the contraction of a cardiac cell. The development of these models has taken decades and have culminated in the model of the cardiac myofilament by Rice et al. [88]. This model is well established, but continuously being added to, adapted and updated. However, for the purposes of subsequent work it is sufficient and contains many of the crucial aspects that are of interest. Specifically, it reliably models the crossbridge formation system and includes a dependence on the calcium concentration, meaning that it can also be adapted to be coupled with an electrophysiology model in any future work. It is also readily coupled in series, using a coupling scheme that is introduced in the next chapter.

Chapter 4

Cardiomyocyte Contraction when Attached to a Substrate

In this chapter the first piece of novel work is presented, in which models of sarcomere contraction that have been adapted from the model of cardiac filament contraction by Rice et al. [88], which are coupled end-to-end using a coupling scheme from Timmermann et al. [116]. This model was constructed to investigate a problem posed by experiments performed by Huethorst [41], that found a link between the contraction of a monolayer of cardiomyocytes and the stiffness of the substrate.

4.1 Introduction

The stiffness of the myocardium varies during the developmental stages and in disease. For example, the human neonatal myocardium has a Young's Modulus around 10 kPa which increases to approximately 50 kPa in a healthy adult heart [85, 117, 120]. Whereas, cardiac fibrosis increases the myocardium stiffness to approximately 100 kPa [85, 117, 120].

As with other cell types, cardiomyocytes will bind to both the surrounding cells and the extra cellular matrix (ECM) through cell adhesion complexes [30, 76, 96, 97, 120]. There are a number of studies that have shown that the substrate stiffness affects the sarcomere organisation [32, 44, 87, 92], myofibril formation [23, 25, 86], calcium handling [7, 21, 44, 92] and force generation [87, 92]. These studies primarily focussed on the effects on a single cell, and ignored the role of cell-cell coupling and force transmission between the cells [24, 124].

In work by Huethorst [41], the contraction in monolayers of the hiPSC-CM was investigated when the cardiomyocytes were cultured on a rigid substrate, for example glass or plastic, and a flexible hydrogel, and substrate-free cultures. These experiments found that spatio-temporal features of hiPSC-CM contraction are dependent on the rigidity of the substrate that the monolayers of hiPSC-CMs are attached to. Specifically, it was found that if the monolayers of myocytes are attached to a rigid substrate, such as plastic or glass, the contraction of the monolayer shows

multi-peaked behaviour in the motion traces. However, if the monolayer is substrate-free or attached to a flexible substrate like a hydrogel, the number of contraction traces with multiple peaks is significantly reduced. These phenomena are summarised in Figure 1.1.

4.1.1 Motion Capturing Techniques

To record the myocyte contraction a high-speed camera (Hamamatsu ORCA-flash 4.0 V2 digital CMOS camera C11440-22CU) (100 fps, 600×600 pixels) and a 4x, 10x or 40x objective (Olympus, air objectives) were used to record Brightfield videos. An open source contractility algorithm (MUSCLEMOTION (MM) [95]) was used to analyse the video frames. The contractility algorithm measures movement of the monolayer as a function of pixel intensity and has been verified against a number of other measures of mechanical function. The contraction algorithm is able to record the temporal parameters, for a range of illumination conditions. The recorded value is relative to the position of the substrate and is contributed to by the motion of the cell, regardless of if the cell is actively contracting. However, the amplitude of the contraction is dependent on the pixel intensity and the illumination levels and thus have arbitrary units and thus comparison between contraction amplitudes is difficult and there is no distinction between a cell that is contracting or being stretched. Another key artefact to consider is that the algorithm does not consider directional changes, and although the images has movements of the cells in two dimensions, the algorithm produces a trace of the motion against time only. An example of the recorded potential, calcium concentration and motion of a single contracting cell is shown in Figure 4.1b).

Each frame of the video was segmented into a grid, with the algorithm applied to each square in the grid, giving a spatial mapping of the hiPSC-CM contractility. Many values were measured, specifically, the spatial distribution of beat frequency, amplitude, contraction time, Up_{90}, relaxation time, Dn_{90}, and the contractility duration at 50% of the peak, CD_{50}, were measured, as seen in Figure 4.1a). The number of peaks within one time-course was also measured, as well as the start time, T_{Start}, which is measured as the time to 50% of the contraction amplitude. In order to exclude outliers, the spread of T_{Start} and CD_{50} was estimated as the difference between 10th and 90th percentile.

4.1.2 Experimental Results

The differences in the multi-peaked behaviour is seen in Figure 4.2, which shows various traces from spatial analysis of monolayers of cardiomyocytes on a rigid substrate. In Figure 4.2c), the traces from the individual grids that divided the monolayer (seen in Figure 4.1a). These traces are plotted together in Figure 4.2b). Figure 4.2e) shows the average trace from all nine grid sections, over three consecutive cycles. These traces show that in most of the grid segments multi-peaked behaviour appears and Figure 4.2e) shows that this behaviour persists over multiple

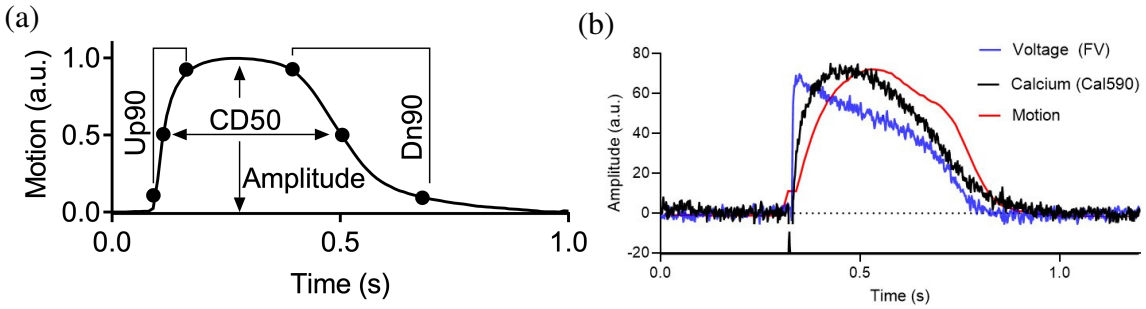

Figure 4.1: a) Schematic diagram of the measurements taken in contractility experiments [41]. b) The potential, calcium concentration and motion profiles overlapped.

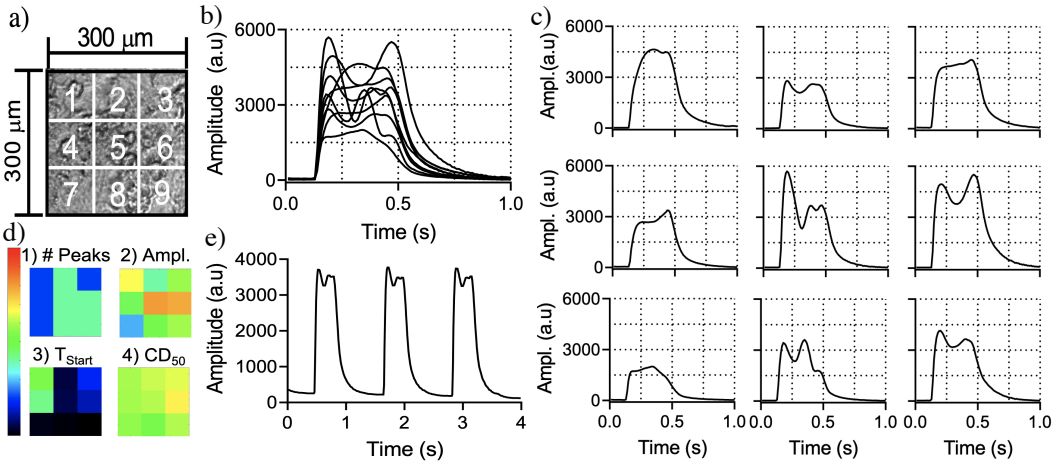

Figure 4.2: Spatio-temporal analysis of contractile behaviour of hiPSC-CMs reveals local variations of movement. a) 300×300μm fields of view were subdivided in 3×3 grid-squares of 100×100μm, where after the MM algorithm was applied to every grid-square. b) All traces from each grid-square (9 in total) were overlapped. c) All traces from each grid-square were placed in their corresponding location shown in panel (a). d) Heatmaps indicating 1) the number of peaks, 2) the amplitude of the events, 3) the start time, T_{Start}, and 4) the contractile duration at 50% of the amplitude, CD_{50}, (scalebars are 0-5 peaks, 0-7000 a.u., 0-40 ms and 0-600 ms, respectively). e) The contractility trace taken from the whole area (300×300μm). Adapted from [41].

cycles.

This work shows that rigid substrates may be inappropriate mechanical matrices for monolayers of hiPSC-CMs. This is important for both basic research and cardiotoxicity studies that use hiPSC-CMs as a stable reliable model of human myocardium. In this section we have mathematically modelled this system in order further explore the mechanisms at play here.

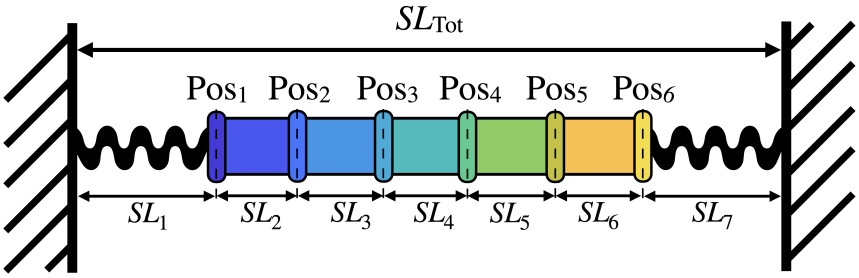

Figure 4.3: Illustration of units attached end-to-end, with external springs attached to a substrate, with the relevant measurements and positions labelled for 5 contractile units.

4.2 Mathematical Modelling of Contractile Units attached to a Substrate

In this section we set up the problem posed by this experimental work by Huethorst [41]. It is known, from previous studies, that this profile varies from cell to cell. It is assumed that all the cells are attached to each other via protein links (cadherins) and electrically coupled via another type of protein link (connexin). It is also known that the monolayer of cells adheres to the underlying matrix, via cell-adhesion complexes (SACs). It is suspected that it is variation in this interaction that underlies the complex movement signals, since when the cells are not adhering to the glass/plastic or if the tissue is cultured on a flexible matrix that these complex contraction signals are minimised.

This problem can be simplified to be considered as a group of contractile units linked in series, with springs at either end of the system, representing the cell's connections to the substrate. The stiffness of these springs can be adjusted to reflect the stiffness of the substrate, an illustration of this system can be seen in Figure 4.3. The simplifying assumption of a 1D chain of cells is justified by the fact that, not only is a 1D system simpler and faster to solve, but that the motion profiles recorded in the physical experiments do not account for 2D changes and so any 2D effects could neither be validated or compared to the experiments. Another simplification was that a model of myofilament contraction was used rather than a model of a whole myocyte. Although the experiments were concerned with whole cells, as will be discussed in Section 4.2.3, it was found that by simply adapting the passive force of the myofilament contraction, the Rice model could effectively model the recorded motion of the myocyte contraction.

The forces of the springs on the outside are defined by a simple spring. The spring length is also dependent on the springs' viscosity and mass of the spring, although appropriate values for these are unknown, and thus are arbitrarily chosen to be the same as the viscosity and mass of

sarcomere from the Rice model [88], which will be used to define the contracting units.

$$\text{For } i \in \{1,N\} \quad \text{Force}_{\text{Spring}} = K(SL_i - SL_{i,0}), \tag{4.1}$$

$$\frac{d}{dt}SL_i = \frac{p + (SL_{i,0} - SL_i)\nu}{m}, \tag{4.2}$$

where $SL_{i,0}$ is the rest length, which will be also used as the initial length of the spring, p is the force integrated, ν is the viscosity of the spring, m is mass of the spring, and K is the spring constant, with units of (unit normalized force)μm^{-1}. Recall, from Section 3.2.5, that the model forces are normalised relative to the peak-twitch force of 101.8kPa, as found by Daniels et al. [19]. In the substrate-free case the spring constant will be set to $K = 0$, and the system has no springs, in this case the viscosity will also be removed. This substrate-free case is interesting to consider, but it should be noted that it is not physically realistic as the cell can never be truly "substrate-free".

The contractile units between the springs are defined by the Rice model [88], as seen in Section 3.2.5. The calcium profile recorded by Huethorst [41], as seen in Figure 4.1b) will be used to define the contraction in the units, as they apply to the hiPSC-CM. However, note that this profile is given with arbitrary units, and so must be scaled to be in the correct units. The minimum and maximum calcium concentration will be defined by the calcium profile used by the Rice model, the Chicago rabbit ventricular myocyte model by Shannon et al. [100]. Specifically, $[\text{Ca}_i]^{\alpha} = 0.09\mu\text{M}$ and $[\text{Ca}_i]^{\omega} = 1.45\mu\text{M}$ are the minimum and maximum calcium concentrations, respectively. The rescaled data and associated fitted curve can be seen in Figure 4.4a).

The equation defining the calcium concentration profile, with the physiological values is,

$$[\text{Ca}_i] = \begin{cases} [\text{Ca}_i]^{\alpha} & \text{if} \quad t > 30\text{ms}, \\ ([\text{Ca}_i]^{\omega} - [\text{Ca}_i]^{\alpha}) \left(\frac{0.361}{1+\exp(-0.0347(t-53.5))} - \dots \right. & \\ \qquad \left. 0.1 \right) \left(\frac{3.98}{1+\exp(0.0168(t-402))} \right) + [\text{Ca}_i]^{\alpha} & \text{otherwise.} \end{cases} \tag{4.3}$$

This equation has been constructed using two sigmoidal functions to create the shape of a simple calcium profile. At which point the curve was fitted to the data taken in Figure 4.1b, to find the parameters.

4.2.1 Measurements of Motion

In the experiments by Huethorst et al [41], the recorded motion is the absolute value of the distance a point is from its initial position and are recorded as an average over a number of cells. In order to fully compare the experimental and simulated results the "motion" of the cells must be considered. To find the absolute value of the change in the position, Pos, the cumulative unit

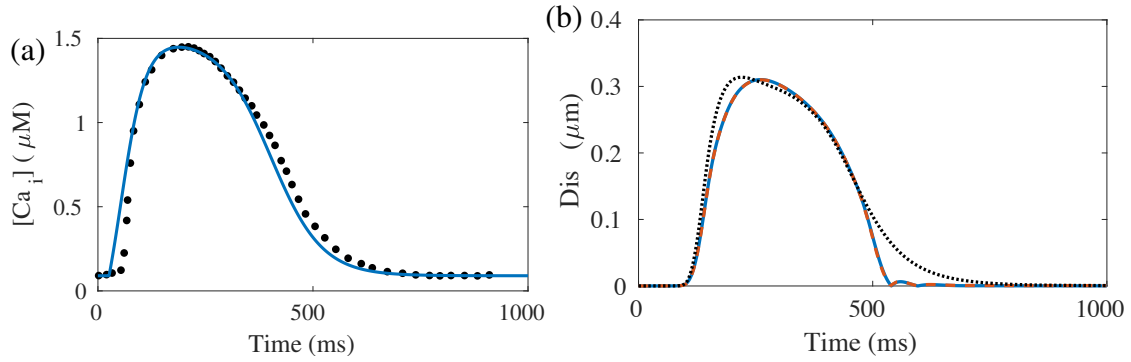

Figure 4.4: a) The calcium profile fitted to data taken from the calcium profile seen in Figure 4.1b, rescaled to units of μM. b) The displacement recorded, when the Rice model is uncoupled (blue), and the displacements of a single contractile unit in the coupled system, but with the springs exerting no force, with the scheme from Timmermann et al. [116] (black dashed line) and in the adjusted scheme (orange broken line).

length, CSL, is found to locate the ends of the units relative to the exterior. Then the position is taken to be the absolute value of the difference between the unit end position and from its initial position,

$$\text{CSL}_i = \sum_{j=1}^{i} SL_j \quad \text{and} \quad \text{Pos}_i = |\text{CSL}_i - \text{CSL}_{i,0}|, \quad \text{for} \quad i \in \{1,\ldots,N-1\}, \tag{4.4}$$

where CSL_i is the cumulative unit length. In this system there are N units, two of which are the springs, thus, let the number of contractile units be, $n = N-2$, which means that for n contractile units there are $n+1$ points of motion. Figure 4.3 shows the positions labelled for a system with n=5 contracting units, which is N=7 units in total. Note that, the colours of this figure correspond with the profiles seen in Figures 4.9, 4.11, 4.12, and 4.13.

Taking the average position gives a trace of the motion that can be most closely compared to the motion trace from the algorithm described in Section 4.1.1 and it is assumed that the position value, Pos_i, is most like the recorded motion from the algorithm. Also note that, the units are either springs or contracting units, and are not considered as sarcomeres, however, the model of the contraction will be based on a model of sarcomere contraction (see Section 4.2.2), and so to avoid confusion the unit length is denoted SL.

Another useful interpretation of the change in unit length is the displacement of the unit length,

$$\text{Dis}_i = |SL_i - SL_{i,0}|, \quad \forall i \in \{1,\ldots,N\}, \tag{4.5}$$

where $SL_{i,0}$ is the initial unit length, also note that Dis_1 and Dis_N are the displacements of the springs and are not included in subsequent plots of the displacement. Even though this displacement of the unit length does not give the whole picture of the motion in the system, it does inform about the activity of the individual unit behaviour.

4.2.2 Coupling Contraction Models in Series

In a paper by Timmermann et al. [116], sarcomeres are attached end-to-end, by redefining the change in sarcomere length to be dependent on the change in the adjacent sarcomeres' lengths. For a given number of units, N, attached end-to-end in a chain the change in unit length is redefined.

$$\frac{dSL_i}{dt} = 2\frac{d\widehat{SL}_i}{dt} - \frac{d\widehat{SL}_{i-1}}{dt} - \frac{d\widehat{SL}_{i+1}}{dt} \qquad \forall i \in \{2,\ldots,N-1\}, \tag{4.6}$$

$$\text{where} \quad \frac{dSL_1}{dt} = \frac{d\widehat{SL}_1}{dt} - \frac{d\widehat{SL}_2}{dt}, \tag{4.7}$$

$$\text{and} \quad \frac{dSL_N}{dt} = \frac{d\widehat{SL}_N}{dt} - \frac{d\widehat{SL}_{N-1}}{dt}, \tag{4.8}$$

where $\frac{d\widehat{SL}_i}{dt}$ is the unit length change, which are contractile units as defined by the Rice model [88] if $i \in \{2,\ldots,(N-1)\}$ or they are considered to be the spring units if for $i = 1, N$. In order to solve this system numerically, for each time step the uncoupled sarcomere length change is defined, and then each sarcomere length change is re-evaluated with the above scheme. Then for the next time step the coupled sarcomere length is used to define the uncoupled length change.

By defining the unit lengths with this coupling scheme, the total length of the units is held constant. This can be shown, by the summation of all the ODEs being equal to zero.

$$\frac{dSL_{\text{Tot}}}{dt} = \frac{d}{dt}(SL_1 + SL_2 + \ldots + SL_N) = \frac{dSL_1}{dt} + \frac{dSL_2}{dt} + \ldots + \frac{dSL_N}{dt} \tag{4.9a}$$

$$= \left(\frac{d\widehat{SL}_1}{dt} - \frac{d\widehat{SL}_2}{dt}\right) + \left(2\frac{d\widehat{SL}_2}{dt} - \frac{d\widehat{SL}_1}{dt} - \frac{d\widehat{SL}_3}{dt}\right) + \ldots$$

$$\cdots + \left(\frac{d\widehat{SL}_N}{dt} - \frac{d\widehat{SL}_{N-1}}{dt}\right) \tag{4.9b}$$

$$= 0 \tag{4.9c}$$

However, there is a problem with this coupling scheme. If one is to consider the case with one contractile unit and no external springs (i.e. $K = 0$), this should be equivalent to the uncoupled model. However, using this coupling scheme in this case, the rate of change of SL will be doubled, i.e.

$$\frac{d\widehat{SL}_1}{dt} = \frac{d\widehat{SL}_3}{dt} = 0 \qquad \Longrightarrow \qquad \frac{dSL_1}{dt} = 2\frac{d\widehat{SL}_2}{dt}. \tag{4.10}$$

For this reason an adjustment is suggested. The coupling scheme equations are divided by

2,

$$\frac{dSL_i}{dt} = \left(2\frac{d\widehat{SL}_i}{dt} - \frac{d\widehat{SL}_{i-1}}{dt} - \frac{d\widehat{SL}_{i+1}}{dt}\right)\Big/2 \quad \forall i \in \{2,\dots,N-1\}, \tag{4.11}$$

$$\frac{dSL_1}{dt} = \left(\frac{d\widehat{SL}_1}{dt} - \frac{d\widehat{SL}_2}{dt}\right)\Big/2, \tag{4.12}$$

$$\frac{dSL_N}{dt} = \left(\frac{d\widehat{SL}_N}{dt} - \frac{d\widehat{SL}_{N-1}}{dt}\right)\Big/2. \tag{4.13}$$

With this adjustment the uncoupled case and the single contractile unit with no springs are equivalent, and maintains the property that the total length is constant. This is shown in Figure 4.4b), in which the displacement of the uncoupled case (blue line), and the displacements of the coupled case with and without the adjustment (orange broken line and black dots, respectively) are plotted together. This shows the uncoupled case and adjusted coupled case have the exact same displacement, whereas the original coupled scheme has a faster upstroke and a slower return to the rest length. It should be noted that in this figure the displacement of the unit length is used rather than the position, since the position is relative to the external edge, which does not exist in the uncoupled case.

Perfectly rigid springs

A special case can be defined, to represent the system attached to perfectly rigid springs. In this system, the spring equations are defined to be,

$$\frac{d\widehat{SL}_1}{dt} = -\frac{d\widehat{SL}_2}{dt} \quad \text{and} \quad \frac{d\widehat{SL}_N}{dt} = -\frac{d\widehat{SL}_{N-1}}{dt}, \quad \Longrightarrow \quad \frac{dSL_1}{dt} = \frac{dSL_N}{dt} = 0. \tag{4.14}$$

Thus, the units on the extremes of the chain are redefined to be,

$$\frac{dSL_2}{dt} = \left(\frac{d\widehat{SL}_2}{dt} - \frac{d\widehat{SL}_3}{dt}\right)\Big/2 \quad \text{and} \quad \frac{dSL_{N-1}}{dt} = \left(\frac{d\widehat{SL}_{N-1}}{dt} - \frac{d\widehat{SL}_{N-2}}{dt}\right)\Big/2. \tag{4.15}$$

In this form, the summation of the contractile unit lengths can be shown to be constant, in the same way as seen in equation 4.9, meaning the springs are perfectly rigid.

The most rigid substrates, glass and plastic substrates, have rigidities in the order GPa, which far exceeds the stiffness of the cells. However, the cell can not be perfectly held in place by the substrate as the cytoskeleton of the myocyte allow for some rearrangement and movement, and so, as with the “substrate-free" case, although this is an interesting case to consider, it is not physically realistic.

4.2.3 Increased Passive Force

The passive forces included in the Rice model are based on the passive forces in the sarcomere. Primarily, the restorative forces from the titin, which pull the sarcomere back to its rest length, when it has either contracted or been stretched. There is also a passive force from the extra cellular matrix (ECM), however this only activates if the sarcomere is stretched too far and the collagen around the cell prevents it from getting any longer. The passive force of the titin is an exponential function (Eq 4.16) that increases when SL is greater than the rest length, and decreases exponentially when SL is less than the rest length. The passive force is very low when the sarcomere length is close to the rest length.

$$F_{\text{Ti}}(x) = \begin{cases} PCon_{\text{titin}} \times (\exp(PExp_{\text{titin}} \times (x - SL_{\text{rest}})) - 1) & \text{if} \quad x \geq SL_{\text{rest}}, \\ -PCon_{\text{titin}} \times (\exp(PExp_{\text{titin}} \times (SL_{\text{rest}} - x)) - 1) & \text{if} \quad x < SL_{\text{rest}}, \end{cases} \tag{4.16a}$$

$$F_{\text{Col}}(x) = \begin{cases} PCon_{\text{col}} \times (\exp(PExp_{\text{col}} \times (x - SL_{\text{col}})) - 1) & \text{if} \quad x \geq SL_{\text{rest}}, \\ 0 & \text{if} \quad x < SL_{\text{col}}, \end{cases} \tag{4.16b}$$

$$F_{\text{Passive}}(x) = \begin{cases} F_{\text{Ti}}(x) & \text{if} \quad \text{isolated cell}, \\ F_{\text{Ti}}(x) + F_{\text{Col}}(x) & \text{if} \quad \text{trabeculae}. \end{cases} \tag{4.16c}$$

A myocyte will have more passive forces than those acting upon the sarcomere. For example, the isovolumetric nature of the myocyte act as a passive force on the cell. In an effort to capture the passive force of the myocyte, an additional passive force has been added to the system on top of those from the titin and ECM. This additional passive force is a simple linear function,

$$F_{\text{Passive}}(x) = \begin{cases} F_{\text{Ti}}(x) + F_{\text{Lin}}(x) & \text{if} \quad \text{isolated cell} \\ F_{\text{Ti}}(x) + F_{\text{Col}}(x) + F_{\text{Lin}}(x) & \text{if} \quad \text{trabeculae} \end{cases} \tag{4.17}$$

$$\text{where} \quad F_{\text{Lin}}(x) = 0.131(x - SL_0). \tag{4.18}$$

The two forms of the cumulative passive forces can be seen in Figure 4.5a, with the displacements from the two forms of the passive forces seen in Figure 4.5b. The additional passive force causes the contractile unit to return to its rest length very quickly and even briefly becomes longer than its original length, hence the small second peak after the initial contraction. Whereas, the case with the original passive force, returns to the rest length much slower and does not overshoot. It should also be noted that there is little change in the amplitude or contraction duration of the displacement.

The motion detected in the monolayers exhibit a fast return to the rest length, with little to no tail, as seen in Figures 4.1a, 4.1b, and 4.4a. So, the passive force with the additional linear passive force will be used in subsequent simulations.

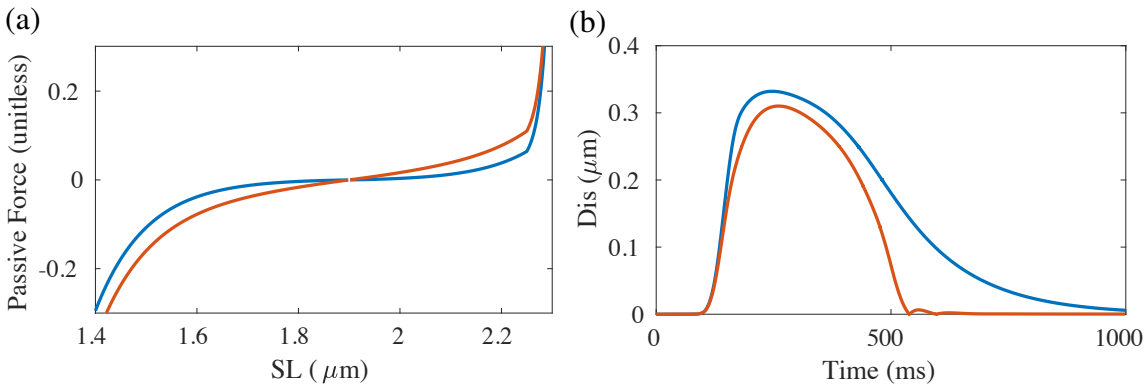

Figure 4.5: a) The original passive force from Rice et al. [88] (blue) and the passive force with an additional linear component (orange) b) The displacement of a single contractile unit, with no external springs, with the original passive force (blue) and with the passive force with an additional linear component (orange).

4.2.4 Numerical Methods

The coupled system of contracting units, like the uncoupled units, is a system of first order differential equations, with stiff initial changes in value. Although the number of ODEs is greatly increased (depending on the number of units), the same variable time step MATLAB solver `ode15s` [99] is sufficient. As discussed in Section 3.3, this solver is a quasi-constant step size implementation of the in built numerical difference formulas, with backward differences, and adequately resolves the features of the simulated results.

4.3 Simulation Results

The coupling of multiple contractile units, with external spring with a range stiffnesses, introduces two key variables to the system; the number of contractile units, n, and the spring constant, K. Both of these values impact the contraction of the units and the motion of the system.

Assuming that each unit acts identically, when the number of units is increased they act against each other and the average displacement of the unit lengths decrease. However, even though the individual units are shortening less, the position increases, as there is a cumulative effect on those on the outside of the chain. The differences in the average displacements and the average positions for a range of n can be seen in Figures 4.6 and 4.7, which have K=0 and K=0.01, respectively (note that K is unitless). In the substrate free case, K=0, when the active force ends, the passive force pulls the units back to its original length with such force the units over correct and take a moment to settle, creating the oscillations seen in Figure 4.6. However, as was discussed earlier, this is not seen in the experiments, as it is not a realistic system. These oscillations are significantly dampened when the springs are attached to the system with spring constants of $K = 0.01$, as seen in Figure 4.7.

The differences due to a change in the spring constant can be seen in Figure 4.8. Note

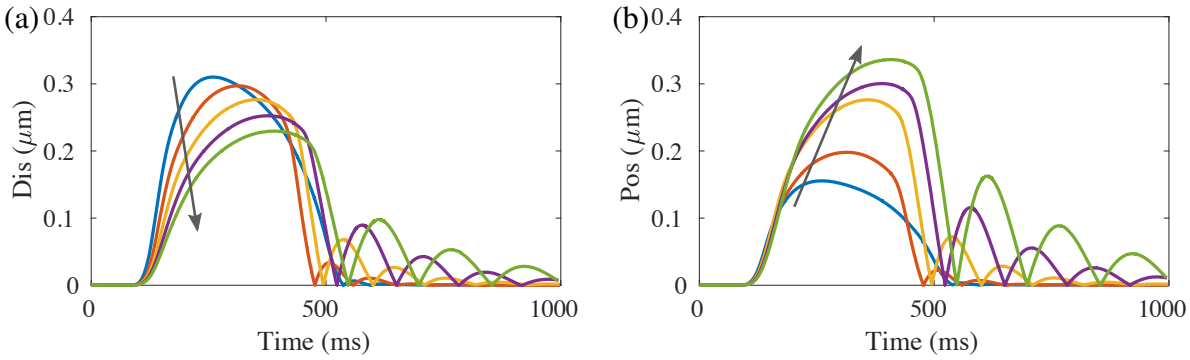

Figure 4.6: a) Average displacements and b) average positions, for a range of n contractile units (increasing from $n = 1$ (blue) to $n = 5$ (green), in the direction of the arrow), with no external springs.

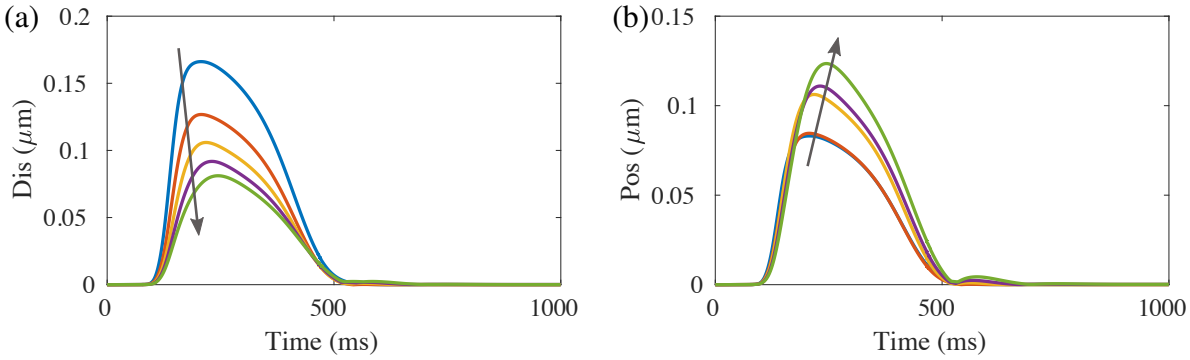

Figure 4.7: a) Average displacements and b) average positions, for a range of n contractile units (increasing from $n = 1$ (blue) to $n = 5$ (green), in the direction of the arrow), with external springs with a spring constant of K=0.01.

that, as there is only one contracting units, the average position is equivalent to half the average displacement and thus the average position is not presented, instead the active force is plotted. Figure 4.8a) shows that the average displacement of the length decreases, which is reflected in the active force generated, which is dependent on the unit length, as seen in Figure 4.8b). Another key impact of increasing K, with identical units, is that the profile of the displacement (and forces) are much more triangular than those at low values of K or as seen in the experimental motions.

Figure 4.9 shows the forces, displacements, and positions of the individual units. Note that the colours of the lines correspond with illustration seen in Figure 4.3, and the black lines are the averages. For the lowest value of the spring constant, K=0.01, the profiles of the displacements and positions are almost identical, with smooth shapes, similar to the uncoupled contraction seen in Figure 4.4. As the K increases, the profiles become more triangular and multi-peaked behaviour appears, although it should be noted that at K=1, the amplitude of the position profiles are approximately 10% of the amplitudes seen when K=0.01.

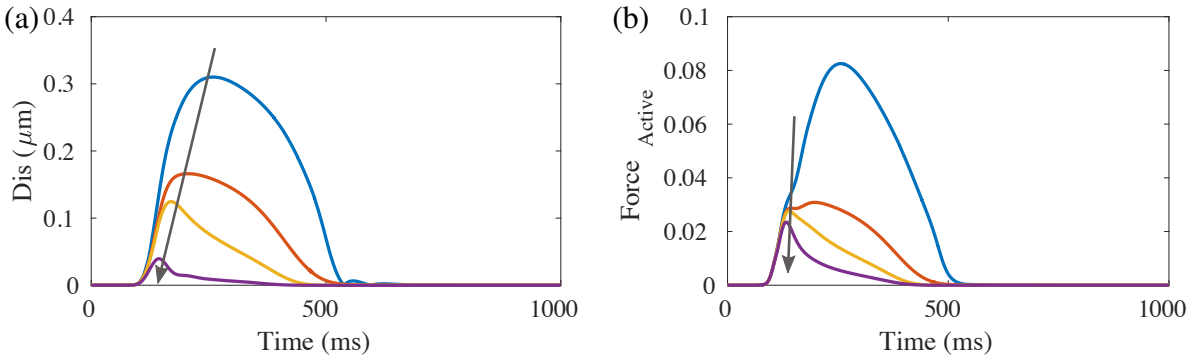

Figure 4.8: a) Average displacements and b) average positions, for a single contractile unit, with a range of spring constants, K =0, 0.01, 0.1, and 1, the direction of the arrow, from blue to purple.

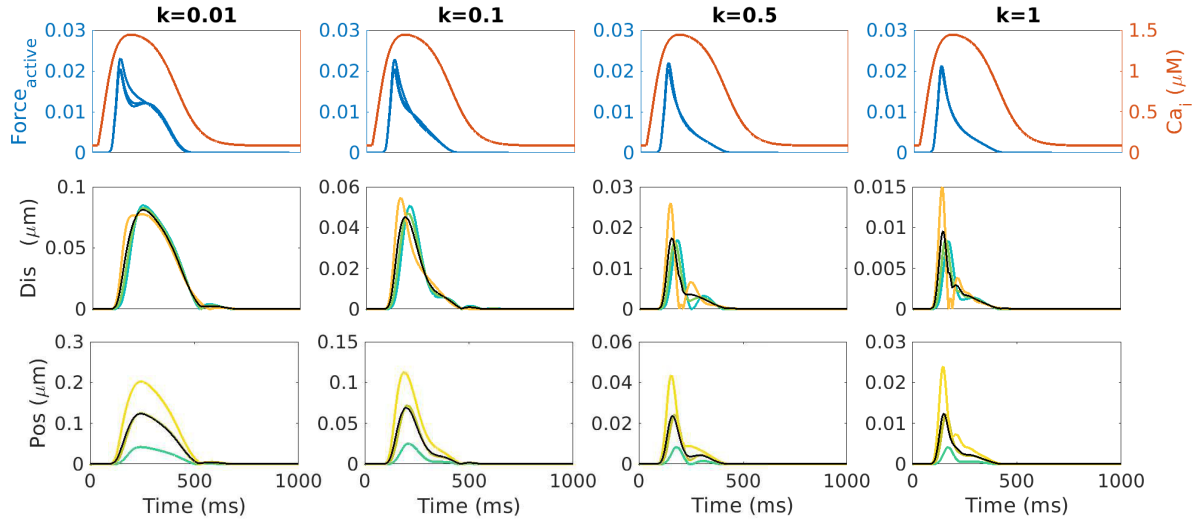

Figure 4.9: Forces, displacements and positions with n=5 and K=0.01, 0.1, 0.5, and 1. The black lines denote the average of the displacements and positions.

4.3.1 Results of including Intercell Variations in Calcium

When the units are identical, if the external springs are very stiff, the units cannot move much as the units are all pulling against each other equally. By introducing variation in the maximum level of calcium in the each unit, at the higher levels of the spring constants, the units are able to move more, this is due to the fact that some units are over-powered by adjacent cells and rather than contracting are stretched.

By changing the maximum level of the calcium, there are significant effects on the displacements and active force. Figure 4.10 shows that as the maximum calcium concentration is reduced to approximately a third of its original value, the recorded displacement and active force are very low, and hardly vary little from their initial values.

Figures 4.11 and 4.12 show the forces, displacements and positions of the individual units, for a range of spring constants, K, when one unit has $[\mathrm{Ca}_i]^{\omega}$ =1.45μM and the others have

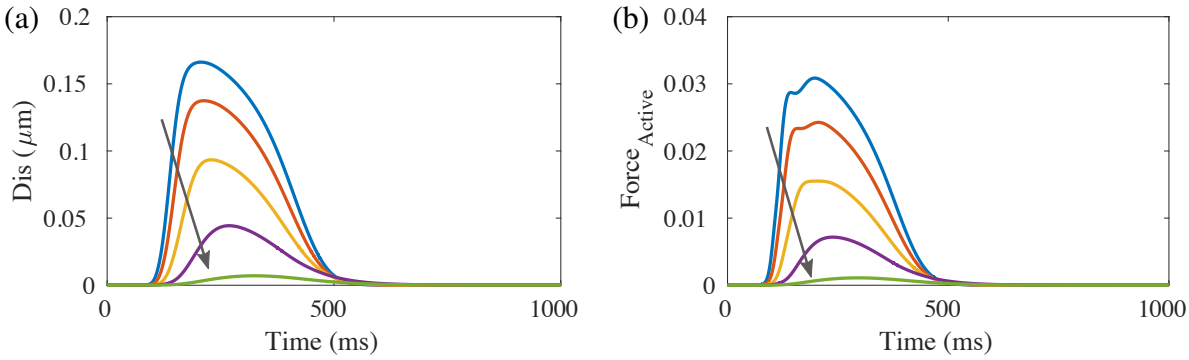

Figure 4.10: a) Average displacements and b) average positions, for a single contractile unit and a spring constant of K=0.01, with a range of maximum calcium concentrations, $[Ca_i]^{\omega}$ =1.45, 1.25, 1.0, 0.75, and 0.5μM, the direction of the arrow, from blue to green.

$[Ca_i]^{\omega}$ =0.5μM, meaning only one unit has sufficient calcium to prompt a significant contraction. Figure 4.11 has the unit with sufficient calcium in the middle unit, and Figure 4.12 shows the profiles when the unit with sufficient calcium is off centre, in this case in the fourth unit out of the five. Both of these cases show almost identical changes in the position for the lowest value of the spring constant, K=0.01. For the larger values of K, the average amplitude of the displacements and positions is greater than in the case with identical calcium profiles (as seen in Figure 4.9). It should also be noted the wider profile and larger amplitude of the averages of the displacements and positions.

Both of these cases show multi-peaked behaviour, however the contractions are also impacted by the location of the unit with sufficient calcium. When this contracting unit is in the middle of the system (Figure 4.11) there is less multi-peaked behaviour than in the case with the contractile unit is off centre (Figure 4.12) and a wider average profile. These cases highlight that the system is impacted significantly by variation in the units and asymmetry in the system.

Naturally, it is unlikely that only one unit will be able to contract within a given system, it is more likely that all of the units will have a range of calcium profiles. Figure 4.13 shows the profiles from a system with 5 contractile units in which the calcium is randomly[1] assigned within 95-100% of the assigned maximum calcium. Even with such minimal changes in the calcium levels a lot more multi-peaked behaviour appears more for high values of K, in comparison to the case with identical units (in Figure 4.9), while the lower values of K show profiles with a single peak.

The amount of variation of the levels of calcium, between the units is difficult to measure in physiology. However, the amount of intercell variation impacts the amount of motion that is recorded in the simulations. This was explored by varying the maximum calcium concentration with a random number generator, with a uniform distribution. The randomly generated number was used to assign a maximum calcium concentration within a prescriber percentage range of

[1]The Matlab function `rand` was used, which generates a random number between 0 and 1, with a uniform distribution [56].

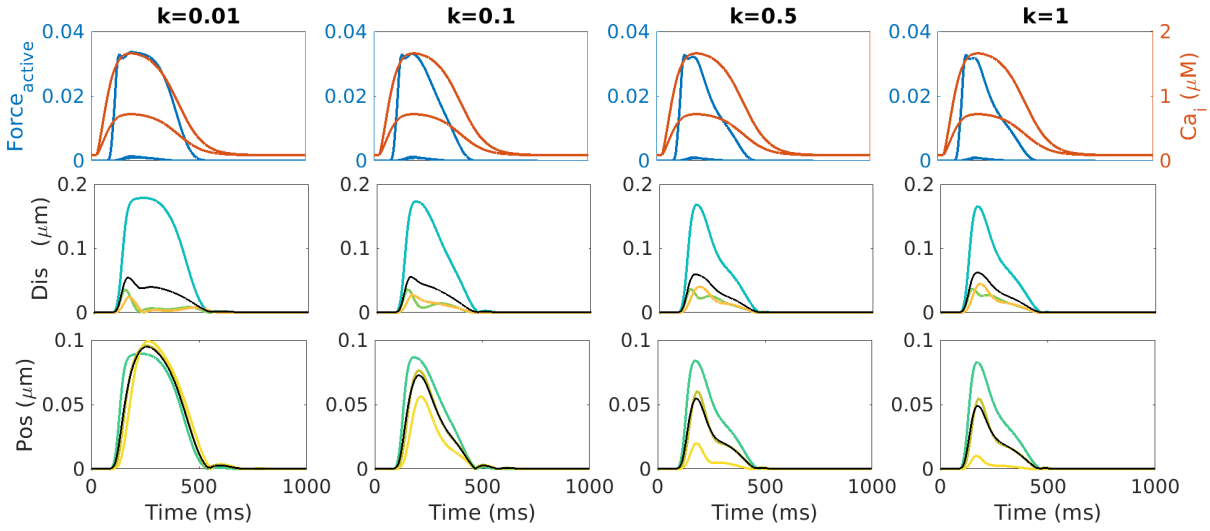

Figure 4.11: Forces, displacements and positions with n=5 and K=0.01, 0.1, 0.5, and 1, when the centre unit has sufficient calcium and the others do not. The black lines denote the average of the displacements and positions, with one contracting unit in the middle of the chain.

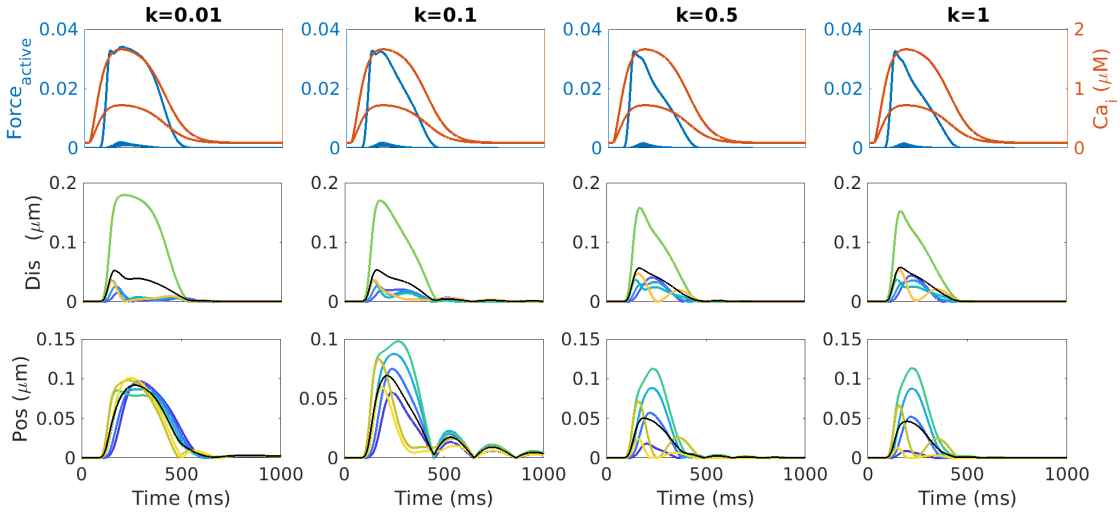

Figure 4.12: Forces, displacements and positions with n=5 and K=0.01, 0.1, 0.5, and 1, when the fourth unit has sufficient calcium and the others do not. The black lines denote the average of the displacements and positions.

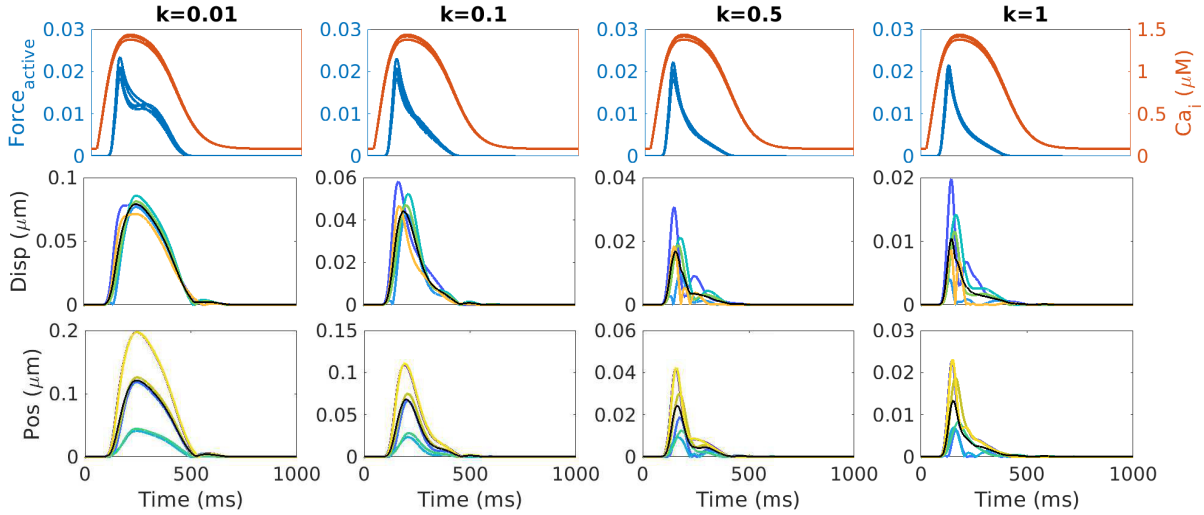

Figure 4.13: Forces, displacements and positions with n=5 and K=0.01, 0.1, 0.5, and 1, with randomly assigned maximum calcium values within a range of 95%-100% of the assigned value maximum calcium concentration. The black lines denote the average of the displacements and positions.

the original maximum calcium, $[\mathrm{Ca}_i]^{\omega}$ =1.45μM. Four percentage ranges were considered. A minimal range of 95-100%, a low level of variation, 75-105%, a medium level of variation, 50-115%, and the highest level of variation, 25-125%. As there is a relatively low number of units, 5 units, the randomly assigned maximum levels of calcium can vary greatly, and thus the simulations were repeated 15 times each and the average was taken of the average position for each set, at the four levels of variation. Note that for each of the levels of variation, the random number generator was reset so the same random numbers were generated in each case.

In Figure 4.14, the average positions, for the four levels of calcium variation with a spring constant of $K = 0.01$, are plotted. Each case shows average positions with similar profiles at a range of amplitudes, as the level of variation is increased the amplitude of the average of the average positions decrease, as seen in Figure 4.16a), this is due to the average calcium level decreasing as the range in the variation increases.

In Figure 4.15, the average positions, for the four levels of calcium variation with a spring constant of $K = 1.0$, are plotted. As the level of variation increases there are greater differences between the average potentials, some showing multiple peaks and few showing a smooth profile, unlike the average positions seen in the K=0.01 cases. Also as the levels of variation increases the amplitudes of the average of the average positions increase, as seen in Figure 4.16b). There is also a change in the shape of these averages of the average positions, with the higher levels of variation showing wider profiles, with a flatter peak.

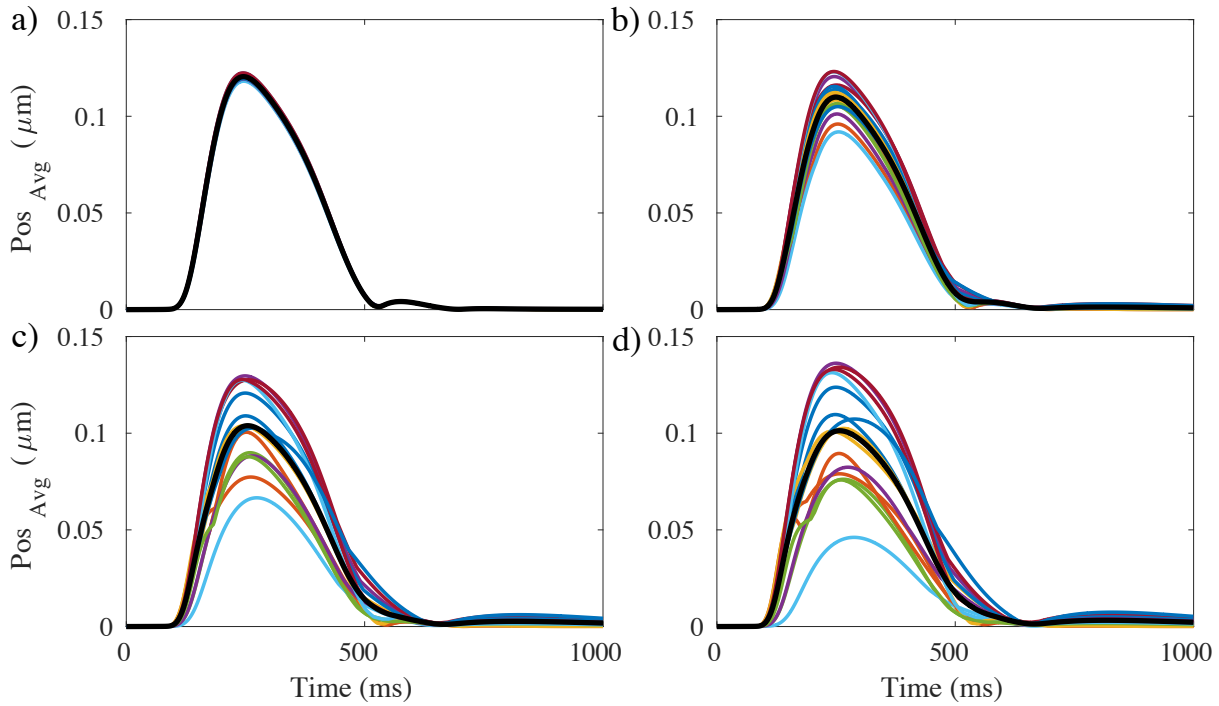

Figure 4.14: Average position from 15 sets of simulations with 5 contractile units, with K=0.01 and randomly assigned maximum calcium concentrations within the ranges: a) the minimal range of 95-100%, b) a low level of variation, 75-105%, c) a medium level of variation, 50-115%, d) and the highest level of variation, 25-125%. The average of the 15 sets of averages is plotted with the thick black line.

4.3.2 Long Chains of Contractile Units

The experiments focus the algorithm on the groups of cells within an assigned small grid, estimated to be approximately five cells [41]. However, The system is part of a larger monolayer with many more cells. So, it is natural to explore simulations with many more units in the chain.

When a long chain of 100 units, with identical calcium profiles, is constructed, despite the weak attachments to the substrate (K=0.01) only the units on the edges can contract, and despite creating an active force, the units in the middle do not contract. However the contraction of the outer units creates a wave and causes the units in the middle to decrease in length, even though the calcium has left the system and thus having no active force. This can be seen in Figure 4.17. It should be noted that, the yellow lines represent the outer units from one end and the green lines are the inner units, but due to the symmetry of the system the lines at the other end cannot be seen in the figure as they are identical to the equivalent lines at the opposite end of the chain. This Figure shows the outer units contracting first and a wave propagating to the centre of the chain, which then meets the wave from the other end of the chain creating a cumulative displacement. The maximum displacement of each unit in the chain is seen in Figure 4.20a) and shows the dependence the unit movement has on its location within the cell. This not a feature seen in the experimental results, this is likely due to attachments to the substrate breaking up the chain. However, this is also does not appear in physiology. All of the units should pull the

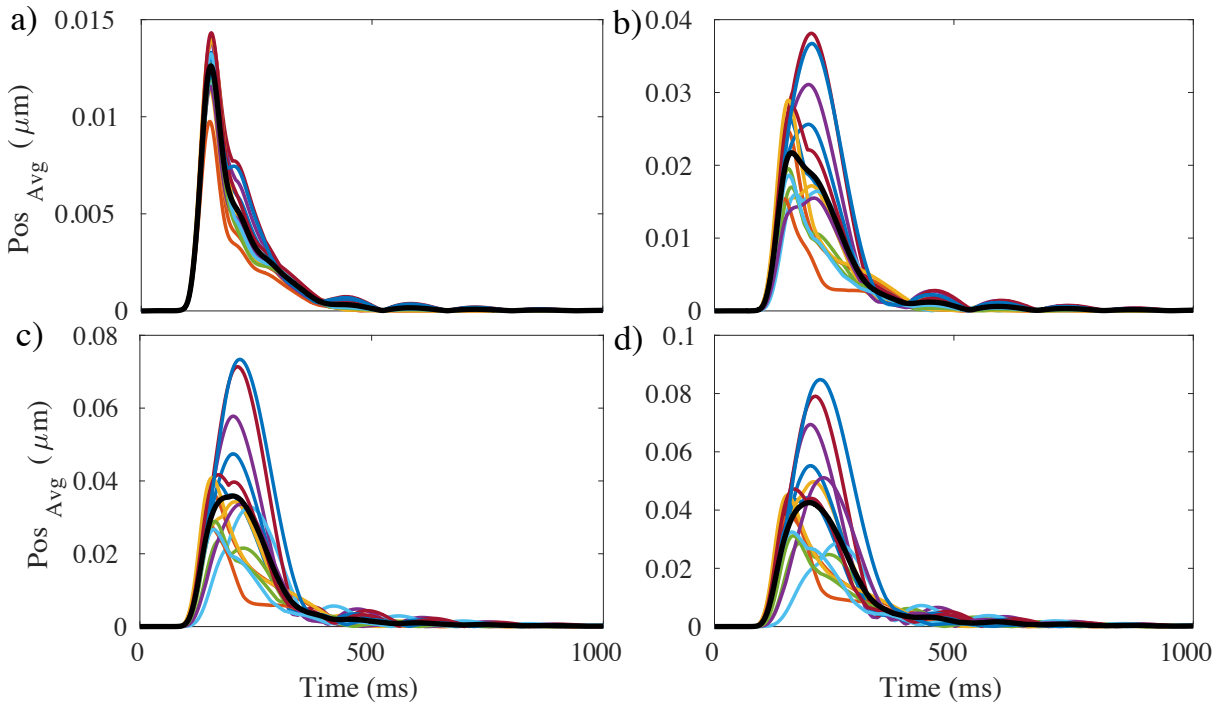

Figure 4.15: Average position from 15 sets of simulations with 5 contractile units, with K=1.0 and randomly assigned maximum calcium concentrations within the ranges: a) the minimal range of 95-100%, b) a low level of variation, 75-105%, c) a medium level of variation, 50-115%, d) and the highest level of variation, 25-125%. The average of the 15 sets of averages is plotted with the thick black line.

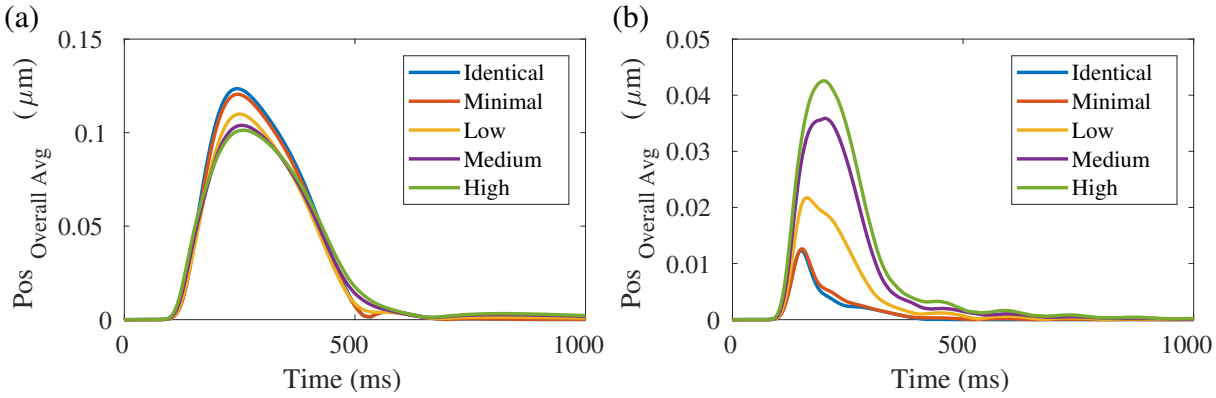

Figure 4.16: a) The average of the average position at five levels of variation of the maximum calcium concentration when, the spring constant is a) $K = 0.01$ and b) $K = 1.0$.

chain at the same time. This is also reflected by the fact that the total length of the chain does not change significantly, as seen in Figure 4.21b).

In an effort to reduce the wave effect and location dependence, calcium variation was introduced with the same uniform distribution seen in Section 4.3.1, specifically uniform distribution of the maximum calcium within the range 75-105% of the original value. This inclusion of the calcium variation did remove the dependence on the location (as seen in Figure 4.20b)), although it did not stop the wave from forming, as seen in Figure 4.18. Also, despite allowing the units

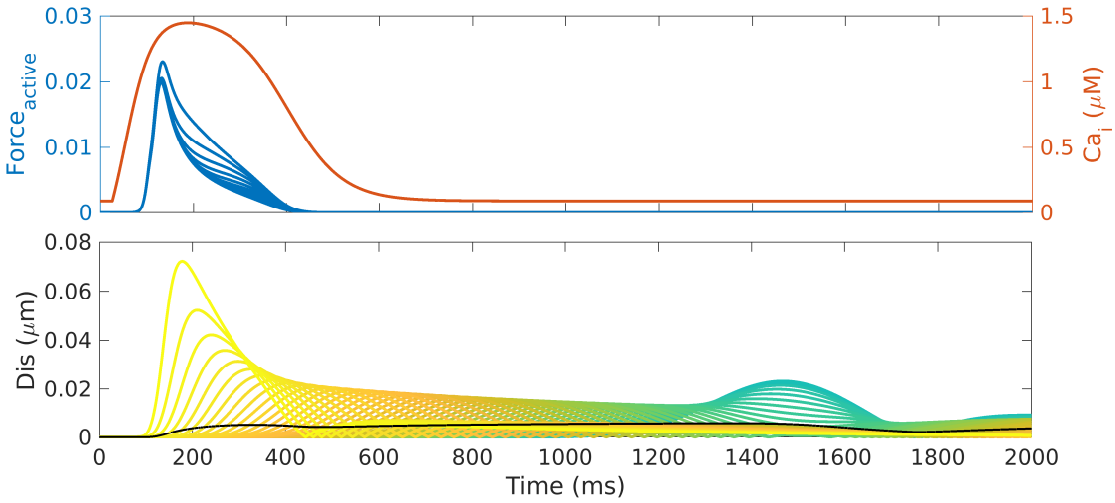

Figure 4.17: Active force and displacement profiles of each unit in a chain of 100 identical units, when K=0.01, with the black line denoting the average displacement.

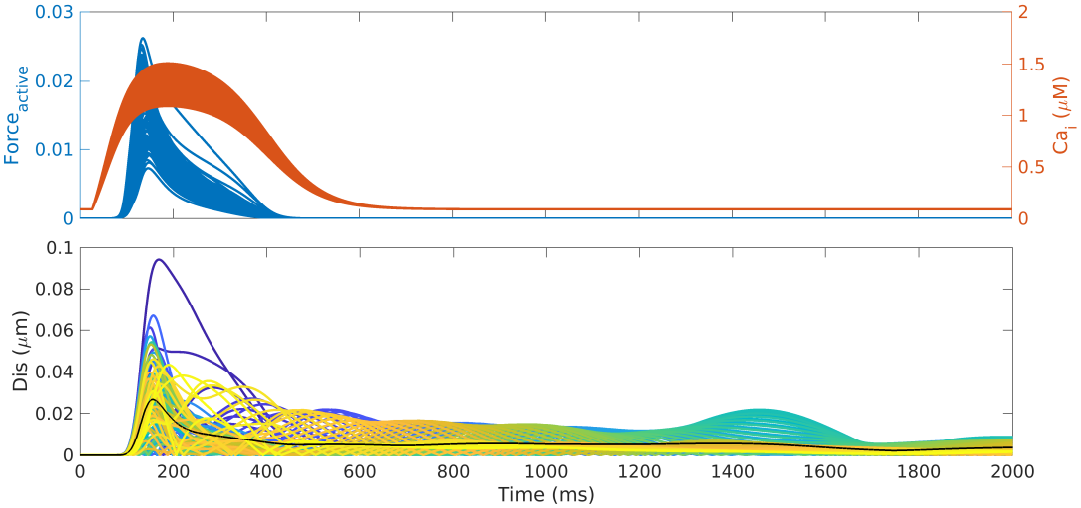

Figure 4.18: Active force and displacement profiles of each unit in a chain of 100 units, when K=0.01, with the black line denoting the average displacement.

in the middle of the chain to move more, any additional contraction in a given unit from the calcium variation is balanced by the stretching of adjacent units, meaning the total length of the chain has a similar length change as the system with identical units, see Figure 4.21b).

The wave can be eliminated by separating groups of contractile units with a simple spring. These springs are modelled in the same way as the external springs, with spring constants of $K = 0.01$. Figure 4.19 shows the forces and displacement of the unit lengths, when a group of five contracting units are separated by a spring, the displacements of the springs are not included. This figure shows the similar levels of displacement, except the waves are buffered by the springs and thus do not form. Figure 4.21a) shows the maximum displacements of the contracting units in this system, showing less dependence on the location within the chain and an increased level of contraction of the units throughout, although the smaller groups of 5 units show some location

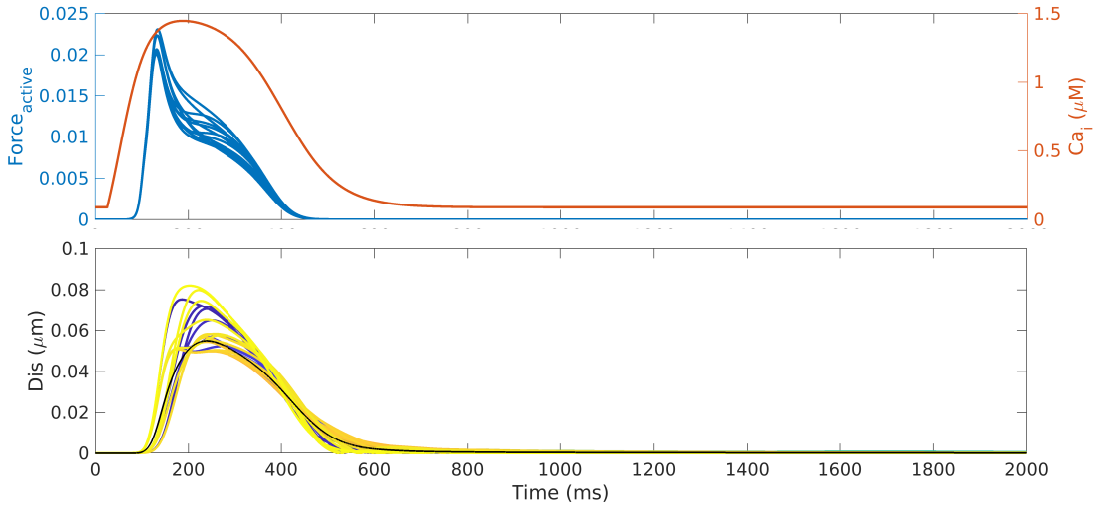

Figure 4.19: Active force and displacement profiles of each unit in a chain of 100 units, where every sixth unit is a spring and all the springs have K=0.01. The black line denoting the average displacement.

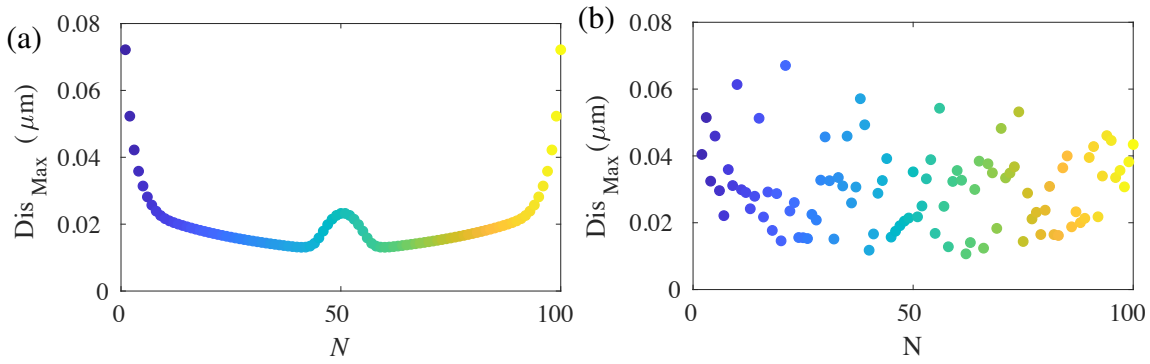

Figure 4.20: Maximum displacements of each unit in a chain of 100 units, when K=0.01, where a) the chain is entirely made of identical contractile units and b) the units have randomly chosen maximum calcium concentrations.

dependence within their groups. Also, despite the increased levels of displacement, the overall length change of the chain is less that the system without the springs separating the units, as seen in Figure 4.21b).

4.4 Discussion

By mathematically modelling a chain of contractile units suspended between two springs, the key characteristics seen in the experimental results have been successfully replicated. Specifically, for a substrate (or spring) with a low stiffness the simulated motion does not exhibit a lot of multi-peaked behaviour, and as the substrate (or spring) stiffness increases, the multi-peaked begins to appear. This behaviour is more pronounced when there is intercell variation in the calcium profiles, with more variation causing more multi-peaked behaviour.

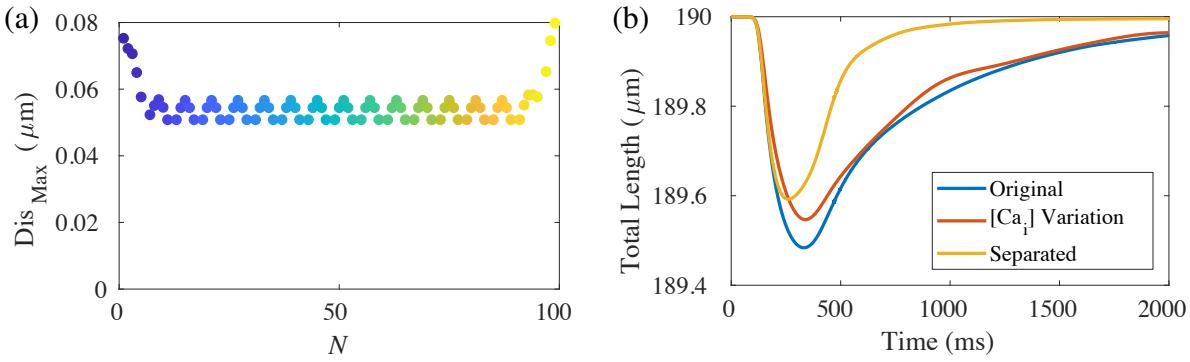

Figure 4.21: a)Maximum displacements of each unit in a chain of 100 units, when K=0.01 where groups of five contracting units are separated by a spring, and b) Total lengths of chains of 100 units and K=0.01, in three different cases. First 100 identical contracting units (blue), second the cases with 100 units with varied levels of calcium (orange) and third 100 units where the coupling is separated by a spring defining every sixth unit.

There are two key differences between the simulated and experimental results. Firstly, there is a delay between the upstroke of the calcium profile and the active force, and subsequently the unit length. However, this discrepancy appears in both the coupled and the uncoupled system and is likely due to the formulation of the active force and crossbridge formation. This is something that would be explored in further work. Secondly, in the cases with increased substrate stiffness, the time courses of the force and movement have a triangular shape and have a significantly reduced amplitude, whereas the experimental results keep a similar shape and amplitude in comparison to the softer substrate cases. This again points towards a flaw in the formulation of the active force, which appears to be significantly affected by the constraints on the movement of the units. Although, this effect is alleviated slightly when the a high level of variation in the calcium profiles introduced, with the average of the average positions having greater amplitudes, greater durations and less triangular shapes. It should be noted that in the experiments, although the profile shape is reliable, the experimental motion traces may not reliably capture the amplitude.

An interesting result of these simulations is that for longer chains of contractile units, the contraction of the units are dependent on the location within the chain. Even with a weak attachment, the units in the centre of the chain are unable to move and the contraction of the units at the edges cause a wave to appear, shortening those units in the middle even after the calcium has left the system and there is no active force. This is a behaviour that does not appear in nature. Also, the total length of the chain does not reduce significantly.

In an effort to remove the location dependence and wave formation, the system is adapted with increasing the level of calcium variation and also by introducing springs between groups of 5 units. By introducing calcium variation, the position dependence is removed, however the wave persisted and the total length of the chain is similar to the case with identical units. When the chain is broken up by springs at every sixth unit (where the contracting units are

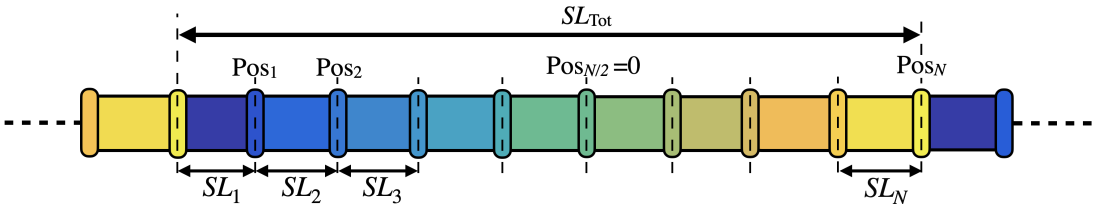

Figure 4.22: Schematic of units attached end-to-end, with periodic boundary conditions.

identical), the location dependence was reduced from the original case and the wave does not appear. Although, as the additional springs in the system stretch, the total length of the chain reduces even less that the other two cases.

Another possible method of avoiding the contraction being dependent on the location within the chain, the coupling scheme could be redefined to have periodic boundaries, as seen in Figure 4.22. Here the first and final derivatives of SL have the same form as the those in the middle, with $d\widehat{SL}_0$ and $d\widehat{SL}_{N+1}$ being defined by the units at the other end of the chain,

$$\frac{dSL_i}{dt} = \left(2\frac{d\widehat{SL}_i}{dt} - \frac{d\widehat{SL}_{i-1}}{dt} - \frac{d\widehat{SL}_{i+1}}{dt}\right)\Big/2 \quad \forall i \in \{1,\ldots,N\} \tag{4.19}$$

$$\text{where} \quad \frac{d\widehat{SL}_0}{dt} = \frac{d\widehat{SL}_N}{dt} \quad \text{and} \quad \frac{d\widehat{SL}_{N+1}}{dt} = \frac{d\widehat{SL}_1}{dt}. \tag{4.20}$$

As with the original scheme to couple the units, it can be shown that the total length is held constant.

$$\frac{dSL_{\text{Tot}}}{dt} = \frac{d}{dt}(SL_1 + \ldots + SL_N) = \frac{dSL_1}{dt} + \ldots + \frac{dSL_N}{dt} \tag{4.21}$$

$$= \left(2\frac{d\widehat{SL}_1}{dt} - \frac{d\widehat{SL}_2}{dt} - \frac{d\widehat{SL}_N}{dt}\right)\Big/2 + \left(2\frac{d\widehat{SL}_2}{dt} - \frac{d\widehat{SL}_1}{dt} - \frac{d\widehat{SL}_3}{dt}\right)\Big/2 + \ldots \tag{4.22}$$

$$\cdots + \left(2\frac{d\widehat{SL}_N}{dt} - \frac{d\widehat{SL}_{N-1}}{dt} - \frac{d\widehat{SL}_1}{dt}\right)\Big/2 = 0. \tag{4.23}$$

By defining the unit length changes with periodic boundary conditions the dependence on position is removed, however it also removes the external springs on either end, and thus severs the attachment to the substrate. In this system, the forces on the units are only those defined in the Rice model, namely the active and passive forces, with the preload and afterload forces removed. It is only the passive force, which will restore the system to its original state, which is dependent only on the unit length. Thus an additional passive force, to represent the connection to the substrate is needed. This would be an opportunity to introduce a passive force that was dependent on the position of the end of the units, rather than purely the unit length, which would prevent cells being pushed or pulled too far away from their original positions. In order to do this, the definition of the system would need to be reconsidered so that the unit lengths are

defined by the positions as well as their internal forces. In the current formulation, the positions are defined by the unit lengths and do not impact the results.

Chapter 5

Mathematical Models of Electrophysiology

In this chapter the origins and derivations of mathematical models of electrophysiology at the single cell and tissue levels are discussed. The method by which these EP models are then coupled is then outlined. Later in this chapter, the numerical methods used to solve both the single cell and tissue level models are outlined. Finally, benchmarking of EP models and resolution tests of the numerical implementation is presented.

5.1 Introduction to Mathematical Models of Electrophysiology

There are two types of mathematical models of electrophysiology. The first is a model of the cellular electrophysiology, known as “ion current models", which model the ion permeability changes through the various channels in the cell membrane and organelles found within the cell, in order to model the transmembrane potential. The second type of model is a simpler qualitative model of the membrane potential and is subsequently called a “membrane potential model". This type of model represents the electrical activity of cells with equations derived using dynamical systems arguments to model the electrical properties [113].

Membrane potential models use far fewer equations than ion current models and offer an adequate description of the electrical activity. A major benefit of membrane potential models is that, through the use of fast-slow analysis, they can be treated analytically, this is discussed further in Keener and Sneyd [45]. An example of such a model is the Fitzhugh-Nagumo model, which was proposed independently by R. Fitzhugh and J. Nagumo in 1961 [26]. The dynamical features of these models can be applied to various chemical, physical and biological systems. These models do not give insight into the internal workings of the cells and are not readily coupled with models of muscle contraction or with EP models of other cells. However, where the membrane potential models lack in physiological detail, they make up for in computational efficiency and are popular when modelling for large scale tissue models where the specifics of

the cellular behaviour or the ion movements are unimportant. The work in this thesis will require coupling with other models and thus we will focus on the more complex “ion current models".

The origins of ion current models were not concerned with the electrophysiology of cardiac cells, but rather of the giant squid axon[1]. In 1952, Alan Hodgkin and Andrew Huxley derived the first quantitative model of the cellular electrophysiology with ionic currents. Their work used the giant axon of a squid, as it was sufficiently large enough to perform physical experiments on, with the equipment available to them at the time. Their work ultimately lead to our understanding of voltage-gated ion channels and the first mathematical model of these channels [34, 35, 36, 37, 38]. They used experimental results and their biological understanding to derive equations for the transmembrane potential, the ion currents, and their associated gating variables. For this work, they were awarded the 1963 Nobel Prize for Physiology and Medicine. These techniques were later applied to cardiac cells by Denis Noble in the 1960s [72, 73], who derived the first ion current model of the purkinje fibres in 1962. Since then many models have been derived for various cardiac cells and for a range of species, such as: humans, rabbits, mice, and pigs. There are also models of human induced pluripotent stem cell derived cardiomyocytes. These models of the ionic current are dependent only on time and assume that there are no spatial effects. The importance of spatial effects in electrophysiology were not considered until Wilfrid Rall’s work on motor neurons [81, 82, 83, 84], which applied the cable equation[2] to electrophysiology.

The work in this thesis utilises three different existing ionic current models of cardiac cells. A model of human atrial cardiomyocytes by Courtemanche et al. [16], a model of human induced stem cell derived cardiomyocytes by Paci et al. [75], and finally a model of mammalian fibroblasts by Morgan et al [63]. Also presented, is a novel model of human embryonic kidney cells (HEK cells), both wild-type HEK cells and those which express the inward rectifying current.

To begin to mathematically model the electrophysiology of a cell, one can consider the potential over the cell membrane as a simple electrical circuit with two components based on the physiology of the cell. Firstly, the movement of ions through the ion channels in the membrane act as resistors. Secondly, the change in electrical charge over the lipid bilayer of the cell membrane acts as a capacitor. This simple resistor-capacitor circuit can be seen in Figure 5.1.

By considering the movement of ions over the membrane as an electrical circuit a simple equation of the transmembrane current can be written,

$$I_t(V,t) = C_{\mathrm{m}} \frac{dV(t)}{dt} + I_{\mathrm{ion}}(V,t). \tag{5.1}$$

The first term on the right hand side is the capacitance, where the C_{m} is the membrane capaci-

[1] Not the axon of a giant squid but the giant axon of a squid.

[2] The cable equation was first considered by Lord Kelvin in 1855 when he studied the transatlantic telegraph cable, and the effects on the conductance over such a large distance [45].

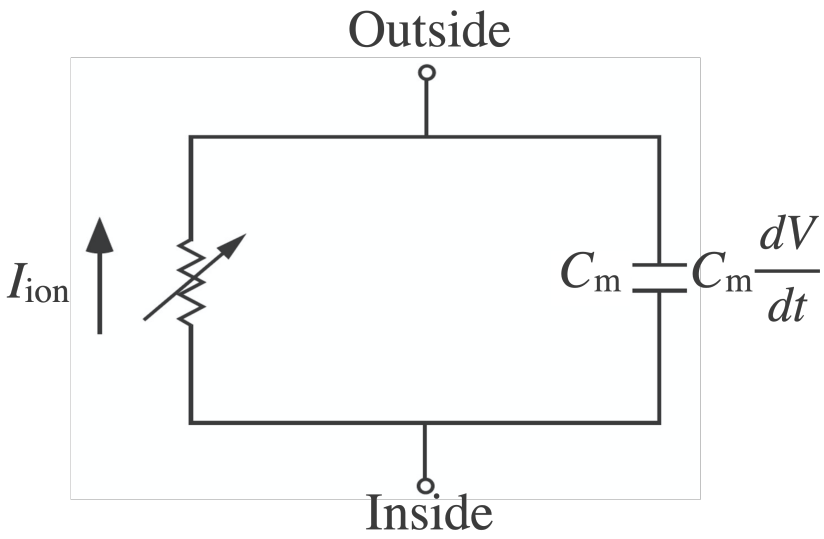

Figure 5.1: Schematic of the transmembrane ion circuit, adapted from [45].

tance (with units in Farads, F). The second term is the current through the ion channels (units in Amps, A). The transmembrane potential is denoted V, which has units of Volts (V).

5.2 Ion Channel Currents

The capacitance of the membrane is determined by the size and surface area of the cell type, and is constant for any given cell type. However, the movement of ions across the membrane, through the respective channels, is much more complex. Ions can be actively moved across the ions through channels known as pumps and exchangers that can move ions across the membrane, even against gradients in their concentration or electrical fields. Alternatively, there are passive channels which allow the movement of ions due to the same chemical gradients and electrical fields [109]. The currents of these channels are commonly modelled by considering either the flux of the ion concentration, or the physiological

The simplest is the passive channel, which has a current defined as,

$$I_{\text{ion}} = G_{\text{ion}}(V - V_{\text{ion}}), \tag{5.2}$$

where, the ion channel conductance for a given ion is denoted G_{ion}, which is the inverse of the channel resistance and has units of siemens[3], S. The channel conductance is generally dependent on the transmembrane potential, V, and its form will vary in each type ion channel. Finally, V_{ion} is the Nernst potential of the ion.

The Nernst potential is a fundamental value within electrophysiology. It is defined as the transmembrane potential generated by the separation of ions across the membrane at thermody-

[3]Siemens are sometimes known as Mhos, (backwards for Ohm, the units of resistance) and is denoted with an upside down capital omega ℧.

namic equilibrium [45].

5.2.1 The Nernst-Planck Equation

Every ion has a unique Nernst potential, dependent on the ion concentrations either side of the membrane. The value can be derived by finding the chemical potential of the ion both internally and externally, then finding the difference across the membrane. The Nernst potential is the transmembrane potential at which the current across the membrane is zero [45].

Alternatively, the Nernst potential can also be found be considering the flux across the membrane. There are two types of flux at play, electrical flux, J_{E} and diffusive flux, J_{D} [109]. The diffusive flux for a given ion is defined by,

$$J_{\mathrm{D}} = -D \bigtriangledown [\mathrm{ion}], \tag{5.3}$$

where D is the diffusion coefficient of the ion and $[\mathrm{ion}]$ is the ion concentration.

If there is no difference in the chemical concentration across the membrane, the flux is entirely defined by the electrical flux, given by Planck's equation,

$$J_{\mathrm{E}} = m\frac{z}{|z|}[\mathrm{ion}]E, \qquad \text{where} \quad m = D\frac{|z|F}{RT}, \quad \text{and} \quad E = -\bigtriangledown \phi, \tag{5.4}$$

where z is the ion charge and the values m and E are the mobility and the electrical field, respectively [109]. The universal gas constant is R, T is the temperature, F is the Faraday constant (a capacitance) and ϕ is the scalar potential.

The summation of the diffusive and electrical flux forms the total flux, J, known as the Nernst-Planck equation,

$$J = -D\left(\bigtriangledown[\mathrm{ion}] + \frac{zF}{RT}c \bigtriangledown \phi\right). \tag{5.5}$$

As discussed earlier the Nernst potential is the potential when there is zero flux, so by considering the flux in only one dimension, across the membrane, and integrating the Nernst-Planck equation when J=0, with respect to this dimension, the Nernst potential can be found,

$$V_{\mathrm{ion}} = \frac{RT}{zF}\ln\left(\frac{[\mathrm{ion}]_{\mathrm{e}}}{[\mathrm{ion}]_{\mathrm{i}}}\right) = \frac{kT}{zq}\ln\left(\frac{[\mathrm{ion}]_{\mathrm{e}}}{[\mathrm{ion}]_{\mathrm{i}}}\right), \tag{5.6}$$

where, $[\mathrm{ion}]_{\mathrm{e}}$ and $[\mathrm{ion}]_{\mathrm{i}}$ are the external and internal ion concentrations, respectively, which are defined when there is no current across the membrane and both sides are electrically neutral. An alternative formulation defines the Nernst potential with the Boltzmann's constant, $k = \frac{R}{N_A}$, where N_A is Avogadro's number and q is the charge on a proton (note that $F = qN_A$). When $V = V_{\mathrm{ion}}$, there is no net current of the ion across the membrane.

5.2.2 Ionic Flux Models

The Nernst-Planck equation (Equation (5.5)) can be used to determine the flux across the membrane, not just its equilibrium point, and can be used to construct models for individual channels. The simplest form of ion flux is the linear form,

$$J_{\text{ion}} = g(V - V_{\text{ion}}), \tag{5.7}$$

where g is the permeability of the channel. This linear flux is used to define the passive ion current and are often used to define background currents. This was already seen in Equation (5.2).

To find the ion flux of with more complex forms one must integrate the Nernst-Planck equation. First consider the gradient of the electrical field to be the transmembrane potential divided by the distance between the internal and external regions, then rearranging Equation (5.5) to be an ODE in terms of the ion concentration,

$$\frac{d}{dx}[\text{ion}] - \frac{zFV}{RTL}[\text{ion}] + \frac{J}{L} = 0, \tag{5.8}$$

where L is the membrane thickness.

Solving this ODE gives the Goldman-Hodgkin-Katz formulation for the ionic flux [109],

$$J = \frac{D}{L}\frac{zFV}{RT}\frac{[\text{ion}]_i - [\text{ion}]_e \exp\left(\frac{-zFV}{RT}\right)}{1 - \exp\left(\frac{-zFV}{RT}\right)}, \tag{5.9}$$

where the subscripts i and e refer to the internal and external values. The term, $\frac{D}{L}$ is the permeability of the membrane, and is sometimes denoted with a P. The flux, J, has units of moles per area per time, which can be converted to the current of the ion, by multiplying the flux by zF, the charge carried in a mole of the ion, giving,

$$I = \frac{D}{L}\frac{z^2F^2V}{RT}\frac{[\text{ion}]_i - [\text{ion}]_e \exp\left(\frac{-zFV}{RT}\right)}{1 - \exp\left(\frac{-zFV}{RT}\right)}. \tag{5.10}$$

This is the Goldman-Hodgkin-Katz current equation, and is used to define many ionic current.

5.2.3 Models of Ion Channel Gates

The second form of model for the ion current considers gates that appear in the channel. A channel may have multiple gates, all which must be open to allow ions to pass through. A simple example of the derivation of the modelling these ion channel gates is the Hodgkin-Huxley model, which derived two such models.

The Hodgkin-Huxley Model

As discussed in Section 5.1, Hodgkin and Huxley were the first to derive models of active ion channels. Their work focussed on the currents of the giant squid axon. Through their experiments they identified a potassium current, a sodium current and small leakage current (which they determined to be so negligible that it could be considered to be constant). They went on to perform voltage clamp experiments for the potassium and sodium channels. They used these experiments to derive equations for the respective ion conductances and introduced 'gates', which actively open and close. Thus, the potassium and sodium conductances, respectively, can be defined as,

$$g_{\mathrm{K}} = \bar{g}_{\mathrm{K}} n^4, \qquad g_{\mathrm{Na}} = \bar{g}_{\mathrm{Na}} m^3 h, \tag{5.11}$$

where, $\bar{g}_*$ is the maximal conductance of the channel, a constant, and n, m, and h are the gating variables. The voltage clamp experiments informed both how many types of gates the two channels have and the order of each gate. These gating variables are determined by simple first order ordinary differential equations with the same fundamental form, with one term opening the gate and a second closing the gate, with a prescribed rate, as seen in Equation 5.12.

In conclusion, Hodgkin and Huxley derived a model for the transmembrane potential of the axon of the giant squid, with 3 ion channels,

$$C_{\mathrm{m}} \frac{dV}{dt} = -\bar{g}_{\mathrm{K}} n^4 (V - V_{\mathrm{K}}) - \bar{g}_{\mathrm{Na}} m^3 h (V - V_{\mathrm{Na}}) - \bar{g}_{\mathrm{L}} (V - V_{\mathrm{L}}), \tag{5.12a}$$

$$\frac{dn}{dt} = \alpha_n (1 - n) - \beta_n n, \tag{5.12b}$$

$$\frac{dm}{dt} = \alpha_m (1 - m) - \beta_m m, \tag{5.12c}$$

$$\frac{dh}{dt} = \alpha_h (1 - h) - \beta_h h, \tag{5.12d}$$

where $\bar{g}_{\mathrm{L}}$ is the constant maximal conductance of the small leakage current and α_* are the rates at which the gates open and β_* are the rates at which the gates close. The specific values of the parameters were determined with further experiments.

The Hodgkin-Huxley equations of the squid axon are simple in comparison with ion current models of cardiomyocytes. Although the form models have similarities, the electrophysiology of cardiomyocytes involves more ion channels, and there have been advancements in the understanding the behaviour of said ion channels.

5.3 Cardiomyocyte Ion Current Models

As discussed in Section 2.3.1, the myocyte AP involves the movement of three types of ions: Sodium, Potassium, and Calcium, each with multiple channels. There are many models of cardiomyocytes. Their differences are dependent on their location in the heart, i.e. the atria or

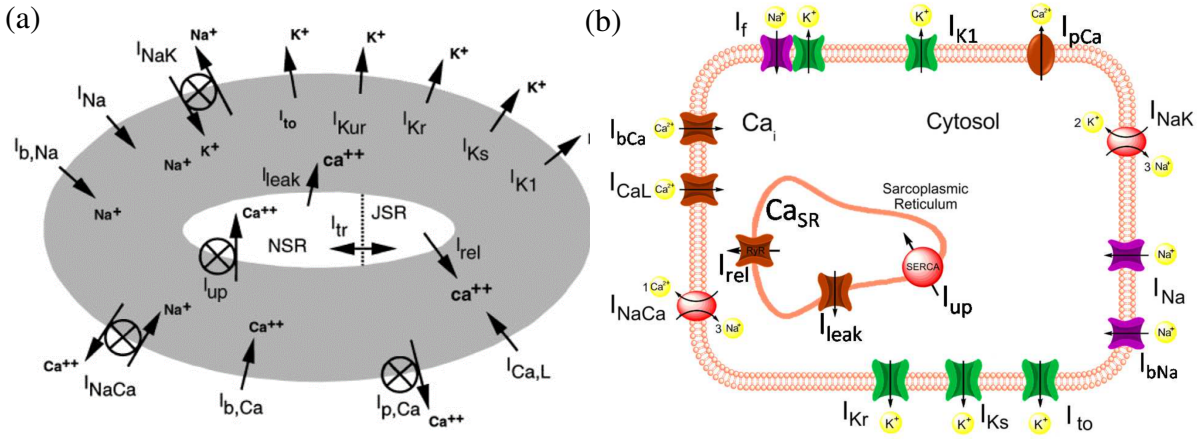

Figure 5.2: Schematic of the ion channels in a) the Courtemanche, Ramirez, and Nattel EP model of an human atrial cardiac myocyte Courtemanche et al. [16] and b) the EP model of a human induced pluripotent stem cell derived cardiomyocyte, by Paci et al. [75].

ventricles, or the species, i.e. human or rabbit. Figure 5.2 shows examples of two cardiomyocyte models, in Figure 5.2a), the ion channel schematic of the human atrial cardiac myocyte EP model by Courtemanche, Ramirez and Nattel [16] (referred to as the CRN model), which will be utilised and discussed in Chapters 6 and 7. Figure 5.2b) shows a schematic from the Paci et al EP model of a human induced pluripotent stem cell derived cardiomyocyte [75], which will be of interest in Chapter 8.

5.4 Tissue Level Models

Considering the electrophysiology of a cell with an ion current model can give an excellent insight into cellular behaviour and are said to be single cell level models, however these models of the transmembrane potentials do not consider how the action potentials propagate, as they have no spatial dependence. To upscale the system to a tissue level model, one uses the monodomain model, which has its origins in the cable equation.

5.4.1 The Cable Equation

The cable equation is derived by first considering the cable as an electrical circuit, consisting of many resistor-capacitor circuits separated by resistors, as seen in Figure 5.3. This creates a discrete representation of the ion transportation across and around the cell membranes.

On either side of the membrane are the two axial currents, $I_i(x)$ and $I_e(x)$ (intra- and extracellular, respectively). They are defined by the differences in potential and the distance between

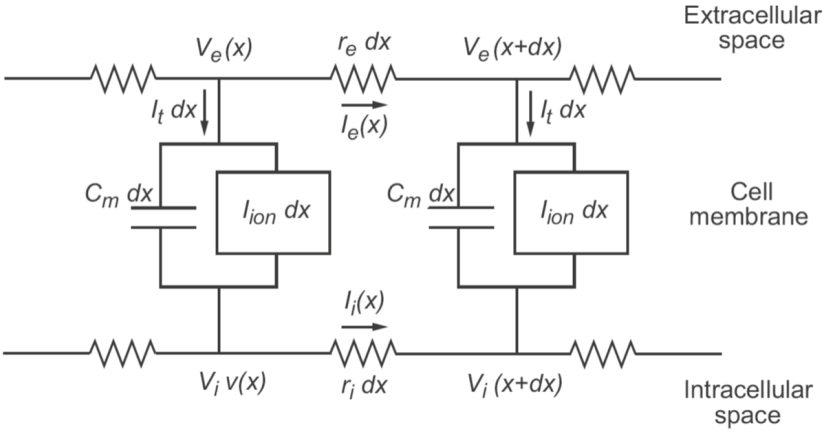

Figure 5.3: Diagram of the circuit elements of the cable equation, from Keener and Sneyd [45]

each circuit for the channels,

$$-I_i r_i dx = V_i(x+dx) - V_i(x) \quad \Longrightarrow \quad I_i = -\frac{1}{r_i}\frac{\partial V_i}{\partial x} \quad \text{as} \quad dx \to 0, \tag{5.13}$$

$$-I_e r_e dx = V_e(x+dx) - V_e(x) \quad \Longrightarrow \quad I_e = -\frac{1}{r_e}\frac{\partial V_e}{\partial x} \quad \text{as} \quad dx \to 0, \tag{5.14}$$

where r_i and r_e are the respective resistances per unit area and $V_i(x)$ and $V_e(x)$ are the respective potentials.

Kirchoff laws define the laws of an electrical circuit, specifically it is known that any change in intracellular or extracellular axial currents must be due to the transmembrane current, I, thus,

$$\begin{aligned} I_i(x) - I_i(x+dx) = Idx &= I_e(x+dx) - I_e(x) \\ \Longrightarrow \quad I = -\frac{\partial I_i}{\partial x} &= \frac{\partial I_e}{\partial x} \quad \text{as} \quad dx \to 0. \end{aligned} \tag{5.15}$$

Note, that there is difference in the sign, as the currents are travelling in opposite directions on either sign of the membrane.

With no external current sources there is a constant total axial current, $I_T = I_i + I_e$. Thus, with the definitions of the axial currents,

$$I_T = -\frac{1}{r_i}\frac{\partial V_i}{\partial x} - \frac{1}{r_e}\frac{\partial V_e}{\partial x}. \tag{5.16}$$

Also, the transmembrane potential is defined to be $V = V_i - V_e$, thus by eliminating the external potential and rearranging,

$$\frac{1}{r_i + r_e}\frac{\partial V}{\partial x} - \frac{r_e}{r_i + r_e} I_T = \frac{1}{r_i}\frac{\partial V_i}{\partial x} = I_i. \tag{5.17}$$

Now, recall the definition of the transmural current from Equation (5.15), and substitute into

Equation (5.17),

$$I = \frac{\partial}{\partial x}\left(\frac{1}{r_i + r_e}\frac{\partial V}{\partial x}\right). \tag{5.18}$$

This transmembrane current is equivalent to the transmural current from the single cell model, Equation (5.1), thus we find that,

$$I = p\left(C_{\mathrm{m}}\frac{dV}{dt} + I_{\mathrm{ion}}\right) = \frac{\partial}{\partial x}\left(\frac{1}{r_i + r_e}\frac{\partial V}{\partial x}\right). \tag{5.19}$$

where p is the perimeter of the cable (or cell) and I_{ion} is the summation of the ion channel currents.

Rearranging ultimately gives the cable equation,

$$C_{\mathrm{m}}\frac{dV}{dt} = -I_{\mathrm{ion}} + \frac{1}{p}\frac{\partial}{\partial x}\left(\frac{1}{r_i + r_e}\frac{\partial V}{\partial x}\right). \tag{5.20}$$

The cable equation is a second order PDE, and can be used to model neurons, a line of myocytes or purkinje fibres.

5.4.2 The Monodomain Model

The cable equation only considers one spatial dimension. Using the same method the cable equation can be upscaled to a 3D model of the transmembrane potential. This gives an equation that still contains values specific to the intra- and extracellular regions, and is hence called the bidomain model,

$$C_{\mathrm{m}}\frac{\partial V}{\partial t} + I_{\mathrm{ion}}\frac{1}{\chi}\nabla\cdot(\sigma_i\nabla V_i), \tag{5.21}$$

$$\nabla\cdot(\sigma_i\nabla V_i + \sigma_e\nabla V_e) = 0, \tag{5.22}$$

where, χ is the surface-to-volume ratio of the membrane and σ_i and σ_e are the intra- and extracellular conductances.

By defining the transmembrane potential to be $V = V_i - V_e$, and the transmembrane conductance to be $\sigma = \sigma_i(\sigma_i + \sigma_e)^{-1}\sigma_e$, the bidomain model can be rearranged to remove the dependence on the internal and external values can be removed. This makes the system only dependent on the transmembrane values and is thus known as the monodomain model,

$$C_{\mathrm{m}}\frac{dV}{dt} = -I_{\mathrm{ion}} + \frac{1}{\chi}\nabla\cdot(\sigma\nabla V), \tag{5.23}$$

The monodomain model is equivalent to the bidomain model, but has fewer variables, and thus is more simply solved numerically. It should be noted that σ is the conductivity tensor and is

defined by the diagonal matrix,

$$\sigma = \begin{pmatrix} \sigma_l & 0 & 0 \\ 0 & \sigma_t & 0 \\ 0 & 0 & \sigma_n \end{pmatrix}, \tag{5.24}$$

where σ_l, σ_t, and σ_n are the conductivity in the three directions of the tissue, named the longitudinal, tissue and normal directions. The conductivity tensor is said to be transversely isotropic as it larger in the longitudinal direction.

5.4.3 Conductance Variation: Length Rescaling

It can be assumed that in the scarred cardiac tissue, the increased levels of collagen cause reduced conductance in the region. Thus, the conductivity parameter, σ, can be reduced to reflect the conductivity in a scar. By changing the conductivity tensor, the conduction velocity changes proportionately and as a result the APD changes proportionately. Thus, to see if there is any effect to the shape of the action potential, the length scale can be rescaled to remove σ from the monodomain equation.

Let, $\hat{x} = \frac{1}{\sqrt{\sigma}}x$. Thus,

$$\frac{\partial}{\partial x} = \frac{\partial \hat{x}}{\partial x}\frac{\partial}{\partial \hat{x}} = \frac{1}{\sqrt{\sigma}}\frac{\partial}{\partial \hat{x}} \tag{5.25}$$

$$\frac{\partial^2}{\partial x^2} = \frac{\partial}{\partial x}\left(\frac{\partial}{\partial x}\right) = \left(\frac{1}{\sqrt{\sigma}}\frac{\partial}{\partial \hat{x}}\right)\left(\frac{1}{\sqrt{\sigma}}\frac{\partial}{\partial \hat{x}}\right) = \frac{1}{\sigma}\frac{\partial^2}{\partial \hat{x}^2} \tag{5.26}$$

Thus

$$\chi\left(C_{\mathrm{m}}\frac{\partial V}{\partial t} + I_{\mathrm{ion}}\right) = \hat{\nabla}^2 V, \tag{5.27}$$

Figure 5.4 shows examples of two APs propagating in one direction with two different conductivities, $\sigma_l = 1.334\mathrm{Sm}^{-1}$ and $\sigma_l = 0.3\mathrm{Sm}^{-1}$. By rescaling the data in the x-direction, the APs have almost the same shape, with minor discrepancies on the repolarisation part of the AP. It should be noted that since the length scale of the system changes the impact of the spatial resolution will also be different in the systems. This will be discussed further, in Section 5.7.

5.5 Coupling of Multiple Electrophysiology Models

In this section the coupling of myocytes and fibroblasts EP models will be discussed, of course the methods used can be applied to multiple cell types, or even variants of the same cell.

To begin to couple multiple EP models, one returns to the resistor-capacitor (RC) circuit. At the single cell level, the RC circuits of the two EP models are resistively coupled in parallel, with one of the first type and multiple of the second. Separated by the intercell conductance,

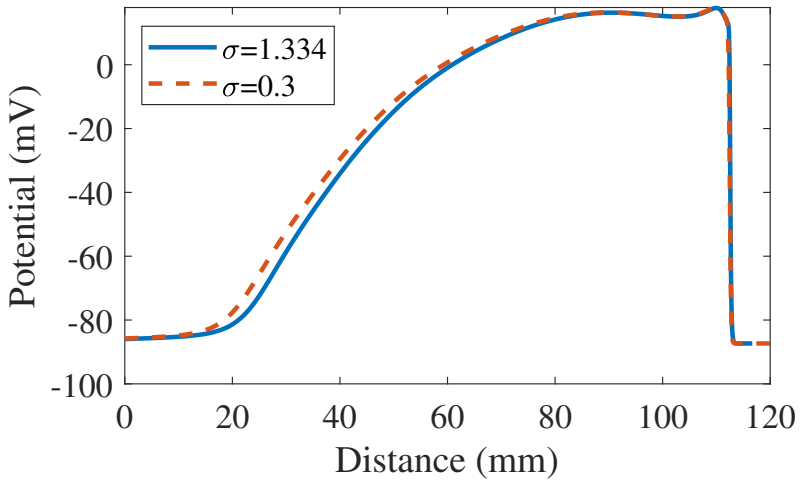

Figure 5.4: Action potentials in the x-direction simulated with different conduction tensors, after being rescaled to remove σ from the system.

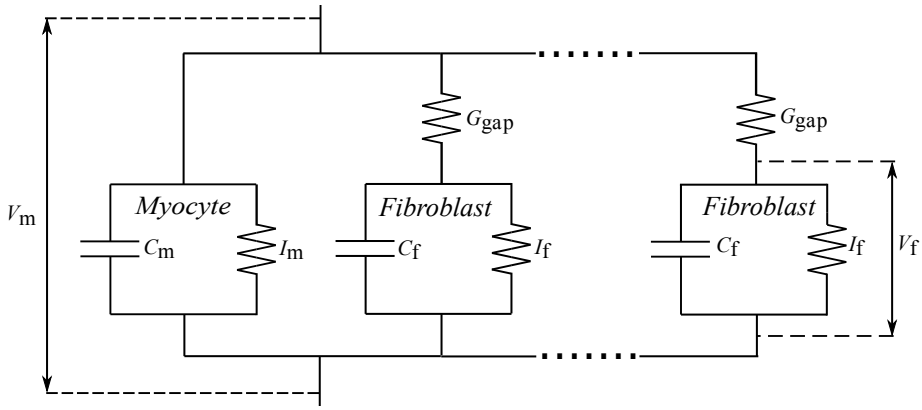

Figure 5.5: A schematic of the electrical circuit of a myocyte with coupled fibroblasts, based on figures in [52].

G_{gap}. A schematic of this system for fibroblasts and myocytes, from MacCannell et al. [52], can be seen in Figure 5.5

From this circuit, the following set of ODEs of the transmembrane potentials of the coupled cells is found,

$$\frac{dV_m}{dt} = -\frac{1}{C_m}\left[I_m(V_m,t) + \sum_{i=1}^{n} G_{gap}(V_m - V_f)\right], \tag{5.28}$$

$$\frac{dV_f}{dt} = -\frac{1}{C_f}\left[I_f(V_f,t) + G_{gap}(V_f - V_m)\right], \tag{5.29}$$

where the m and f subscripts relate to the myocyte and fibroblast form of the variables and constants, respectively. V_* is the transmembrane potentials, C_{m*} is the capacitance, I_* is the summation of the cells' ionic currents, n is the number of coupled fibroblasts (note that n must be a non-negative integer) and G_{gap} is the intercell conductance. Note that the current between

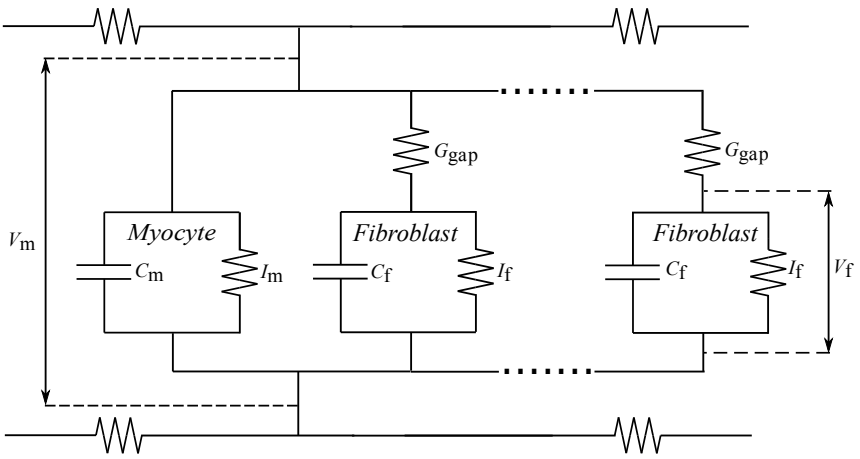

Figure 5.6: Schematic of the electrical circuit of the fibroblasts coupled to the myocyte, based on figures in [52].

the myocyte and the fibroblast is defined to be $I_{gap} = G_{gap}(V_f - V_m)$, where if $I_{gap} < 0$ then the current flows from myocyte to fibroblast.

5.5.1 3-Dimensional Model of Myocyte-Fibroblast Electrophysiology

The coupled system can be upscaled to a tissue level system in the same way as the uncoupled models. Again, the resistor-capacitance circuit, seen in Figure 5.5, is resistively coupled in parallel, which can be seen in Figure 5.6.

The transmembrane potentials of the myocytes and fibroblasts are modelled by the equations,

$$\chi\left(C_m\frac{\partial V_m}{\partial t} + I_m(V_m,t) + n(\mathbf{x})G_{gap}(V_m - V_f) + I_{stim}\right) = \nabla\cdot(\sigma\nabla V_m) \tag{5.30a}$$

$$C_f\frac{\partial V_f}{\partial t} + I_f(V_f,t) + G_{gap}(V_f - V_m) = 0. \tag{5.30b}$$

$$I_* = I_*\big(V(\mathbf{x},t),\mathbf{y}(\mathbf{x},t)\big), \tag{5.30c}$$

$$\frac{\partial \mathbf{y}}{\partial t} = \mathbf{R}\big(V,\mathbf{y}\big), \tag{5.30d}$$

$$\text{for} \quad \mathbf{x}\in\Omega, \quad t\in[0,\infty), \tag{5.30e}$$

with boundary conditions

$$\frac{\partial V}{\partial \mathbf{n}} = 0 \quad \text{on} \quad x\in\partial\Omega, \tag{5.30f}$$

in a spatial domain $\Omega\in\mathbb{R}^3$ representing a piece of cardiac tissue with $\mathbf{n}$ being the outer normal unit vector to the boundary $\partial\Omega$. The transmembrane currents of the myocytes and fibroblasts, I_m and I_f, are modelled as a function of a vector of state variables, $\mathbf{y}$, representing ionic con-

Symbol	Parameter	Value	Unit	Source Ref.
C_{m}	myocyte capacitance	100	pFmm^{-2}	Courtemanche et al. [16]
C_{f}	fibroblast capacitance	6.3	pFmm^{-2}	MacCannell et al. [52]
G_{gap}	intercell conductance	0.5	nS	Morgan et al. [63]
χ	surface-to-volume ratio	140	mm^{-1}	Niederer et al. [71]
$\sigma(\mathbf{x})$	conductivity tensor	$\begin{pmatrix} 0.1334 & 0 \\ 0 & 0.0176 \end{pmatrix}$	Sm^{-1}	Niederer et al. [71]
I_s	stimulus current amplitude	-2000	pA	Courtemanche et al. [16]
x_s	stimulus extent	1	mm	Courtemanche et al. [16]
t_s	stimulus duration	2	ms	Courtemanche et al. [16]
$I_{\text{m}}(V_{\text{m}})$	myocyte current kinetics	variable	pA	Courtemanche et al. [16]
$I_{\text{f}}(V_{\text{f}})$	fibroblast current kinetics	variable	pA	Morgan et al. [63]

Table 5.1: Default values of model parameters and kinetics used in equations (5.30).

centrations and ionic channel gating variables determined by a system of non-linear ordinary differential equations with rates given by **R**. Here it is assumed that fibroblast acts the same, and thus the intercell currents, I_{gap}, of each fibroblast is the same, and the coupling term in Equation (5.30a) is multiplied by n, rather than being a summation term. It is also assumed that the number of fibroblasts per myocyte, n, has spatial dependence. It is also, important to note that dimensional analysis shows that the dimensions of the ionic currents are current densities.

In Chapter 6, the monodomain model with coupled fibroblasts is utilised, specifically with the myocytes being defined by the Courtemanche, Ramirez, and Nattel model of atrial human cardiomyocytes [16], and the model of mammalian fibroblasts by Morgan et al. [62], with the parameters seen in Table 5.1.

5.5.2 Attachment versus Insertion Models

The above model describes an “attachment" model. In such a model each myocyte has a set number of fibroblasts coupled to it (defined by $n(\mathbf{x})$). This is a common and effective way to couple fibroblasts with myocytes however it has limitations in that if the myocyte is removed then the coupled fibroblasts are also removed from the system, thus it is impossible to have tissue that is purely fibroblasts that still has some conductive properties. This limitation is overcome in an “insertion" model where each node it the computational mesh is defined as either a myocyte or a fibroblast, with their associated properties and parameter values. These models also define specific intercell conductances dependent on whether the intercell channels are myocyte-myocyte, fibroblast-fibroblast, or myocyte-fibroblast channels. This allows for incredibly detailed tissues which can have regions of almost entirely fibroblast. An example of such and insertion model is described Xie et al. [122], and an illustration of the myocyte and fibroblast distribution from this insertion model work is shown in Figure 5.7.

Although an insertion model better describes the interaction of fibroblasts and myocytes, the

discrete formulation makes it is much more computationally expensive, as a result a less accurate passive electrophysiology model is used. A passive model does not include fibroblast ionic currents but instead a simpler diffusive term in the fibroblast transmembrane potential equations. Due to the high computational cost, the insertion model was not used in the subsequent chapters, in favour of the attachment model with an “active" fibroblast model.

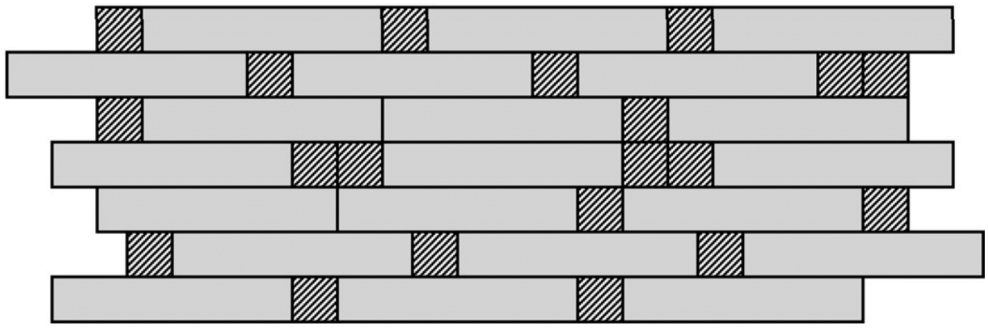

Figure 5.7: Schematic of Fibroblast-Myocyte tissue with random fibroblast insertions in smaller shaded boxes, from [122]

5.6 Numerical Methods for Electrophysiological Models

In this section the methods used to solve the EP models at both the single cell level and the tissue level are discussed.

5.6.1 Single Cell Solutions

At the single cell level, for example the work in Chapter 8, the model is a system of first order ordinary differential equations (ODEs). The action potentials described by this system of ODEs, as with those seen in cardiac tissue, have a fast initial upstroke and thus present a problem that can be described as stiff, requiring a numerical method that can resolve the wave fronts and thus a variable step, variable order solver is used. One such method is utilised in the MATLAB solver `ode15s` [99]. This solver is a quasi-constant step size implementation of the in built numerical difference formulas, with backward differences. This allows for efficient solving, while maintaining a good resolution in the initial upstroke of the AP, as well as the rest of the cycle.

5.6.2 Tissue Level Solutions

To solve the model at a tissue level an operator splitting method is used. This involves solving the single cell ionic models and the monodomain equation separately.

The monodomain model (Equations (5.30)) is characterised by a large range of significant scales, e.g. cardiac action potentials have extremely fast and narrow upstrokes (depolarisation)

and very slow and spread out recovery (repolarisation) phases. An effective numerical scheme based on an operator splitting approach (Godunov and Strang splitting, [108], also known as the fractional time-step method [78]), was proposed by Qu and Garfinkel [80] and is adopted in our study in the following form. The non-linear monodomain model is split into a set of non-linear ordinary differential equations.

In order to obtain numerical solutions of the fibroblast-myocyte monodomain equations the system (5.30) is written in the form,

$$\frac{\partial}{\partial t}\begin{bmatrix} V_{\mathrm{m}} \\ V_{\mathrm{f}} \end{bmatrix} = \mathscr{A}\begin{bmatrix} V_{\mathrm{m}} \\ V_{\mathrm{f}} \end{bmatrix} + \mathscr{B}\begin{bmatrix} V_{\mathrm{m}} \\ V_{\mathrm{f}} \end{bmatrix}, \tag{5.31}$$

where $\mathscr{A}$ and $\mathscr{B}$ are non-linear differential operators defined by

$$\begin{aligned} \mathscr{A}\begin{bmatrix} V_{\mathrm{m}} \\ V_{\mathrm{f}} \end{bmatrix} &\equiv -\operatorname{diag}\left(\frac{1}{C_{\mathrm{m}}}\Big(I_{\mathrm{m}}(V_{\mathrm{m}}) + n(\mathbf{x})\,G_{\mathrm{gap}}(V_{\mathrm{m}} - V_{\mathrm{f}}) + I_{\mathrm{stim}}\Big),\ \frac{1}{C_{\mathrm{f}}}\Big(I_{\mathrm{f}}(V_{\mathrm{f}}) + G_{\mathrm{gap}}(V_{\mathrm{f}} - V_{\mathrm{m}})\Big)\right), \\ \mathscr{B}\begin{bmatrix} V_{\mathrm{m}} \\ V_{\mathrm{f}} \end{bmatrix} &\equiv \operatorname{diag}\left(\frac{1}{\chi C_{\mathrm{m}}}\nabla\cdot(\sigma\cdot\nabla V_{\mathrm{m}}),\ 0\right). \end{aligned} \tag{5.32}$$

Following [80],the classical operator splitting method of [108] is applied and the solution vector $[V_{\mathrm{m}}, V_{\mathrm{f}}]^T_{k\Delta t}$ is numerically approximated after k time steps of length Δt by the following second-order accurate in time, formal θ-scheme with $\theta = 1/2$,

$$\begin{bmatrix} V_{\mathrm{m}} \\ V_{\mathrm{f}} \end{bmatrix}_{k\Delta t} = \left(e^{(1-\theta)\Delta t\mathscr{A}}\ e^{\Delta t\mathscr{B}}\ e^{\theta\Delta t\mathscr{A}}\right)^k \begin{bmatrix} V_{\mathrm{m}} \\ V_{\mathrm{f}} \end{bmatrix}_0 + O(\Delta t^2), \qquad k = 0, 1, \ldots, \tag{5.33}$$

where $[V_{\mathrm{m}}, V_{\mathrm{f}}]^T_0$ are specified initial conditions and $e^X \equiv \sum_{m=0}^{\infty} X^m/m!$ is an operator exponential.

The problems represented by the exponentials of $\mathscr{A}$ consist of a spatially-decoupled non-linear system of stiff ordinary differential equations that describe the ionic models. Due to this operator splitting method, the adaptive time stepping that was used to solve the ionic model at the single cell level can no longer be used. Thus, they are solved using an fourth-order implicit Runge-Kutta method.

The problem represented by the exponential of $\mathscr{B}$ is a linear diffusion equation which is spatially discretised using a low-order finite element scheme and implemented in the open-source parallel C++ finite element library `libMesh` [48], which is similar to the implementation developed in Rossi and Griffith [93]. Specifically, the solution of linear systems and the time stepping relies on the solvers provided by the `PETSc` library[4]. Simulations are run both on our local Linux workstations with 2 Intel(R) Xeon (R) CPU E5-2699 2.30 GHz (up to 72 threads) and 128 GB of memory at the School of Mathematics and Statistics, University of Glasgow as

[4] www.mcs.anl.gov/petsc

well as on the RCUK flagship High-Performance parallel computer ARCHER[5]. VisIt[6] is used for post-processing the two- and three-dimensional simulations.

The High-Performance parallel computer ARCHER was used in select simulations in Section 6.3.4. Certain simulations required an increased resolution due to their specific conditions which caused them to become unstable with the usual spatial and temporal resolution, that was sufficient for the majority of the simulations in that same section. The choice of the resolution is discussed further in Section 5.7. In this section it is discussed that the numerical simulation code has been validated in [64] against the benchmark paper of [71].

5.6.3 Operator Splitting

The complete monodomain model (Equations (5.30)) is integrated over the interval $[t_n, t_n + \Delta t]$ in the three fractional steps of the splitting algorithm. This splits the model into two sets of equations. Firstly, the reaction part which is an initial value problem of the ionic model equations, which are a set of non-linear ordinary differential equations,

$$\frac{\partial V_\mathrm{m}}{\partial t} = -\frac{1}{C_\mathrm{m}}(I_\mathrm{ion}(V_\mathrm{m}, \mathbf{y}) + I_\mathrm{stim}), \tag{5.34a}$$

$$\frac{\partial y}{\partial t} = \mathbf{R}(V_\mathrm{m}, \mathbf{y}). \tag{5.34b}$$

It should be noted that this form includes the variables of both the myocyte and fibroblast models.

Secondly, the diffusion part, a linear diffusion second order partial differential equation,

$$\frac{\partial V_\mathrm{m}}{\partial t} = \frac{1}{\chi C_\mathrm{m}} \nabla \cdot (\sigma \nabla V_\mathrm{m}), \tag{5.35}$$

and then the algorithm solves the two sets of equations at separately using an intermediate time step, $t_n + m\Delta t$. Note that $V^n_{\mathrm{m},\theta} = V_\mathrm{m}(t_n + \theta \Delta t)$.

1. Solve the non-linear ODE system for $V^n_{\mathrm{m},\theta}$ at $t_n < t \leq t_n + \theta \Delta t$,

$$\frac{\partial V_\mathrm{m}}{\partial t} = -\frac{1}{C_\mathrm{m}} I_\mathrm{ion}(V_\mathrm{m}, \mathbf{y}), \quad \frac{\partial \mathbf{y}}{\partial t} = \mathbf{R}(V_\mathrm{m}, \mathbf{y}), \quad V_\mathrm{m}(t_n) = V^n_\mathrm{m} \tag{5.36}$$

   where V^n_m is defined by initial conditions or the previous time-step.

2. Solve the linear PDE for $V^{n+1}_{\mathrm{m},\theta}$ at $t_n < t \leq t_n + \Delta t$

$$\frac{\partial V_\mathrm{m}}{\partial t} = \frac{1}{\chi C_m} \nabla \cdot (\sigma \nabla V_\mathrm{m}, \quad V_\mathrm{m}(t_n) = V^n_{\mathrm{m}\theta} \tag{5.37}$$

[5] www.archer.ac.uk
[6] https://visit.llnl.gov

3. Solve the ODE system again for V_{m}^{n+1} at $t_n + \theta\Delta t < t \leq t_n + \Delta t$

$$\frac{\partial V_{\mathrm{m}}}{\partial t} = -\frac{1}{C_m} I_{\mathrm{ion}}(V_{\mathrm{m}}, \mathbf{y}), \quad \frac{\partial \mathbf{y}}{\partial t} = \mathbf{R}(V_{\mathrm{m}}, \mathbf{y}), \quad V_{\mathrm{m}}(t_n + \theta\Delta t) = V_{\mathrm{m},\theta}^{n+1}. \tag{5.38}$$

Step 3 at a given time is the same as Step 1 at the next time step and so in practice the first and final steps are combined. Also, generally $m = 1/2$ is chosen for the intermediate step. Further details on the operator splitting method applied to the monodomain problem can be found in [109].

5.6.4 Numerical Solution of the Reaction Part

In the above form the problem that is usually stiff, 5.34, can be integrated separately using one of the many known methods for solution of initial value problems. In the following work a fourth-order Runge-Kutta method is used.

5.6.5 Numerical Solution of Diffusion Part

The diffusion part of the above system, 5.35, is solved with use of a finite element method. For the spatial discretisation, the numerical approximation $V_{\mathrm{m}}^h(\mathbf{x},t)$ of the myocyte transmembrane potential is assumed to take the form of a finite expansion in a set of continuous piecewise polynomial nodal basis functions, $\{\phi_i^h(\mathbf{x}), i = 1 \ldots p\}$ with time-dependent coefficient, $\{V_{\mathrm{m},i}(t), i = 1 \ldots p\}$, each representing a nodal value at time t,

$$V_{\mathrm{m}}(\mathbf{x},t) \approx V_{\mathrm{m}}^h(\mathbf{x},t) = \sum_{i=1}^{p} \phi_i^h(\mathbf{x}) V_{\mathrm{m},i}(t), \tag{5.39}$$

where $p = \dim\{\phi^h\}$, and h denotes a parameter measuring the size of the domain partition.

Substituting expansion 5.39 in equation 5.30a, taking the Galerkin projection and using the boundary condition 5.30f, the following weak variational form of the monodomain equation is obtained,

$$\chi C_{\mathrm{m}} \left(\frac{\partial V_{\mathrm{m}}^h}{\partial t}, \phi_i^h \right)_\Omega + \left(\sigma \nabla V_{\mathrm{m}}^h, \nabla \phi_i^h \right)_\Omega = 0 \quad \text{where} \quad i = 1 \ldots p, \tag{5.40}$$

representing a weighted-residual condition for minimization of the residual error, where the round brackets $(v,w)\Omega = \int_\Omega vwd\Omega$ denote the inner product with the basis functions. The Galerkin approximation 5.40 represents a set of p ordinary differential equations in time for the p coefficient functions Vi(t) in the expansion 5.39. For brevity, going forward, the superscript h is dropped.

For the temporal discretisation of the Galerkin projection equations 5.40 the time derivative approximated a first-order accurate forward finite difference formula and the following implicit

numerical scheme is used,

$$\chi C_{\mathrm{m}}\mathbf{M}\frac{\mathbf{V}_{\mathrm{M}}^{n+1}-\mathbf{V}*n_{\mathrm{m}}}{\Delta t}+\mathbf{K}\mathbf{V}_{\mathrm{m}}^{n+1}=0, \tag{5.41}$$

where $\mathbf{V}^n=\left[V_{\mathrm{m},1}^n,V_{\mathrm{m},2}^n,\ldots,V_{\mathrm{m},p}^n\right]$ now denoted the p-dimensional vector of voltage values at time level $t_n=n\Delta t$ with time step Δt, and where

$$\left[M_{ij}\right]=(\phi_i,\phi_j)_\Omega, \tag{5.42}$$

denotes the mass matrix and

$$\left[K_{ij}\right]=(\nabla\phi_i,\sigma\nabla\phi_j)_\Omega, \tag{5.43}$$

denotes the stiffness matrix.

Finally, the vector of unknowns voltage values at time level t_{n+1} is determined by solving

$$(\mathbf{M}+\frac{\Delta t}{\chi C_{\mathrm{m}}}\mathbf{K})\mathbf{V}^{n+1}=\mathbf{M}\mathbf{V}^n. \tag{5.44}$$

5.7 Benchmarking

Our mathematical model and its numerical implementation are validated by comparison with a standard cardiac tissue electrophysiology simulation benchmark case Niederer et al. [71], and is discussed in Mortensen et al. [64]. This benchmarking work calculates the time for the action potential to propagate across a domain, known as the activation time, of a predefined mesh. The domain was measured from one corner to the opposite corner. This domain was defined for a range of spatial steps and system is solved for a range temporal step sizes. This test shows the effects of varying the step sizes on the simulation accuracy. When testing our numerical implementation, our results at Δt =0.0001 ms and Δx =0.1 mm agreed with the benchmark values with the ten Tusscher model, [110] within 2% error. The values recorded for these benchmarking simulations are listed in Tables 5.2a) and 5.2b). The benchmark work uses the ten Tusscher model, however this work also repeated the test with the Weiss model [53], a model of rabbit ventricular myocytes in order to explore is the numerical implementation as a form of resolution test.

From these simulations it is clear, for both models, that the solution is significantly affected by the spatial resolution, becoming more accurate as the resolution increases. The spatial resolution strongly impacts the activation times, however when the temporal resolution is varied there is little change in the activation time. However, as seen with the solutions from the Weiss model (see Table 5.2b)) if the temporal resolution is not increased when the spatial resolution is increased the solution may not converge, and the simulation will fail. Of course, with the increase of the resolution, the computational cost increases, and thus for large simulations a balance must

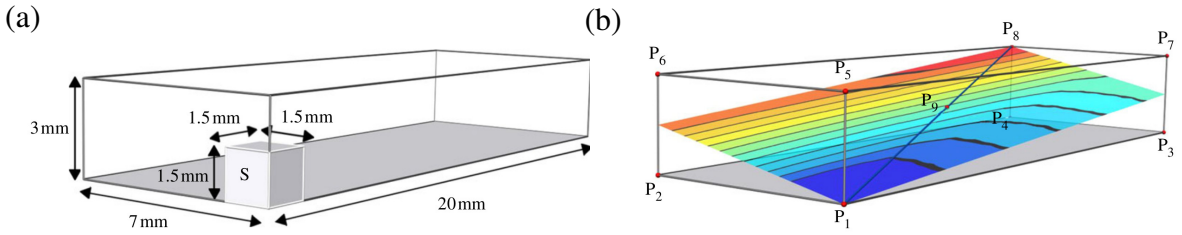

Figure 5.8: Schematic of mesh from the benchmark paper, [71]. (a) mesh and stimulation location dimensions. (b) cross-section of the mesh of interest.

Figure 5.9: Cross-section from benchmark tests with the Weiss model, where $\Delta x = 0.1$mm and $\Delta t = 0.005$ms.

be struck between the accuracy of the simulations and the computational cost. For the majority of the simulations in this work, the chosen spatial mesh size of 0.1 mm is required, with a time step of 0.005 ms. Some simulations in Chapter 6, required a higher resolution, which will be discussed in that chapter.

In subsequent chapters the Weiss model is not used, however this model is representative of many cardiac EP models, in particular its sharp initial upstroke appears in all cardiac EP models and is very stiff. Due to the stiffness of the ionic current system, a high-resolution spatial mesh with typical size 0.1 mm and a time step of 0.005 ms is required to resolve the upstrokes of propagating action potentials, without being unreasonably computationally expensive. Although some direct numerical simulations presented in Section 6.3.4 require an even higher resolution of 0.05 and 0.025 mm, due to these specific cases being close to a threshold, that will be discussed in the section.

a)	Δx (mm)			
Δt (ms)	0.5	0.333	0.2	0.1
0.05	81.75	60.95	52.15	47.20
0.025	80.70	59.85	50.72	45.40
0.010	80.06	59.20	49.94	44.26
0.005	79.82	58.96	49.65	43.85

b)	Δx (mm)			
Δt (ms)	0.5	0.333	0.2	0.1
0.01	X	X	X	54.19
0.005	X	X	63.94	53.91
0.0025	X	82.30	63.81	53.76
0.0001	X	82.25	63.75	53.68

Table 5.2: Activation times from mech cross section with a) the ten Tusscher-Panfilov model [110] and b) the Weiss model [53]. X marks simulations that failed.

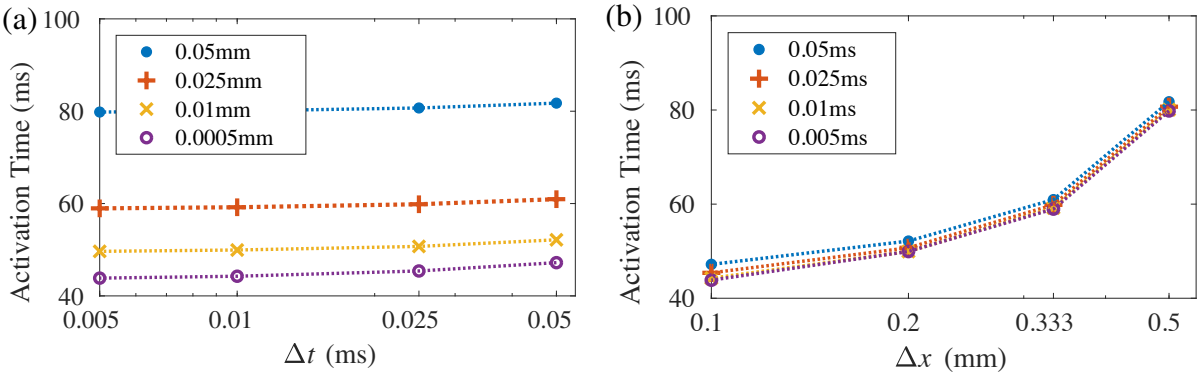

Figure 5.10: Results from benchmark tests with ten Tusscher-Panfilov model.

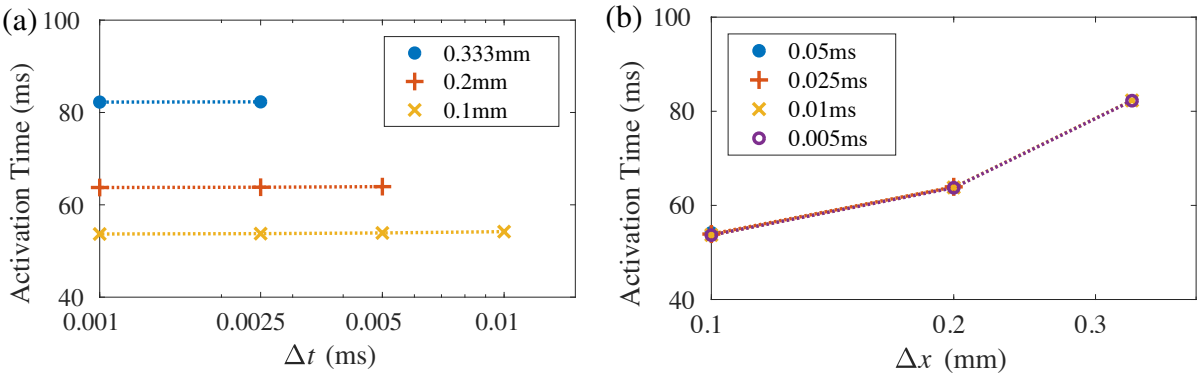

Figure 5.11: Results from benchmark tests with Weiss model.

Chapter 6

Direct Numerical Simulations of Action Potential Propagation after Coupling Myocytes and Fibroblasts

In this chapter, the effects of coupling myocyte and fibroblast electrophysiology models are explored. In particular how this coupling can cause the action potential to fail to propagate in three fundamental pattern of fibroblast density, seen in histology of fibrosis. At the end of the chapter, the differences between fibroblasts and myofibroblasts are explored.

6.1 Introduction

As discussed in Chapter 1, when a myocardial infarction occurs, a region of tissue is damaged, causing the process of fibrosis to start. This introduces increased levels of fibroblasts, the cells that produce the collagen and the extra cellular matrix. Like myocytes, fibroblasts can conduct electricity. However, unlike myocytes, the fibroblast is not active. Meaning that, when the fibroblast is stimulated, there are no voltage gated time-dependant channels that would support an action potential (AP). Instead, the potential just decays away when the stimulation stops. It is clear from experiments that connections form not only between myocytes and between fibroblasts, but also there are intercell connections between myocytes and fibroblasts [49, 77]. So, when fibroblasts are coupled with myocytes, they will conduct will conduct electricity, but if there are too many fibroblasts compared to the number of myocytes then the passive component will dominate over the active elements of the cardiomyocyte component.

In previous studies, there has been extensive work on mathematical modelling the coupling of myocytes and fibroblasts. Namely, work by Kohl et al. [50] and MacCannell et al. [52] coupled myocyte EP models with passive and active fibroblasts EP models, respectively. These two models of the coupled myocyte and fibroblast cells are the basis of many subsequent myocyte-fibroblast models. The work by Kohl et al coupled fibroblasts with sino-atrial myocytes, whereas

the work by MacCannell et al couples a mammalian model of fibroblasts with the ventricular myocyte model, by ten Tusscher et al [111]. Both the passive and active models show increased the action potential duration and decreased AP amplitude. However, the passive models have no significant effect on the myocyte currents. Whereas, the active models show significant changes to some potassium and calcium currents of the myocytes. Many newer models explore the arrhythmogenic properties of fibrotic tissue. This work has involved 2D slabs with spiral waves [68, 106]. Sridhar et al. [106] actively couple myocytes and fibroblasts, the fibroblasts randomly distributed across the region. They showed how increasing the conductance of the L-type channel increases arrhythmogenesis. They also distinguish between two types of fibroblasts; regular fibroblasts and myofibroblasts, which are distinguished by having an increased cell capacitance and an increased uncoupled resting potential for the myofibroblasts. Work by Nayak et al. [68] use a passive model to show that as the intercell conductance (or coupling strength), is increased the AP plateau amplitude decreases and the resting potential increases and also if the number of coupled fibroblasts increases the resting potential and action potential duration (APD) decrease. They also show that if the number of coupled fibroblasts is too high the AP can not be generated and autorhythmic properties or oscillatory behaviours appear.

Beyond single-cell EP dynamics and 2D spiral waves, more realistic 3D geometries of atria have also been studied [62, 63]. In the study by Morgan et al. [62] they compare the arrhythmogenic properties of fibrosis and ionic remodelling as well as the combination of these two features and showed how they reduced the wave length compared to the control case. To model fibrosis they coupled the CRN model of human atrial myocytes [16] and developed the fibroblast model by MacCannell et al. [52] to be specific to atrial fibroblasts. They showed an increased number of fibroblasts also decreases the wave length. In the paper by [63] they consider four causes of atrial fibrillation: 1) ionic remodelling [15], 2) uniform myocyte-fibroblast coupling 3) uniform myocyte-fibroblast coupling with increased tissue anisotropy and 4) patchy fibrosis defined by patient specific atrial fibrosis. In the first three cases atrial fibrillation-like patterns were only seen in the case with combined myocyte-fibroblast coupling and increased anisotropy. The patient specific fibrosis case shows evidence again of sustained rotors seen in atrial fibrillation patterns. However, the patient specific fibrosis patterns are very complex and so it is difficult to assess to what extent the pattern causes the sustained rotors, if at all, and if so what features of the pattern causes them.

In the literature there is little thorough research into how the coupling of the myocytes and fibroblasts affects the spatial propagation of the AP in 1 dimension, or simple changes in the number of fibroblasts across a 1D or 2D region. This is key to understanding the effects of the coupling before more complex and realistic geometries of organs can be considered.

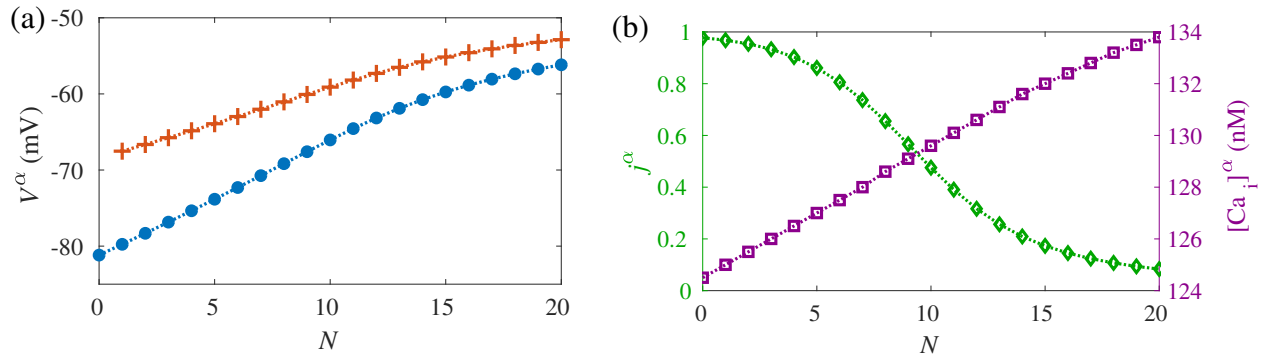

Figure 6.1: The change in the resting values of (a) the myocyte potential, V_{m}^{α}, (•'s) and fibroblast potential, V_{f}^{α}, (+'s) over a range of N and (b) the change in the resting value of the gating variable j, against N.

6.2 Single Cell Simulations

In this section, the results of coupling myocyte and fibroblasts at the single cell level are discussed.

One of the first notable effects of coupling myocytes and fibroblasts, before the AP is even stimulated, is that the equilibrium values change when the fibroblasts are coupled. Figure 6.1 shows the change in the resting values of the myocyte and fibroblast potentials, V_{m}^{α} and V_{f}^{α}, respectively, the gating variable j and the calcium concentration. The gating variable j is the slow variable in the sodium current and is of interest in Chapter 7, where it is discussed further.

The action potential should be stimulated when the system is at rest, thus before the stimulation current is applied to the system it is allowed to come to a rest. Once the system has come to its new resting levels the AP can be stimulated. The action potentials of myocytes and fibroblasts can be seen in Figure 6.2. These examples of APs show the same behaviour that was described in the previous work, namely the reduced peak amplitude, and the change in the action potential duration (APD). Where APD_{30} and APD_{90} is measured to be the time between the initial upstroke and the time when the AP is 30% and 90% repolarised. These recorded values are seen later in Figure 6.6. Note that the system was allowed to rest for 1,000ms before the stimulation, and then the time was rescaled to start at 0ms to more easily see the time course.

6.3 Tissue Level Simulations

In this section, results from direct numerical simulations of equations 5.30 are presented for the three choices of fibroblast distribution, which are introduced in Section 6.3.1. In each of these cases numerical values are provided for selected biomarkers typically used to characterise propagation in experimental measurements. In particular, we report values of conduction velocity, peak potential, peak intracellular calcium transient, APD_{30}, APD_{90} and the normalised

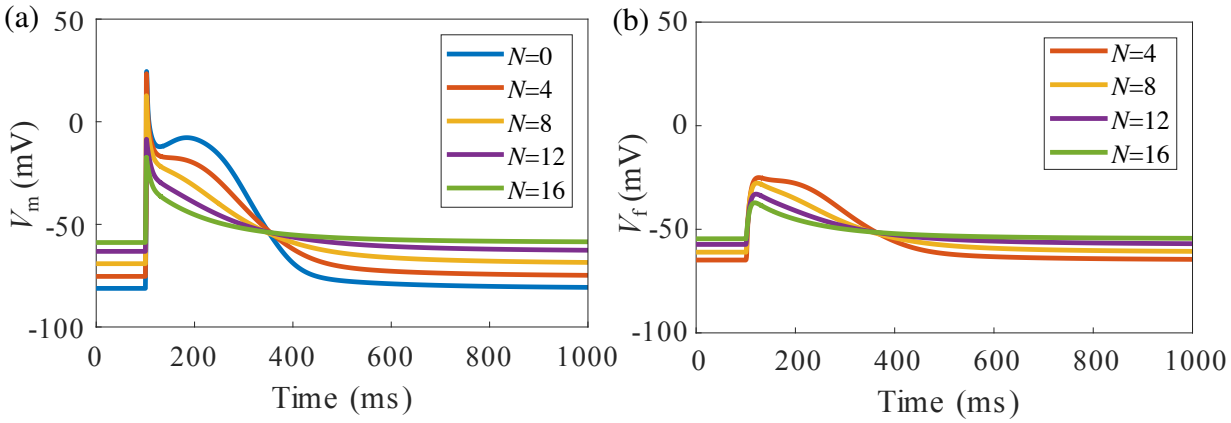

Figure 6.2: Change in myocyte and fibroblast potentials, against time, for a range of N.

triangulation index as functions of the number of fibroblasts per myocyte.

6.3.1 Defining the Fibrotic Region

When fibrosis occurs there are three key properties. The fibrotic region has an increased density of fibroblasts. The second property is the size and shape of the region. Both of these properties are defined by $n(x,y)$. The final property is an increased density of collagen, which decreases the conductivity of the tissue, thus is defined by $\sigma(x,y)$. In order to focus was on the effects of the increased presence of fibroblasts it was assumed that the conductivity is constant over the tissue, and as discussed in Section 5.4.3 variation of $\sigma(x,y)$ is functionally a space scale parameter, and does not impact the electrophysiology of the cells.

When a fibrotic scar that is formed, the scar is not uniform but it has patches and strands of increased fibrosis. In Figure 6.3a) an example of fibrosis histology from [123] is shown, when the collagen is stained red, and the regular conductive tissue is yellow, it can be assumed that the regions with increased levels of collagen also have increased numbers of fibroblasts. It is not possible to distinguish between myocytes and fibroblasts at this scale. The patterns in the collagen show a complex series of strands and patches and an overall increase in collagen across the space. An illustration of fibrotic tissue is shown in Figure 6.3b), again with the yellow regions showing the healthy non-fibrotic tissue and red regions have an increased fibroblast density. This figure highlights three cases of interest. The first case is uniform fibrosis where $n(x,y)$ is assumed to be constant. This case will be referred to as C1. Figure 6.3b) labels two cases of uniform fibrosis, C1a is healthy, fibroblast-free case where $n(x,y) = \mathbf{0}$ and C1b shows uniform fibrosis, where n is a constant positive integer. The second case is tissue that is separated by a patch of fibrosis, labelled C2. The final case (C3) is a thin strand of healthy tissue between fibrotic regions, labelled C3. These three cases raise the questions: how does AP propagation vary between C1a and C1b? How wide can the fibrotic patch in C2 be to allow propagation? How thin can the strand in C3 be to allow propagation?

For the three fundamental fibroblast distributions, $n(x,y)$ is defined to be,

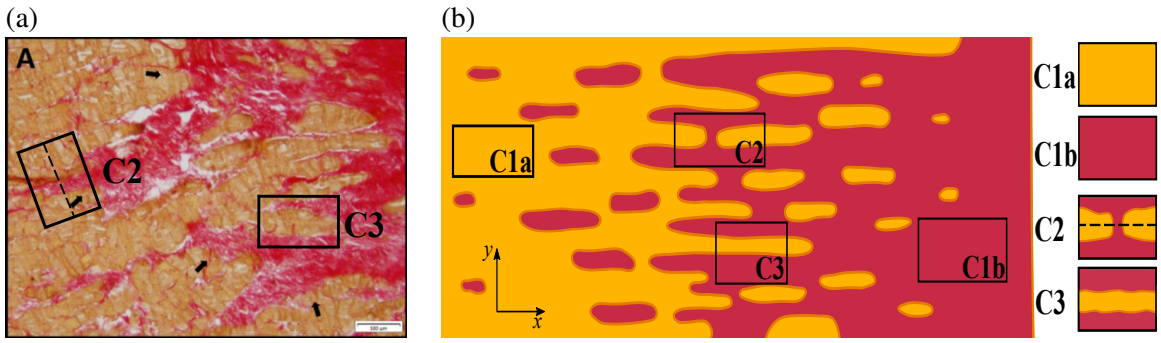

Figure 6.3: (a) An example of fibrosis in a specimen of cardiac tissue with collagen stained in red and intact myocardium shown in yellow from [123] and adapted and shown with permission in Mortensen et al. [65]. (b) A schematic illustration of a border zone between intact myocardium (to the left) and fibrosis (to the right) where the darker shaded areas indicate increased fibroblast density. The rectangular regions denoted in (b) correspond to the specific forms of the fibroblast distribution function $n(x,y)$ considered, see text. These figures are published in Mortensen et al. [65].

C1. Uniform fibroblast distribution prescribed by

$$n(x,y) = N, \tag{6.1a}$$

where N is a constant over the entire domain. This case is schematically illustrated in boxes C1a and C1b of Figure 6.3(b) with $N = 0$ describing intact myocardium with no fibroblasts and $N > 0$ indicating N fibroblasts attached to each myocyte, respectively.

C2. "Fibroblast barrier" distribution prescribed by

$$n(x,y) = N H\big((L_x/2+\Delta x)-x\big)H\big(x-(L_x/2-\Delta x)\big), \tag{6.1b}$$

where intact myocardium with no attached fibroblasts is separated by a rectangular region of constant width Δx extending uniformly in the y-direction where N fibroblasts are attached to each myocyte. This case is a simplification of the situation schematically illustrated in box C2 of Figure 6.3(b).

C3. "Myocyte strait" distribution prescribed by

$$n(x,y) = N\left(H\big((L_y/2-\Delta y)-y\big)+H\big(y-(L_y/2+\Delta y)\big)\right), \tag{6.1c}$$

where intact myocardium, in the shape of a rectangular region of constant width Δy, extends uniformly in the x-direction and channelled by fibrotic regions on both sides where N fibroblasts are attached to each myocyte. This case is schematically illustrated in box C3 of Figure 6.3(b).

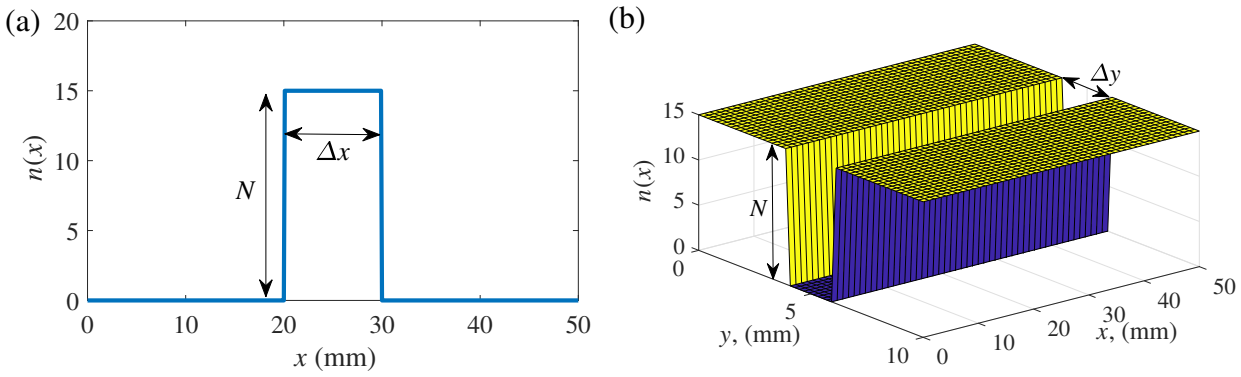

Figure 6.4: The number of fibroblasts as functions of space. a) is an example of C2 $N = 15$ and $\Delta x = 10$mm and b) is an example of C3 where $N = 15$ and $\Delta y = 2$mm.

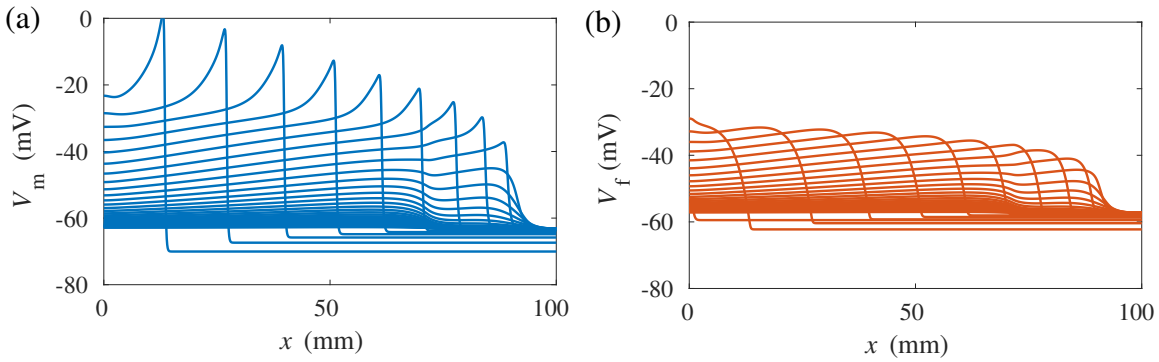

Figure 6.5: Myocyte and fibroblast APs propagating in space at intervals of 25ms, in the case of uniformly distributed fibroblasts where N=12.

6.3.2 Case 1: Uniform Fibroblast Distribution

In Section 6.3.1, three key cases of fibrotic regions are outlined. The first of which, uniform fibroblast distribution, is mathematically modelled with a 1D fibre where $n(x) = N$ is constant.

The basic effects of myocyte-fibroblast electrical coupling on conduction are best understood in the simple case C1 of uniform fibroblast distribution (6.1a). Figure 6.5 shows a numerical experiment that illustrates much of the observed behaviour in context. Here, a tissue model with $N = 12$ fibroblasts coupled to each myocyte is considered. Myocyte and fibroblast variables are set initially to the resting values of uncoupled cells as defined in [16] and [63], respectively. A stimulation by a current injection with a single impulse is performed without allowing the tissue to come to a rest state. The myocyte and fibroblast transmembrane potentials assume typical action potential profiles, as shown in Figure 6.5, note that the profiles are plotted at intervals of 25ms. As the signals propagate in the x-direction and in time, their peak values V_{m}^{ω} and V_{f}^{ω} decrease while the pre-front potentials V_{m}^{α} and V_{f}^{α} increase. The overall shapes of the action potentials change and most notably the steep profile of the myocyte potential, V_{m} is eroded and assumes a much more diffusive profile than initially. This coincides with a slowdown of conduction until eventually decay of the action potentials occurs.

Since conduction velocity and action potential features depend on the state of the tissue ahead of the front, this behaviour in these experiments can be explained by the process of relaxation of pre-front values of the myocyte and fibroblast potentials, gating variables, and ionic concentrations to their resting states. This relaxation occurs simultaneously with the propagation of the AP into the tissue. The resting state of the coupled myocyte-fibroblast system is different from the resting states of the uncoupled myocytes and fibroblast cells and Figure 6.1 shows the equilibrium values V_{m}^{α} and V_{f}^{α} of myocyte and fibroblast potentials and, as examples, also of the slow inactivation gating variable of the myocyte sodium current j^{α} and of the resting calcium concentration, $[\mathrm{Ca_i}]^{\alpha}$, all as functions of the number of coupled fibroblasts N. For each value of N, the resting values are computed by suppressing stimulation and leaving the tissues to relax for 1000 ms at which moment the equilibrium values are recorded. The pre-front potentials V_{m}^{α} and V_{f}^{α} as well as the $[\mathrm{Ca_i}]^{\alpha}$ increase monotonically while j^{α} decreases from their respective uncoupled values with the increase of the number of coupled fibroblasts N.

Figure 6.6 shows the dependences of other selected AP biomarkers commonly measured experimentally on the number of coupled fibroblasts N. The most significant result is the existence of a critical number of fibroblasts beyond which action potential propagation is inhibited and the tissue relaxes to equilibrium soon after stimulation. At the parameter values used in Figure 6.6 this critical number is $N_{\mathrm{crit}} = 10$. At values of N smaller than this critical value, normal action potentials are established and travel in the x-direction with constant wave speed, c, and a fixed shape. These can be characterised with the value of their peak potential, V^{ω}, APD_{30}, APD_{90}, and the normalised triangulation index,

$$\mathrm{AP}_{\mathrm{Tri}} = \frac{\mathrm{APD}_{90} - \mathrm{APD}_{30}}{\mathrm{APD}_{90}}. \tag{6.2}$$

Wave speed values, c, exhibit non-monotonic behaviour with a slight increase in the interval $N \in [0,4]$ and decrease for larger values of N until N_{crit} is reached as shown in Figure 6.6(b). This behaviour is similar to the "biphasic" behaviour reported by Miragoli et al. [59] in experiments and by [121] in simulations of a cell-attached model. This non-monotonicity was suggested to occur because wave speed first increases by the fibroblast bringing the membrane potential closer to the threshold for sodium current activation but then decreases as the increasing fibroblast density shift the cardiomyocyte membrane resting potential and sodium inactivation as discussed above. This will be subject to further theoretical modelling in Chapter 7. With the increase of the number of coupled fibroblasts N, both the peak potential values V^{ω} (Figure 6.6a)) and the values of APD_{30} (Figure 6.6d)) decrease, while the values of APD_{30} (Figure 6.6e)) somewhat increase, before collapse at $N_{\mathrm{crit}} = 10$, giving rise to increasingly triangular AP profile as measured by $\mathrm{APD}_{\mathrm{Tri}}$ (Figure 6.6f)). Another important quantity is the peak internal myocyte calcium concentration, $[\mathrm{Ca_i}]^{\omega}$ which is directly linked the magnitude of myocyte contraction, and is used to couple electrophysiological models to models of sarcomere mechanics

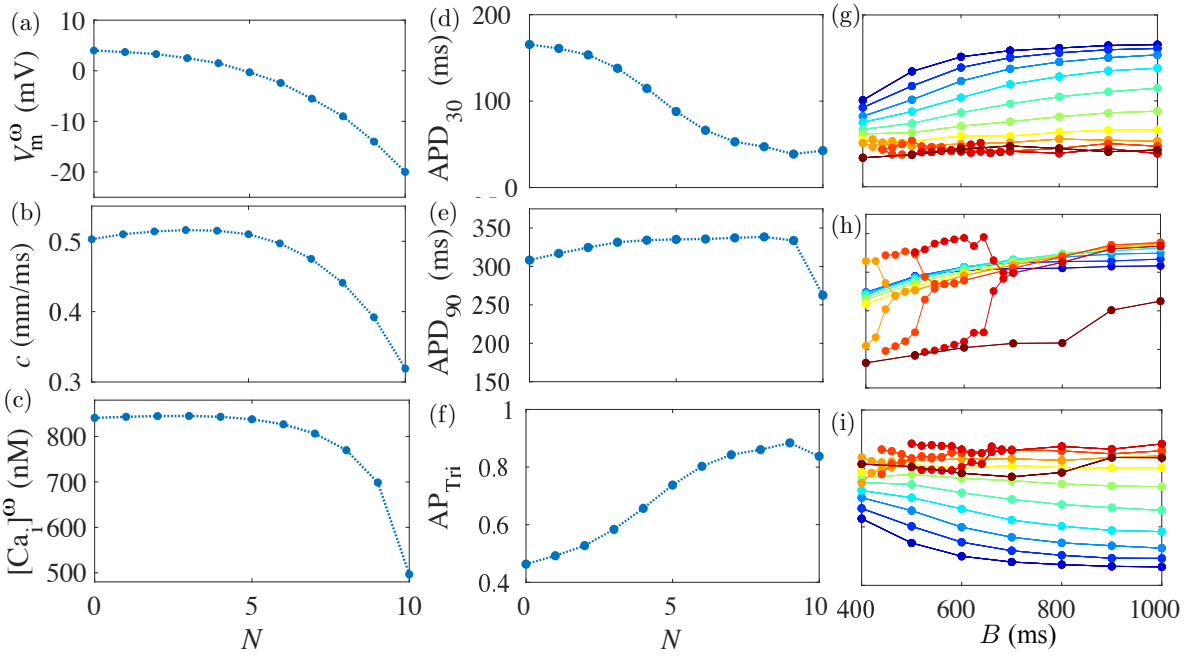

Figure 6.6: Change in a) the maximum myocyte potential, V^{ω}, against N b) the AP wave speed, c, against N c) the maximum internal myocyte calcium concentration against N, d) the myocyte APD_{30} against N e) the myocyte APD_{90} against N and f) the AP_{Tri} against N and g) the myocyte APD_{30} against B h) the myocyte APD_{90} against B and i) the AP_{Tri} against B.

[88]. The peak calcium concentration shown in Figure 6.6c) stays relatively constant until after $N = 6$, after which it decreases. Without coupling the EP model to a model of contraction, it is clear that coupling a high number of fibroblasts will affect muscle contraction significantly.

Both in electrophysiological experiments and in vivo tissue is usually paced continually. This is mimicked by investigating the effects that changing the basic cycle length, B, (BCL) has on the action potential profile and its propagation. Simulations were performed for $N < N_{crit}$ for a physiological range of BCLs ranging from 300ms (200bpm) to 1000ms (60bpm). To allow the stimulated APs to adjust to the BCL a tissue of length 20mm was simulated for 6000ms, again leaving the tissue to relax in the initial 1000ms before the first stimulation. As the BCL was increased both the APD_{30} shown in Figure 6.6g) and the APD_{90} shown in Figure 6.6h) increase. However, when the fibroblast count N reaches $N = 7,8,9$, alternans occur for shorter BCL. At $N = 10$ alternans do not appear, this is likely due to the value being too close to the threshold of excitation. The restitution curves end when the BCL becomes too short to successfully stimulate every AP. For the smaller values of N, the normalised triangulation index, AP_{Tri} shown in Figure 6.6i) increases weakly for small BCL, but for larger BCL the AP_{Tri} remains relatively constant. Action potential triangulation as an important pro-arrhythmic index

6.3.3 Case 2: Fibroblast Barrier

The second case, to be modelled is healthy tissue which is separated by a patch of increased fibrosis. This case is modelled as a 1D fibre where $n(x,y)$ is a step function, as described in

Section 6.3.1 (see Figure 6.4a). This case represents healthy myocardium characterised by small fibroblast density split in two by a fibrous region of high fibroblast density where N fibroblasts are attached to each myocyte.

A test was completed with direct numerical simulations of the full model in which a 1D fibre of length 50mm. Case 1 tells us that is $N \leq 10$ the AP will always propagate through this patch however if $N > 10$ the AP may decay away in this region. Thus, a range of N when $N > 10$ is tested and also with a range of widths of the fibrotic region, Δx. Again, like Case 1, the AP was stimulated after 1,000ms, allowing the fibrotic region to come to a new resting state.

It is expected that the action potential propagation in this case will depend on both the width Δx and the fibroblast count N – the two parameters needed to define this fibroblast distribution. This is illustrated in Figure 6.7 which shows three examples of action potentials propagating in the direction perpendicular to a fibroblast barrier. Panels (a) and (b) of Figure 6.7 show that when the number of fibroblasts is held constant ($N = 15$), but barrier width is increased, from Δx=5mm to Δx=10mm the AP propagation is blocked. Whereas, panels (a) and (c) of Figure 6.7 show that if the barrier width is held constant, $\Delta x = 5$mm but number of fibroblasts is increased from N=15 to N=18 propagation is also blocked. These examples suggest that there exist critical values of the fibroblast barrier distribution parameters N and Δx over which block occurs. The locus of these values forms a critical curve that serves as a threshold separating the outcomes of successful propagation and block in the $(N - \Delta x)$ parameter space and is shown in Figure6.8(a). The threshold curve plays a similar role and appears similar in shape to “strength-duration” curves, familiar from experimental electrophysiology, that serve to determine the threshold of electrical excitation as functions of the stimulus current amplitude and duration. Note that as the fibroblast count N approaches 10 from above, Δx increases asymptotically consistent with the behaviour of the uniform case C1 discussed in the preceding section.

The threshold behaviour described above is the essential feature of the fibroblast barrier case C2. Because the barrier is relatively thin its effect on the propagating action potential is only transient if it is not blocked. In the extensive healthy regions far from the fibroblast barrier action potential biomarkers behave in the same way as in the uniform case C1 described in relation to Figure 6.6. For instance, Figure 6.8b) shows the calcium concentration profile propagating across a fibroblast barrier with $N = 15$ and $\Delta x = 5$ mm. While in the barrier region the calcium concentration is significantly less than in the “healthy" region, it quickly recovers on the exit of this relatively narrow strip.

6.3.4 Case 3: Myocyte Strait

The final case (C3) is a strand of healthy tissue between regions of fibrotic tissue, which is referred to as a “myocyte strait”. To model this a 2D slab (50mm x 10mm) is simulated, $n(x,y)$ defines a narrow strip that has no coupled fibroblasts and elsewhere the number of coupled fibroblasts is greater than the maximum number of fibroblasts that allow propagation as defined

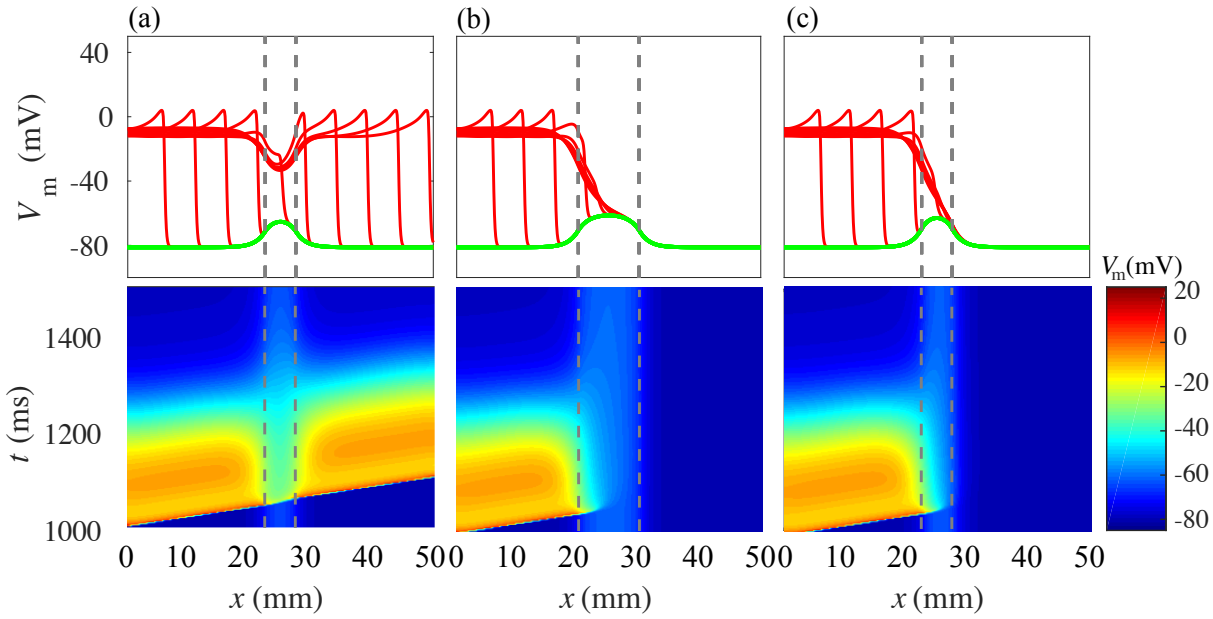

Figure 6.7: Examples of Case 2. The top row shows APs propagating across the patch at time intervals of 10 ms, the thick green line is the potential at the moment before stimulation. Column a) N=15 and Δx=5mm, column b) N=15 and Δx=10mm, and column c) N=18 with Δx=5mm. Thin grey broken vertical lines show the location and the width Δx of the fibroblast barrier and the green line is the potential at the moment before the stimulation.

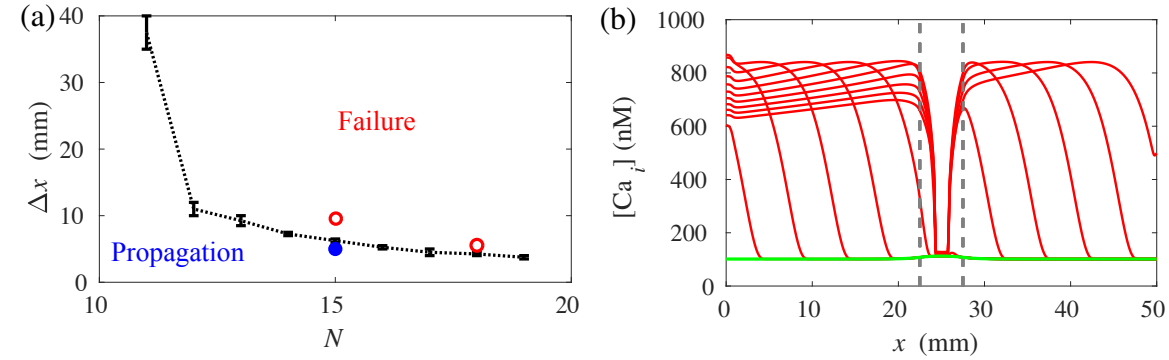

Figure 6.8: The threshold curve separating the outcomes of propagation and block of action potential in the $(N-\Delta x)$ plane in the case of fibroblast barrier distribution (6.1b). The error bars show the nearest pair of grid points where simulations were run in order to construct the curve with the curve taken at midpoints. The markers show the locations of the three examples illustrated in Figure 6.7 with full blue circles indicating successful propagation and empty red circles indicating block. (b) Cross-sections of calcium concentration transient $[Ca_i](x, y = Ly/2,$ at intervals of 10ms, from the moment of stimulation), $k = 0,1,2...$ in the case $N = 15$ and $\Delta x = 5$ mm plotted in style similar to the panels in the top row of Figure 6.7. The thin grey broken vertical lines show the location and the width Δx of the fibroblast barrier and the green line is the potential at the moment before the stimulation.

in Section 6.3.1 (see Figure 6.4b). In the simulations the first 5mm of the region (in the x-direction) has 0 coupled fibroblasts to allow the AP to establish before entering the strand and once again the tissue is stimulated after 1,000ms to allow an equilibrium state to form.

Similarly to the fibroblast barrier, a myocyte strait is determined by two free parameters – its

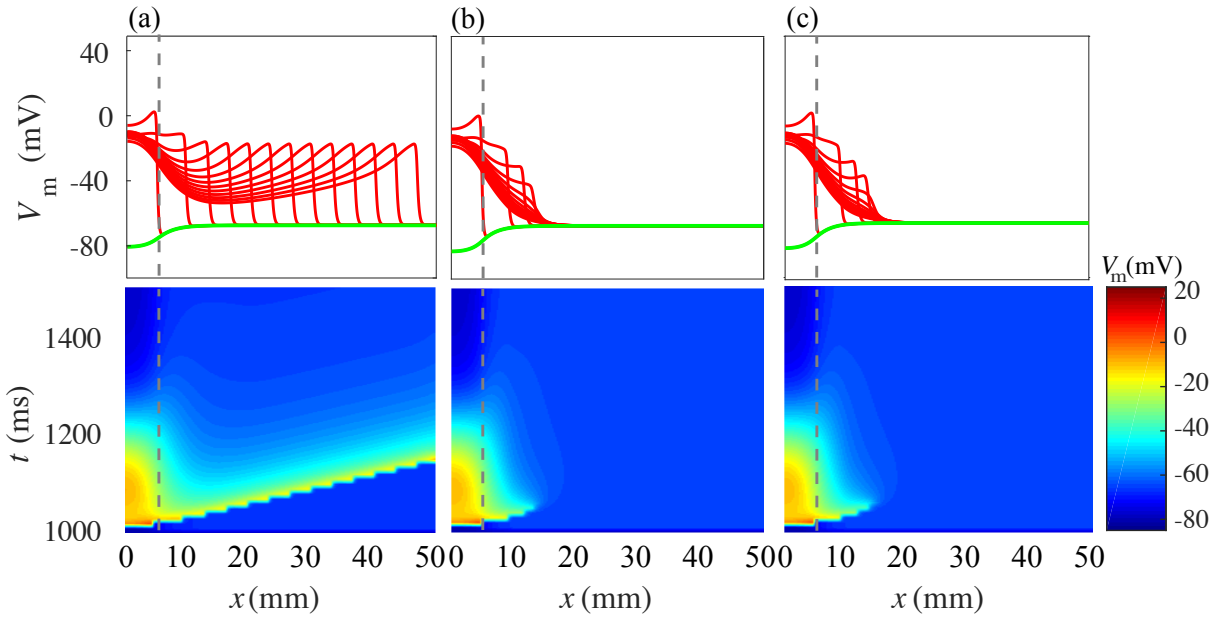

Figure 6.9: Three examples of APs in the case of a myocyte strait (C3), at intervals of 10ms. The top row shows APs propagating into the strand at time intervals of 10 ms, the thick green line is the potential initial conditions. The bottom rows show the potential in time and space. Column a) $N = 15$ and $\Delta y = 0.6$mm, Column b) $N = 15$ and $\Delta y = 0.4$mm, and Column c) $N = 18$ and $\Delta y = 0.6$mm. The thin grey broken vertical lines show the location and the width δx of the fibroblast barrier and the green line is the potential at the moment before the stimulation.

width Δy and the fibroblast count N in the adjacent fibrous regions, and similarly, it is expected that action potential propagation and failure will depend on both. Figure 6.9 shows three examples of action potentials propagating x-direction through myocyte straits. Panel (a) of Figure 6.9 shows an action potential propagating successfully through a strait of width Δy =0.6 mm with 15 fibroblasts coupled to each myocyte on either side of the strand. The corresponding propagation of the calcium transient in this case is shown in Figure 6.10(b). Propagation block occurs when strait width is reduced as illustrated in Figure 6.9(b) for Δy =0.4 mm and the same fibroblast count with $N = 15$ as in panel (a). Propagation block also occurs when the fibroblast count in the flanking fibrotic regions is increased as demonstrated in Figure 6.9(c) for a strand with Δy =0.6 mm, identical to that of panel (a) but with $N = 18$. The critical threshold curve separating the regions where successful propagation and block occur in the $(N - \Delta y)$ parameter space is shown in Figure 6.10(a). The threshold curve tends to $N = 10$ from above as Δy tends to 0 mm in agreement with the uniform case C1.

The simulations also show that if the AP can propagate through the strand it has a constant speed and shape. Although the wave speed and maximum shape both decrease as N increases. These results are shown in Figure 6.11.

As discussed in Section 5.6.2, to avoid numerical instabilities in the cases near the propagation threshold, the mesh discretization size was reduced from 0.1 mm to 0.05 mm in select few cases, in particular for larger values of N = 18, 19, 20. This increase of resolution is also

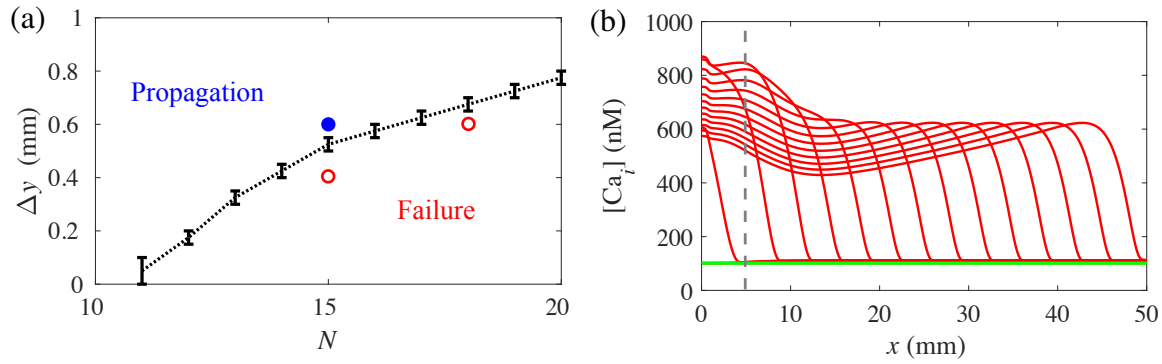

Figure 6.10: The threshold curve separating the outcomes of propagation and block of action potential in the $(N-\Delta x)$ plane in the case of a myocyte strait (C3). The error bars show the nearest pair of grid points where simulations were run in order to construct the curve with the curve taken at midpoints. The markers show the locations of the three examples illustrated in Figure 6.9 with full blue circles indicating successful propagation and empty red circles indicating block. (b) Cross-sections of calcium concentration transient $[\mathrm{Ca}_i](x, y = Ly/2$, at intervals of 10ms, from the moment of stimulation), $k = 0,1,2...$ in the case $N = 15$ and $\Delta y = 0.6$ mm plotted in style similar to the panels in the top row of Figure 6.7. The thin grey broken vertical line shows the location of the fibroblast region and the green line is the potential at the moment before the stimulation.

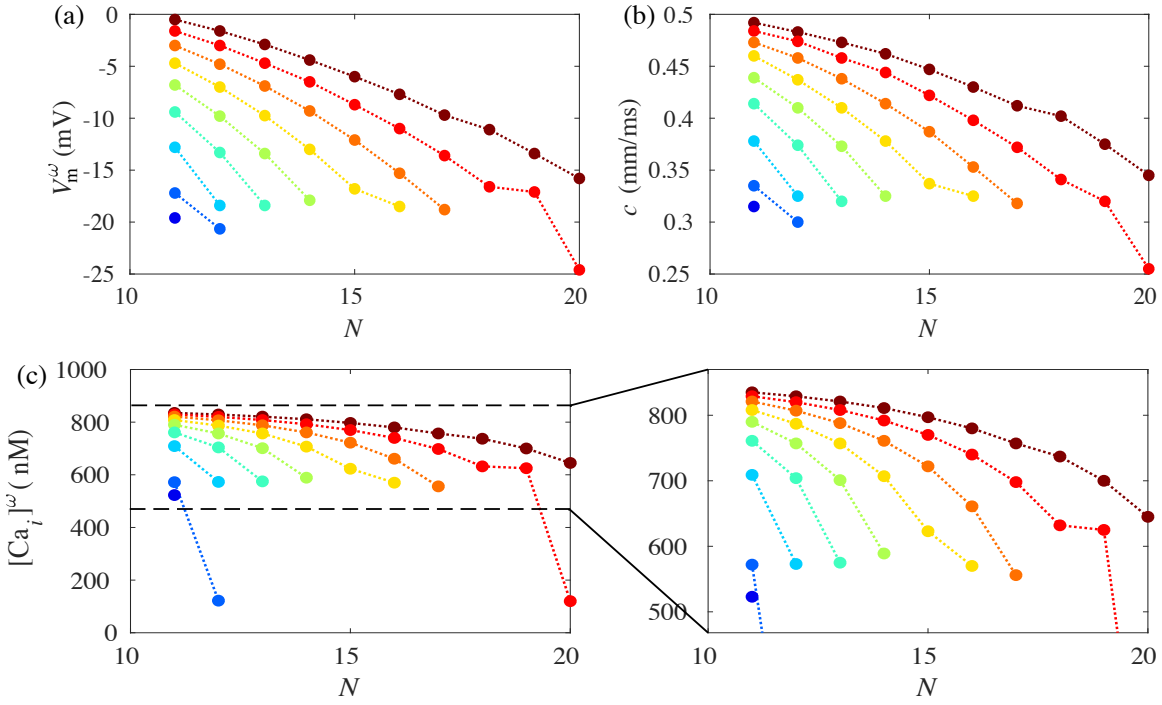

Figure 6.11: The change in a) the maximum potential, b) the wave speed, c and c) the maximum calcium concentration in the strand, for a range of N in the fibrotic regions and Δy. The width, Δy, increases from 0.1mm to 0.9mm in increments of 0.1mm in the direction of the arrow.

responsible for an insignificant change in the slope of the curves corresponding to $\Delta y = 0.8$mm and 0.9mm in Figure 6.11.

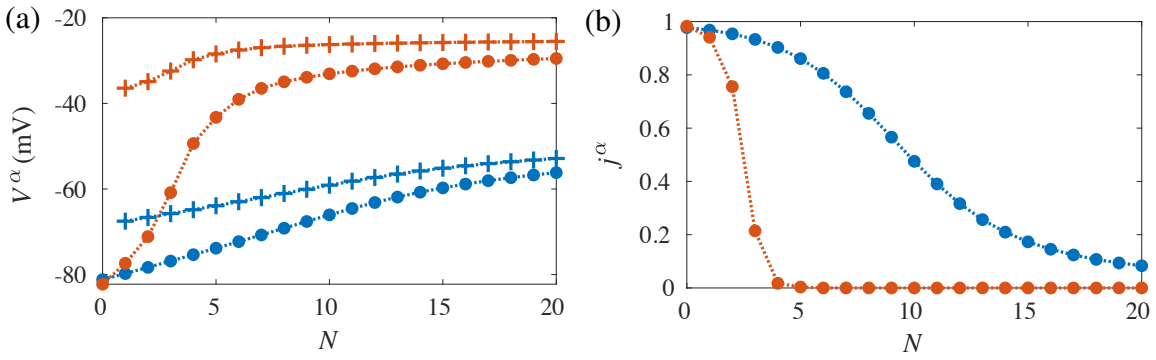

Figure 6.12: a) The resting potentials from the myocyte-myofibroblast system (in blue) and myocyte-fibroblast (in orange), with of myocytes (•'s) coupled with fibroblasts (+'s), where blue denotes the myocyte-fibroblast model and orange denotes the myocyte-myofibroblast. b) Resting gating variable j with coupled fibroblasts (blue) and with coupled myofibroblasts (orange). The black +'s denote the minimum value of j from the reduced model for the myocyte-myofibroblast model.

6.4 Comparison of Fibroblasts and Myofibroblasts

As discussed in Section 2.2, fibroblasts have the ability to differentiate themselves into myofibroblasts, becoming larger and containing smooth muscle fibres. These changes in their physiology has effects on their electrophysiology. Work by Nguyen et al. [69] identifies that myofibroblasts have a capacitance of, C_m = 50.0pF, and an uncoupled resting potential of -25mV. To achieve this higher resting potential, the inward rectifying current, I_{K1}, is modified, by decreasing the channel conductance, G_{K1}, from 0.03ms^{-1} to 0.0075ms^{-1}. Changing these values has a significant effect on the system. Figure 6.12 shows the change in the resting values of the myocyte and myofibroblast potentials and the gating variable j, alongside the equivalent values from the myocyte-fibroblast system, for a range of N cells per myocyte. When myofibroblasts are coupled to myocytes the resting potentials of both cell types increases much quicker and plateaus at a lower value of N. Similarly, the equilibrium value j decreases much sooner than the equivalent in the fibroblast-myocyte system. With the myocyte-myofibroblast system the same fundamental cases C1, C2 and C3 (outlined in Section 6.3.1) can be performed. The results of these tests give the same qualitative results as with the myocyte-fibroblast model. Although, since the resting potential of the myofibroblast is much higher than the regular fibroblast, the width needed to block propagation is much thinner in Case 2 and similarly in Case 3 the width that allows propagation along the isthmus is wider. The results of the tests of cases 2 and 3 can be seen in Figure 6.14

6.5 Discussion of Myocyte-Fibroblast Coupling

A mathematical model of fibrous atrial tissue has been formulated in terms of a set of cardiac monodomain equations including a myocyte-fibroblast coupling current. Following the works

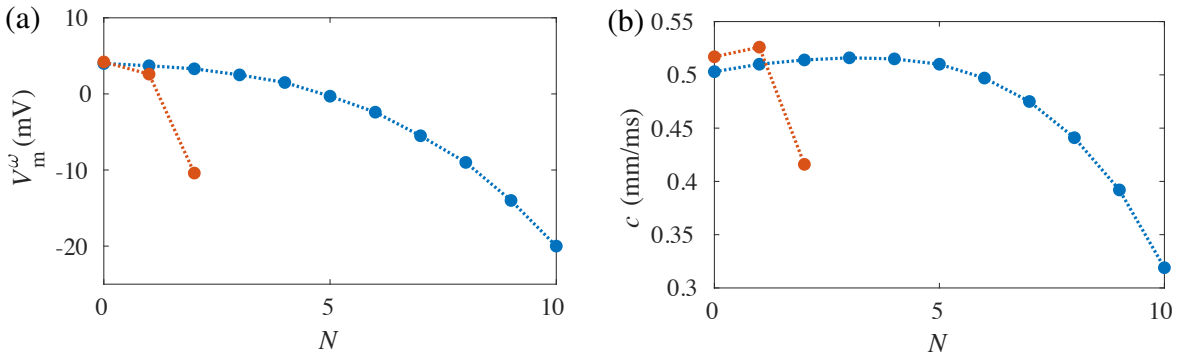

Figure 6.13: a) The resting potentials from the myocyte-myofibroblast system (in blue) and myocyte-fibroblast (in orange), with of myocytes (•'s) coupled with fibroblasts (+'s), where blue denotes the myocyte-fibroblast model and orange denotes the myocyte-myofibroblast. b) Resting gating variable j with coupled fibroblasts (blue) and with coupled myofibroblasts (orange). The black $+$'s denote the minimum value of j from the reduced model for the myocyte-myofibroblast model.

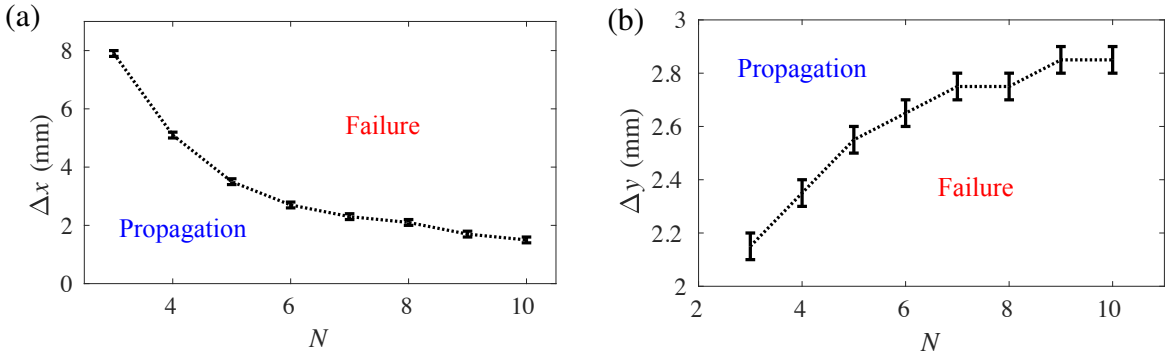

Figure 6.14: a) The threshold curve separating the outcomes of propagation and block of action potential in the $(N-\Delta x)$ plane in the case of fibroblast barrier distribution (6.1b). b) The threshold curve separating the outcomes of propagation and block of action potential in the $(N-\Delta y)$ plane in the case of fibroblast barrier distribution (6.1c). The error bars show the nearest pair of grid points where simulations were run in order to construct the curve with the curve taken at midpoints.

of [122] and [79] we adopt an "attachment" approach to couple the human atrial myocyte model of [16] to the mammalian fibroblast model of [63]. A key advantage of the "attachment" approach is that it can be easily employed within a homogenised continuum model such as the monodomain equations and a variety of fibroblast distributions can be prescribed simply and acutely. The alternative "insertion" approach requires that the model is defined on a discrete grid and does not lend itself easily to asymptotic analysis of the type report here. The atrial model of [16] is chosen as partial asymptotic results (see below) were readily available in earlier work by Simitev and Biktashev [101] for this specific kinetics and because the numerical code was already validated in this case against the benchmark of [71]. For direct numerical simulations of the monodomain equations the Strang operator splitting method is used, as discussed in Section 5.6.2.

Using this setup three idealised fibroblast distributions are investigated: uniform distribution, fibrosis barrier distribution and myocyte strait distribution. These are based on histology of fibrotic cardiac tissue, and it is hypothesised that these are the constituent blocks of realistic fibroblast distributions. Essential action potential biomarkers that are typically measured in electrophysiological myocardial tissue experiments including conduction velocity, peak potential, action potential duration, and triangulation index are estimated from direct numerical simulations for all idealised distributions. Failure of action potential propagation is found to occur at certain critical values of the parameters that define each of the idealised fibroblast distributions and these critical values are accurately determined. In the case of uniform fibroblast distribution it is found that electrical excitation fails to propagate when 10 or more fibroblasts are coupled to each myocyte at the standard parameter values of the simulations. As fibroblast count increases from zero, peak potential decreases while conduction velocity slightly increases for mild fibrosis and then as the degree of fibrosis becomes more severe block occurs. The values of APD_{90} increase as the fibroblast count increases until close to the propagation threshold when APD_{90} decreases rapidly. Similarly, the calcium concentration stays relatively constant as N increases from 0, until $N = 8$, after which it also falls off rapidly. In the case of fibroblast barrier where “healthy" tissue is separated by a region of fibrosis the direct numerical simulations show that propagation block is determined by both the width of the fibrosis barrier and the count of fibroblasts coupled to each myocyte within it. For examples, the more severe the fibrosis within the region the thinner it must be to allow successful AP propagation. Then threshold curve of fibroblast count versus width that splits propagation from failure is determined. This curve is akin to strength-duration curves that are used elsewhere to determine the amplitude and the duration of a stimulus current that is needed to trigger excitation. Unlike in the first and third fibroblast distribution cases in this second case, it the AP is not appropriate to measure biomarkers as the fibrotic region not big enough. In the case of myocyte strait where channel of “healthy" tissue between two regions of fibrosis it is demonstrated that successful AP depends on both the width of the strait and the fibroblast count in the adjacent regions. For instance, the more severe the fibrosis of the surrounding region is, the wider the strand must be to admit the pulse across. Similarly, to the second case the threshold curve of fibroblast count versus strait width that splits propagation from failure is constructed. When the strait width is held constant, as the fibroblast density in the adjacent regions increases the wave speed, peak potential and the peak calcium concentration all decrease.

The same fundamental patterns of fibroblast distribution were applied to the case with myocytes coupled with myofibroblasts, which have an increased capacitance and uncoupled resting potential. The results show the same qualitative results, although there is a large difference in the quantitative results. Firstly the uniform distribution showed that only 3 myofibroblasts are needed to block propagation, and then when cases C2 and C3 are completed for $N \geq 3$, a much thinner barrier is required to stop the AP from propagating across the barrier, and a much wider

myocyte strait was required to block the AP.

This work does not consider the effect of collagen formed in the fibrotic scar. This has been excluded as collagen is not electrically active and thus its main contribution is to alter the value of the effective potential diffusivity and this can be accounted for by simply rescaling the spatial variables in the governing equations. While this is straightforward, in theory, to account for realistic fibrosis distributions the collagen effect and the effects of tissue anisotropy are difficult to separate from the biomarker changes that are reported and so it should be included in simulations. This work also shows that for a large number coupled fibroblasts, the maximum internal myocyte calcium concentration is significantly less than in the fibroblast-free case, and, as discussed in Chapter 3, it is the calcium profile that triggers the myocyte contraction. Also, along with reduced calcium levels, the fibroblasts also increase the collagen density which will increase the passive forces in the system and block contraction further. So, the inclusion of fibroblasts is important when modelling cardiac muscle contraction.

Chapter 7

Asymptotic Theory of Action Potential Propagation in Fast and Slow Subsystems: Reducing the Model

In this Chapter the arguments used to reduce the system to a model of the resting potential and a model of the AP wavefront are outlined. In particular the asymptotic theory of the papers [6, 101, 103] is extended to the case of uniform fibroblast distribution (C1). The theory captures qualitatively the behaviour of action potential biomarkers reported above and explains the occurrence of propagation block with increasing fibroblast count N. This asymptotic theory considers the fast subsystem of the model. The slow subsystem of the model can also be exploited to find analytical equations of the resting myocyte and fibroblast potentials, exploring work in [122].

Equations (5.30) contain both fast and slow components. The initial upstroke of the action potential is determined by the sodium current and is said to be “fast", and is dependent on the fast gating variables m and h. The other fast variables are the gating variables u_a, o_a and d. However, if it assumed that the system has stopped changing, i.e. $\frac{\partial V_{\mathrm{m}}}{\partial t} = \frac{\partial V_{\mathrm{f}}}{\partial t} = 0$, then one can explore how the tissue will act if allowed to rest for a long period of time, thus this is the “slow" subsystem.

7.1 The Slow Subsystem: Analytical Resting Potential

As previously stated, the slow subsystem considers the tissue as it comes to a rest, once all of the mechanics of the myocytes and fibroblasts have ended. This means that the active part of the model can be considered by the simpler passive form, as argued by Weiss et al. [122]. They argue that when a cell approaches its rest state the ionic currents can be assumed to be negligible and thus removed and replaced with passive terms. By finding the Taylor expansion of I_Σ about

the point E_{m}, the passive form of the ion currents is found,

$$I_{\Sigma}(V_{\mathrm{m}}) = I_{\Sigma}(E_{\mathrm{m}}) + \left.\frac{\partial I_{\Sigma}}{\partial V_{\mathrm{m}}}\right|_{E_{\mathrm{m}}} (V_{\mathrm{m}} - E_{\mathrm{m}}) + \ldots = G_{\mathrm{m}}(V_{\mathrm{m}} - E_{\mathrm{m}}), \tag{7.1}$$

since $I_{\Sigma}(E_{\mathrm{m}}) = 0$ and $\left.\frac{\partial I_{\Sigma}}{\partial V_{\mathrm{m}}}\right|_{E_{\mathrm{m}}} = G_{\mathrm{m}}$. Similarly, the Taylor expansion for I_{f} at E_{f} can be found and thus in the vicinity of the resting potential of the uncoupled myocyte, the following equations for V_{f} and V_{m}, are found,

$$C_{\mathrm{m}}\frac{dV_{\mathrm{m}}}{dt} = -G_{\mathrm{m}}(V_{\mathrm{m}} - E_{\mathrm{m}}) + NG_{\mathrm{gap}}(V_{\mathrm{f}} - V_{\mathrm{m}}), \tag{7.2}$$

$$C_{\mathrm{f}}\frac{dV_{\mathrm{f}}}{dt} = -G_{\mathrm{f}}(V_{\mathrm{f}} - E_{\mathrm{f}}) + G_{\mathrm{gap}}(V_{\mathrm{m}} - V_{\mathrm{f}}), \tag{7.3}$$

where E_{m} and E_{f} are the resting potentials of the uncoupled myocytes and fibroblasts, set to be -81mV and -46mV, respectively. This also introduced the new unknown parameters, the membrane conductances of the myocytes and the fibroblasts are G_{m} and G_{f}, respectively. These conductances are unknown. It should be noted that as the case of uniform fibroblast distribution is being considered and so the function of the number of coupled fibroblasts per myocyte is set to be constant, $n(\mathbf{x}) = N$.

Using these simpler passive forms of the ionic currents and setting potentials to be constant (i.e. when $\frac{dV_{\mathrm{m}}}{dt} = \frac{dV_{\mathrm{f}}}{dt} = 0$), the equations can be solved to find the equilibrium values of the potentials,

$$V_{\mathrm{m}}^{\alpha}(N) = E_{\mathrm{m}} + \frac{N}{G_{\mathrm{m}}}\frac{(E_{\mathrm{f}} - E_{\mathrm{m}})}{\frac{1}{G_{\mathrm{gap}}} + \frac{1}{G_{\mathrm{f}}} + \frac{N}{G_{\mathrm{m}}}}, \tag{7.4}$$

$$V_{\mathrm{f}}^{\alpha}(N) = E_{\mathrm{f}} - \frac{1}{G_{\mathrm{f}}}\frac{(E_{\mathrm{f}} - E_{\mathrm{m}})}{\frac{1}{G_{\mathrm{gap}}} + \frac{1}{G_{\mathrm{f}}} + \frac{N}{G_{\mathrm{m}}}}, \tag{7.5}$$

where V_{m}^{α} and V_{f}^{α} are the myocyte and fibroblast potentials at equilibrium. These solutions show that $V_{\alpha\mathrm{m}}$ and $V_{\alpha\mathrm{f}}$ are both dependent on N, as expected. They also show that if no fibroblasts are coupled ($N = 0$), the resting potential is, as defined, $V_{\mathrm{m}}^{\alpha} = E_{\mathrm{m}}$, and, if N tends to infinity, both transmembrane potentials tend to E_{f}. Similarly, if $G_{\mathrm{gap}} = 0$, as expected, $V_{\mathrm{mr}} = E_{\mathrm{m}}$ and $V_{\mathrm{f}}^{\alpha} = E_{\mathrm{f}}$, and when G_{gap} tends to infinity, both V_{m}^{α} and V_{f}^{α} tend to the same constant, a trade-off between the uncoupled resting potentials, E_{m} and E_{f}, the transmembrane conductances G_{m} and G_{f}, and the number of coupled fibroblasts, N,

$$\lim_{G_{\mathrm{gap}}\to\infty}(V_{\mathrm{m}}^{\alpha}) = \lim_{G_{\mathrm{gap}}\to\infty}(V_{\mathrm{f}}^{\alpha}) = \frac{G_{\mathrm{m}}E_{\mathrm{m}} + NG_{\mathrm{f}}E_{\mathrm{f}}}{G_{\mathrm{m}} + NG_{\mathrm{f}}}. \tag{7.6}$$

As mentioned, the conductances of the membranes, G_{m} and G_{f}, are unknown. Although, by considering the values of the resting potentials recorded in the direct numerical simulations

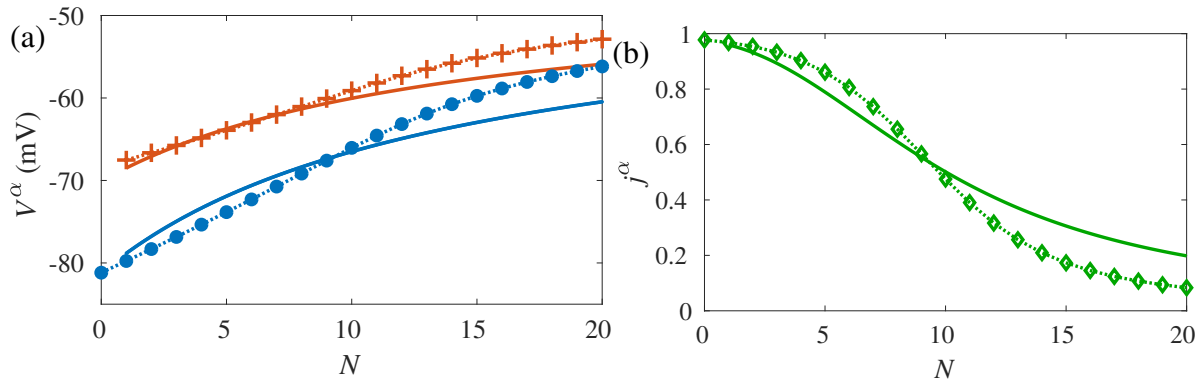

Figure 7.1: Selected components of the equilibrium solution to the slow-time system (7.4). (a) The resting (pre-front) myocyte potential V_{m}^{α} (solid blue curve) and fibroblast potential V_{f}^{α} (solid red curve) as functions of the fibroblast count N evaluated from (7.4). Dotted curves with blue circle markers and with red plus-sign markers show values of V_{m}^{α} and V_{f}^{α}, respectively, measured from direct numerical simulations of (5.30) as discussed in Section 6.3.2. (b) The resting (pre-front) value j^{α} of the j-gate as a function of the fibroblast count N evaluated analytically (solid green curve) and from direct numerical simulations (dotted curve with diamond markers). With $G_{\mathrm{f}} = 0.23$ nS and $G_{\mathrm{m}} = 2.2$ nS.

(DNS), as seen in Figure 6.1, suitable values for these parameters can be chosen. Figure 7.1a shows the analytical equations of the resting potentials fitted against the resting potentials from the DNS, with $G_{\mathrm{f}} = 0.23$ nS and $G_{\mathrm{m}} = 2.2$ nS, showing a good qualitative and quantitative fit. Note, $N = 0$ is excluded as there is no value for V_{f}^{α} when $N = 0$.

Using this analytical result from the passive model, the change of resting values of the other variables can be found. Notably, the gating variable of j,

$$\frac{dj}{dt} = \alpha_j - j(\alpha_j + \beta_j), \quad \text{thus} \quad j_\alpha = \frac{\alpha_j}{\alpha_j + \beta_j}, \tag{7.7}$$

where j_α is the resting value of the gating variable j. The terms α_j and β_j are dependent on V_m^α and are defined in [101]. For small N, j_α is approximately 1. As N increases, j_α decreases and approaches 0. The analytical solution of j_α is plotted, against the simulated resting values of j, in Figure 7.1b).

7.2 The Fast Subsystem

The actions potentials which are excited by periodic stimuli and are propagating with a fixed shape and speed are investigated by the travelling wave coordinates, $z = \tilde{x} + ct$, are introduced, where $\tilde{x} = x\sqrt{C_{\mathrm{m}}\chi/\sigma_{11}}$ is a rescaled x-coordinate. Thus, the system becomes a periodic bound-

ary value problem

$$c\frac{d}{dz}V_{\mathrm{m}} = -\frac{1}{C_{\mathrm{m}}}\Big(I_{\mathrm{m}}(V_{\mathrm{m}},\mathbf{u}) + N\,G_{\mathrm{gap}}(V_{\mathrm{m}}-V_{\mathrm{f}})\Big) + \frac{d^2}{dz^2}V_{\mathrm{m}}, \tag{7.8a}$$

$$c\frac{d}{dz}V_{\mathrm{f}} = -\frac{1}{C_{\mathrm{f}}}\Big(I_{\mathrm{f}}(V_{\mathrm{f}},\mathbf{u}) + G_{\mathrm{gap}}(V_{\mathrm{f}}-V_{\mathrm{m}})\Big), \tag{7.8b}$$

$$c\frac{d}{dz}\mathbf{u} = \mathbf{F}(\mathbf{u},V_{\mathrm{m}},V_{\mathrm{f}}), \tag{7.8c}$$

$$V_{\mathrm{m}}(0) = V_{\mathrm{m}}(cB),\ \frac{d}{dz}V_{\mathrm{m}}(0) = \frac{d}{dz}V_{\mathrm{m}}(cB),\ V_{\mathrm{m}}(z_0) = V_{\mathrm{m}}^b,\ V_{\mathrm{f}}(0) = V_{\mathrm{f}}(cB),\ \mathbf{u}(0) = \mathbf{u}(cB), \tag{7.8d}$$

where $\mathbf{u}$ is a vector of all gating variables controlling the conductances of myocyte and fibroblast ionic channels and the various intra- and extra-cellular concentrations of ions, with the functions that define their dynamics, denoted by $\mathbf{F}$, as defined in [16] and [63]. A phase (or pinning) condition is needed to eliminate the translational invariance of the system and arises to replace the initial value condition of the system. Thus, for the phase condition, $V_{\mathrm{m}}(z_0) = V_{\mathrm{m}}^b$, $z_0 \in [0, cB]$ and V_{m}^b is an arbitrary constant within range of V_{m}, e.g. $V_{\mathrm{m}}^b = 0$ mV.

7.2.1 Asymptotic embedding

In order to analyse this boundary value problem, formulated above, an asymptotic embedding procedure is used, which introduces into the equations the small parameter $\varepsilon > 0$ [6]. With this embedding the system of equations is unchanged when $\varepsilon = 1$, whereas if ε tends to zero (from above) useful asymptotic simplifications are obtained . There are infinitely many ways to embed a small parameter ε and their merits are assessed on firstly, the basis of the usefulness of the asymptotic simplifications and secondly, on the quality of approximation to the solutions of the original problem.

The asymptotic embedding of Equations (7.8) used in this work is based on work by Simitev et al. [101], on the relative speed of the dynamical variables in the atrial model of [16]. For a system of M differential equations $\mathrm{d}w_l/\mathrm{d}t = F_l(w_1,\ldots w_M)$, $l = 1,\ldots M$ the relative speeds of dynamical variables w_l can be formally measured by their time-scaling functions defined as $tau_l(w_1,\ldots) \equiv |\mathrm{d}F_l/\mathrm{d}w_l|^{-1}$, $l = 1\ldots M$.

Comparing relevant time-scaling functions, our earlier work established that the myocyte potential V_{m} and the gating variables m and h are "fast variables", i.e. they change significantly during the upstroke of a typical action potential. While considering the fast system, all other variables are said to be"slow" as they only change weakly during the fast period. However, an unusual feature is that V_{m} is both fast and slow, and is only considered fast due to its dependence on the sodium current, this is said to be a non-Tikhonov feature [115]. Whereas, the sodium current is only large in the upstroke, due to the near perfect switch behaviour of gates m and h which are almost fully closed outside the upstroke. These observations lead to using the

following asymptotic embedding of equations (7.8)

$$c\frac{d}{dz}V_{\mathrm{m}} = -\frac{1}{C_{\mathrm{m}}}\left(\frac{1}{\varepsilon}g_{\mathrm{Na}}(V_{\mathrm{Na}}-V_{\mathrm{m}})jhm^3 + I_{\Sigma}(V_{\mathrm{m}},j,\mathbf{u}_{\mathrm{m}}) + N\,G_{\mathrm{gap}}(V_{\mathrm{m}}-V_{\mathrm{f}})\right) + \varepsilon\frac{d^2}{dz^2}V_{\mathrm{m}}, \tag{7.9a}$$

$$c\frac{d}{dz}V_{\mathrm{f}} = -\frac{1}{C_{\mathrm{f}}}\left(I_{\mathrm{f}}(V_{\mathrm{f}},\mathbf{u}_{\mathrm{f}}) + G_{\mathrm{gap}}(V_{\mathrm{f}}-V_{\mathrm{m}})\right), \tag{7.9b}$$

$$c\frac{d}{dz}m = \frac{\bar{m}(V_{\mathrm{m}},\varepsilon)-m}{\varepsilon\tau_m(V_{\mathrm{m}})}, \quad \bar{m}(V_{\mathrm{m}},0) = H(V_{\mathrm{m}}-E_m), \tag{7.9c}$$

$$c\frac{d}{dz}h = \frac{\bar{h}(V_{\mathrm{m}},\varepsilon)-h}{\varepsilon\tau_h(V_{\mathrm{m}})}, \quad \bar{h}(V_{\mathrm{m}},0) = H(E_h-V_{\mathrm{m}}), \tag{7.9d}$$

$$c\frac{d}{dz}j = \frac{\bar{j}(V_{\mathrm{m}})-j}{\tau_j(V_{\mathrm{m}})}, \tag{7.9e}$$

$$c\frac{d}{dz}\begin{bmatrix}\mathbf{u}_{\mathrm{m}}\\ \mathbf{u}_{\mathrm{f}}\end{bmatrix} = \begin{bmatrix}\mathbf{T}_{\mathrm{m}}(V_{\mathrm{m}}) & 0\\ 0 & \mathbf{T}_{\mathrm{f}}(V_{\mathrm{f}})\end{bmatrix}\left(\begin{bmatrix}\overline{\mathbf{u}_{\mathrm{m}}}(V_{\mathrm{m}})\\ \overline{\mathbf{u}_{\mathrm{f}}}(V_{\mathrm{f}})\end{bmatrix} - \begin{bmatrix}\mathbf{u}_{\mathrm{m}}\\ \mathbf{u}_{\mathrm{f}}\end{bmatrix}\right). \tag{7.9f}$$

The current I_Σ is the sum of all slow currents and $\mathbf{u}_{\mathrm{m}}$ and $\mathbf{u}_{\mathrm{f}}$ are vectors composed of the remaining slow gating variables (in addition to j which is also slow) with myocyte and fibroblast kinetics, respectively. The functions τ_w and $\bar{w}$ are time-scaling functions and quasi-stationary values of gating variables j, m, and h, respectively. For the remaining slow gates these time scaling functions are arranged in diagonal matrices $\mathbf{T}_{\mathrm{m}}$ and $\mathbf{T}_{\mathrm{f}}$ with indices denoting myocyte and fibroblast function and $\overline{\mathbf{u}_{\mathrm{m}}}$ and $\overline{\mathbf{u}_{\mathrm{f}}}$ are quasi-stationary values. The explicit forms of these expressions are specified in [16, 63]. To account for the perfect switch behaviour of m and h, the functions $\bar{m}(V_{\mathrm{m}},\varepsilon)$ and $\bar{h}(V_{\mathrm{m}},\varepsilon)$ are "embedded", i.e. they are ε-dependent versions of $\bar{m}(V_{\mathrm{m}})$ and $\bar{h}(V_{\mathrm{m}})$ such that $\bar{m}(V_{\mathrm{m}};1) = \bar{m}(V_{\mathrm{m}})$ and $\bar{h}(V_{\mathrm{m}};1) = \bar{h}(V_{\mathrm{m}})$ on one hand and $\bar{m}(V_{\mathrm{m}},0) = H(V_{\mathrm{m}}-E_m)$ and $\bar{h}(V_{\mathrm{m}},0) = H(E_h-V_{\mathrm{m}})$ on the other hand, with $E_m = -32.7\,\mathrm{mV}$ and $E_h = -66.66\,\mathrm{mV}$ so that $\bar{m}(E_m) = 1/2$ and $\bar{h}(E_h) = 1/2$. Note the subtle difference between the m and m subscripts, with the italicised m referring to the gating variable m and the regular m referring to the myocyte.

7.2.2 Asymptotic reduction

Now the system has been embedded and converted with the travelling wave coordinate the fast subsystem cane be found. Rescaling $Z = z/\varepsilon$, taking the limit $\varepsilon \to 0^+$ and neglecting decoupled equations, the fast-time subsystem is obtained,

$$c\frac{d}{dZ}V_{\mathrm{m}} = -\frac{g_{\mathrm{Na}}j^{\alpha}}{C_{\mathrm{m}}}(V_{\mathrm{Na}} - V_{\mathrm{m}})hm^3 + \frac{d^2}{dZ^2}V_{\mathrm{m}}, \tag{7.10a}$$

$$c\frac{d}{dZ}m = \frac{H(V_{\mathrm{m}} - E_m) - m}{\tau_m(V_{\mathrm{m}})}, \tag{7.10b}$$

$$c\frac{d}{dZ}h = \frac{H(E_h - V_{\mathrm{m}}) - h}{\tau_h(V_{\mathrm{m}})}, \tag{7.10c}$$

$$V_{\mathrm{m}}(-\infty) = V_{\mathrm{m}}^{\alpha},\ \frac{d}{dZ}V_{\mathrm{m}}(\infty) = 0,\ V_{\mathrm{m}}(\infty) = V_{\mathrm{m}}^{\omega},\ V_{\mathrm{m}}(0) = E_h,\ m(-\infty) = 0,\ h(-\infty) = 1. \tag{7.10d}$$

To avoid ambiguity, the pinning condition explicitly at $Z = 0$ have been specified in (7.10d) and the range $Z \in (-\infty, \infty)$ has been taken. We have also introduced the post-front potential, V_{m}^{ω} as a new parameter and introduced a condition to constrain it, this post-front potential is equivalent to the maximum potential. Note that fibroblast kinetics have been decoupled and do not explicitly affect this fast subsystem making this very similar to the problem considered in [101].

7.2.3 Solution to the Fast subsystem

For fixed myocyte and fibroblast parameter values, the fast subsystem (7.10) has differential equations of cumulative order four and contains four free parameters (c, V_{m}^{α}, V_{m}^{ω}, j^{α}), and is constrained by five boundary conditions and one pinning condition. Therefore, the fast subsystem is expected to have a two-parameter family of solutions, meaning that two of the free parameters can be chosen arbitrarily and all components of the solution will be functions of these two. For comparison with the direct numerical simulations shown in Figure 6.6, the pre-front values of the myocyte potential V_{m}^{α} and of the slow inactivation gating variable of the myocyte sodium current j^{α} are chosen as independent parameters. It is through the choice of the myocyte pre-front voltage that the system becomes implicitly dependent on the fibroblast kinetics, since V_{m}^{α} is equivalent to the resiting potential, which in turn is dependent on the number of fibroblasts coupled per myocyte, as seen in Figure 6.1. The recorded rest potentials, which were then used to define V_{m}^{α}, can be seen in Table 7.1.

In Figure 7.2, the post-front myocyte potential and the wave speed are shown as functions of the latter two, $V_{\mathrm{m}}^{\omega} = V_{\mathrm{m}}^{\omega}(V_{\mathrm{m}}^{\alpha}, j^{\alpha})$, and $c = c(V_{\mathrm{m}}^{\alpha}, j^{\alpha})$, respectively.

The solutions are computed using the numerical method of [101] where a problem identical to (7.10), although they also explore a curvature effect term which is not relevant to this work. The numerical methods take into account that the fast subsystem is posed on an infinite interval and that its right-hand sides are piece-wise differentiable. They use boundary-value problem solver D02RAF of the Numerical Algorithms Group numerical library, which employs a finite-difference discretisation coupled to a deferred correction technique and Newton iteration [74]. Figure 7.2 shows that solutions of the fast-time problem exist only within a certain region of the $(V_{\mathrm{m}}^{\alpha} - j^{\alpha})$-plane above a critical curve $j_{\mathrm{crit}}^{\alpha}(V_{\mathrm{m}}^{\alpha})$. In particular, at every point within this region

n	V_α (mV)	V_ω (mV)	j_{rest}	j_{min}	Simulated c	Analytical c	
						Unstable	Stable
0	-81.18	2.430	0.978	0.325	0.0505	0.286	1.324
1	-79.74	2.559	0.968	0.320	0.0512	0.291	1.354
2	-78.27	2.610	0.954	0.314	0.0517	0.297	1.373
3	-76.78	2.490	0.932	0.309	0.0519	0.304	1.388
4	-75.26	2.167	0.901	0.305	0.0518	0.313	1.399
5	-73.71	1.531	0.857	0.300	0.0511	0.324	1.400
6	-72.13	0.512	0.799	0.297	0.0496	0.339	1.391
7	-70.53	-0.989	0.726	0.295	0.0470	0.359	1.365
8	-68.91	-3.042	0.641	0.297	0.0433	0.389	1.311
9	-67.29	-5.925	0.548	0.312	0.0377	0.446	1.234
10	-65.69	X	0.455	X	0.0286	X	X

Table 7.1: Values recorded for given number of coupled fibroblasts. X denotes that a value could not be recorded.

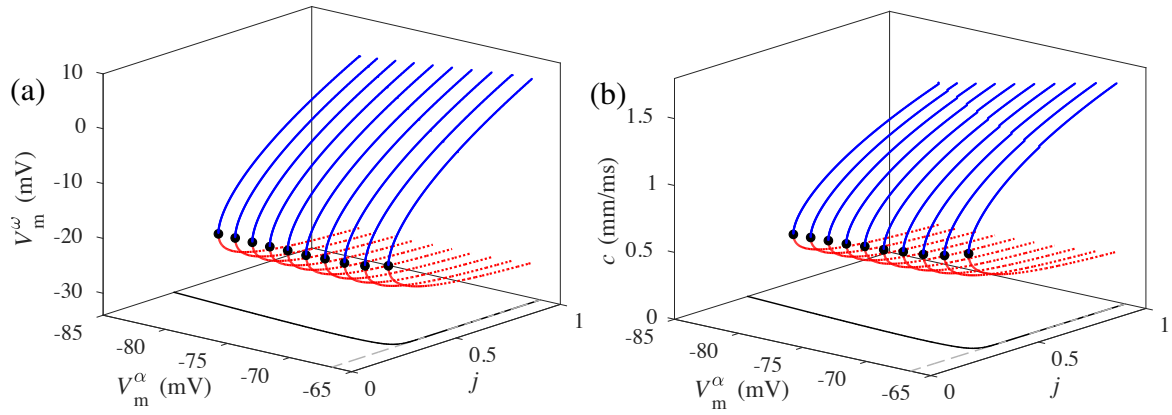

Figure 7.2: Selected components of the solution to the fast-time system (7.10) computed using the numerical method of [101]. (a) Wave speed c and (b) peak myocyte potential V_{m}^{ω} both as two-valued functions of the pre-front values of the myocyte potential V_{m}^{α} and of the slow inactivation gating variable of the myocyte sodium current j^{α}. The critical curve $j_{\text{crit}}^{\alpha}(V_{\text{m}}^{\alpha})$ below which the fast-time problem has no solutions is shown as a black curve in the $(V_{\text{m}}^{\alpha} - j^{\alpha})$-plane in both panels.

two distinct solutions can be found – one solution sitting in a stable branch corresponding to a faster speed c_1 (plotted with a solid blue line in Figure 7.2) and an one solution sitting in an unstable branch corresponding to a slower speed c_2 (plotted with a dashed red line in Figure 7.2). Other solution components are similarly two-valued functions of V_{m} and j^{α}. A more rigorous demonstration of these assertions can be found in [103] where closed-form analytical solutions are presented for a conceptual model with a similar asymptotic structure. For the particular atrial kinetics of [16] considered here, a regular perturbation approximation of the critical curve $j_{\text{crit}}^{\alpha}(V_{\text{m}}^{\alpha})$ and of the wave speed c has been reported in [101] and a solution in terms of iterated integral expressions has been presented in [102].

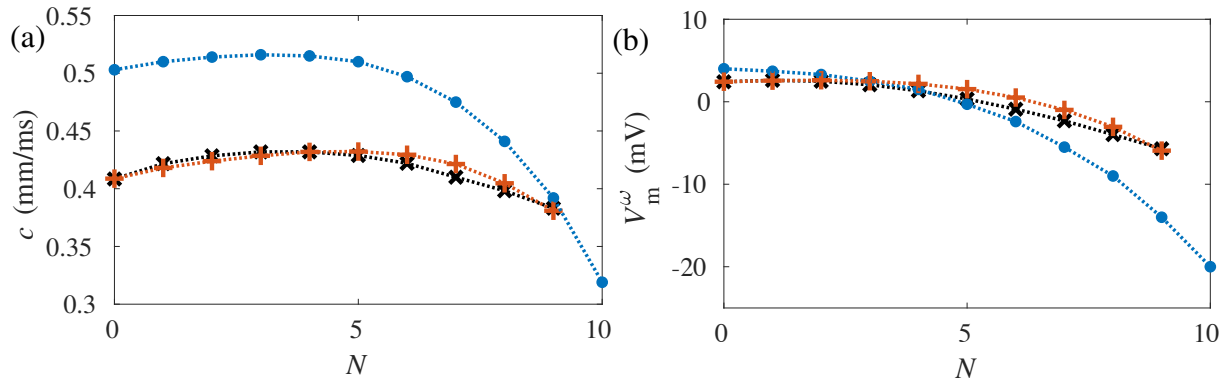

Figure 7.3: Selected components of the solution to the fast-time system (7.10) computed using the numerical method of [101]. (a) Wave speed c and (b) peak myocyte potential V_m^ω both as two-valued functions of the pre-front values of the myocyte potential V_m^α and of the slow inactivation gating variable of the myocyte sodium current j^α. The critical curve $j^\alpha_{crit}(V_m^\alpha)$ below which the fast-time problem has no solutions is shown as a black curve in the $(V_m^\alpha - j^\alpha)$-plane in both panels.

7.2.4 Analytical Model Validation

In order to validate this reduced model, the predicted values of the wave speed and post-front voltage can be compared with the simulated values from the direct numerical simulations, which are shown in Figure 6.6. In the work by [101] they find the relative error of the wave speed of the full model compared to the reduced model to be 16.0%.

The wave speeds from the full system (shown in Figure 6.6) can now be compared with the predicted wave speed from the full system using V^α defined by both numerical simulations and analytical solutions. Figure 7.3a) shows that the wave speeds from the full model and the reduced model solutions has a relative error of 19.1% when $N = 0$, which decreases as N is increased. So, it is reasonable to continue to use the same form for $M(V)$ and $H(V)$. It should be noted that as there was a change of variables thus the full model was adjusted by $c = \sqrt{D}^{-1}C$, where $D = \sigma/\chi C_m$. Both of the curves, using V_α from direct numerical simulations (orange plus marks in Figure 7.3a) and the predicted values of V_m^α from the analytical equations (7.4)a (black crosses), almost converge at $N = 9$, however their respective curvatures compared to the simulated values imply that they would start diverging after this point.

A similar result is shown in Figure 7.3b) which compares the maximum amplitude of the direct numerical simulations and the analytical results from the reduced model for V_ω. These results, again, have similar qualitative properties, again with approximately 19% relative error and have similar qualitative properties, but also for the lower values of N a similar quantitative values. Note that, these results do not need to be re-adjusted.

Condition for Propagation

The equilibrium solution of the slow subsystem can be coupled to the solution of the fast subsystem. The resting myocyte potential, V_m^α and the resting value of the slow inactivation gating

variable of the myocyte sodium current j^α in the tissue serve as pre-front values for the propagating wave front.

In practice, expressions (7.4) and (7.7) are first used to approximate $V_{\mathrm{m}}^\alpha(N)$ and $j^\alpha(N)$ and these are then used as inputs to the fast-time boundary value problem 7.10 which is solved by the numerical method of [101]. These asymptotic results are plotted in Figure 7.3 and compared with the wave speed and the peak myocyte potential measured from direct numerical simulations of the monodomain tissue equations (5.30) performed as described in section as discussed in Section 6.3.2. The relative error between the asymptotic approximation to the wave speed and the values from the direct numerical simulations is approximately 19% at $N = 0$ and decreases with increasing N. To split the error contributions due to the asymptotic reduction from those due to the linearisation of currents near the resting state, also in Figure 7.3 there are plotted the curves computed using pre-front values V_{m}^α and j^α obtained from direct numerical simulations rather than from expressions (7.4) and (7.7) but still solving the fast-time boundary value problem. Errors due to the asymptotic reduction dominate.

With the insight from the asymptotic reduction and consequent coupling, the occurrence of propagation failure with increasing fibroblast count can now be easily understood. Propagating front solutions to the fast subsystem 7.10 exist if and only if a point $(V_{\mathrm{m}}^\alpha, j^\alpha)$, with abscissa given by the value of the pre-front myocyte potential and ordinate given the pre-front value of the slow inactivation gating variable of the myocyte sodium current j, belongs to the region in the (V_{m}, j)-plane located above the critical bifurcation curve $j_{\mathrm{crit}}^\alpha(V_{\mathrm{m}}^\alpha)$ as plotted in Figure 7.2 while propagating front solutions do not exist in the region under the curve. The $j_{\mathrm{crit}}^\alpha(V_{\mathrm{m}}^\alpha)$ curve, therefore serves as the boundary between absolute and relative refractoriness, i.e. the boundary between the ability and the inability of the medium to conduct excitation waves. Refractoriness is a fundamental characteristic of biological excitable media, including cardiac tissues. On the other hand, for a given fibroblast count N, the values of V_{m}^α and j^α are determined from the solution of the slow subsystem, i.e. the system with the fast variables removed. In the special case of propagation of a single action potential through a rested tissue, these are given by equations (7.4) and (7.7) for the equilibrium values of myocyte potential and the slow inactivation gating variable of the myocyte sodium current. Therefore, propagation is possible if these values fall within the region of relative refractoriness above the critical curve $j_{\mathrm{crit}}^\alpha(V_{\mathrm{m}}^\alpha)$ and failure occurs if these values fall within the region of absolute refractoriness below $j_{\mathrm{crit}}^\alpha(V_{\mathrm{m}}^\alpha)$. In Figure 7.4 the $j_{\mathrm{crit}}^\alpha(V_{\mathrm{m}}^\alpha)$ as well as the curve $\left(V_{\mathrm{m}}^\alpha(N), j^\alpha(N)\right)$ parametrised by the fibroblast count N are plotted together in the (V_{m}, j) plane. The intersection of these two curves determines the critical fibroblast count N_{crit} beyond which propagation failure occurs. The N_{crit} is denoted in Figure 7.4 and is bracketed between $N = 9$ and $N = 10$ in full agreement with the results from direct numerical simulations, see Figure 6.6 and discussion in Section 6.3.2. Figure 7.4 also indicates that the intersection between the two curves occurs at a point far along the vertical asymptote $V_{\mathrm{m}}^\alpha = E_h$ of the fast-time system critical curve $j_{\mathrm{crit}}^\alpha(V_{\mathrm{m}}^\alpha)$. This observation allows us to derive an

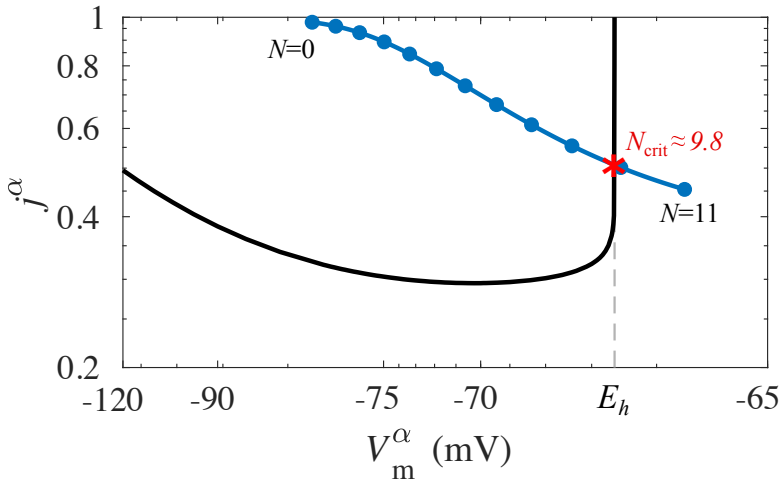

Figure 7.4: Critical fibroblast count N_{crit} beyond which propagation failure occurs. The thick solid black curve is the critical refractoriness boundary curve $j^{\alpha}_{\text{crit}}(V^{\alpha}_{\text{m}})$ for the existence of solutions to the fast-time system as also shown in Figure 7.2. The blue curve is the locus of pairs of equilibrium values of the j-gate and the myocyte potential $\left(V^{\alpha}_{\text{m}}(N), j^{\alpha}(N)\right)$ for fibroblast counts N as denoted by circle markers along the curve. The value of N at the intersection point marked with an asterisk is the critical fibroblast count $N_{\text{crit}} \approx 9.8$. With $G_{\text{f}} = 0.23$ nS and $G_{\text{m}} = 2.2$ nS.

explicit expression for the critical fibroblast count as a function of the parameters of the problem. Indeed, the algebraic equation $V^{\alpha}_{\text{m}} = E_h$, where V^{α}_{m} is given by (7.4) and $E_h = -66.6$, is linear in N and solving this equation finds the approximation,

$$N_{\text{crit}} = \frac{G_{\text{m}}\left(G_{\text{f}} + G_{\text{gap}}\right)\left(V^{0}_{\text{m}} - E_h\right)}{G_{\text{f}} G_{\text{gap}}\left(E_h - V^{0}_{\text{f}}\right)}. \tag{7.11}$$

Specific biomarker values reported from the direct numerical simulations in Chapter 6 also depend on the rest of the model parameters. One model parameter with value poorly constrained from experiments is the myocyte-fibroblast coupling conductance G_{gap}. In the above, the value of G_{gap} was chosen largely for numerical convenience. Now, with the help of the asymptotic theory developed here the dependence on myocyte-fibroblast coupling conductance G_{gap} can be constructed easily. Figure 7.5(a) shows the critical number of coupled fibroblasts N_{crit} as a function of the value of myocyte-fibroblast coupling conductance G_{gap} plotted from expression 7.11. Figure 7.5(b) shows the variation of the resting coupled myocyte and fibroblast potentials and the resting value of the slow inactivation gating variable of the myocyte sodium current j with variation of G_{gap} computed from equations (7.4) and (7.7). Results from direct numerical simulations of the uniformly distributed fibroblast case at fixed $N = 4$ are also plotted there and show excellent agreement. This serves to demonstrate that the asymptotic theory remains qualitatively valid. It has been too expensive to compute the entire critical curve as a function of G_{gap} by direct simulations. It is likely that the conceptual interpretation and the qualitative conclusions of the asymptotic theory remain true for a wide range of parameters, in the same way as for the variation with G_{gap}.

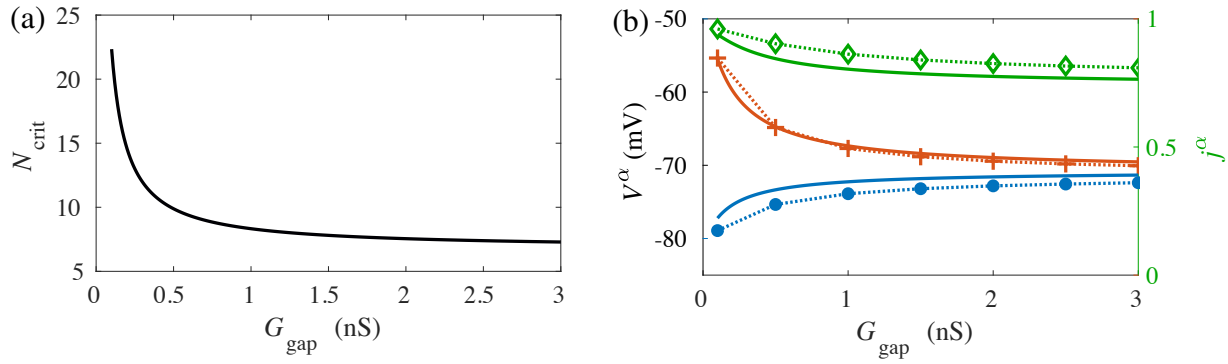

Figure 7.5: Dependence on myocyte-fibroblast coupling conductance G_{gap}. (a) Minimal number of coupled fibroblasts necessary for propagation N_{crit} computed from equation 7.11. (b) Resting (pre-front) potentials and j gate values computed from (7.4) and (7.7) as well as from direct numerical simulations. Same formatting conventions as in Figure 7.1 are used with V_{m}^{α} and V_{f}^{α} on the left y-axis and j^{α} on the right y-axis. Fibroblast count is fixed to $N = 4$ in (b). With $G_{\text{f}} = 0.23$ nS and $G_{\text{m}} = 2.2$nS.

7.3 Comparison of Fibroblasts and Myofibroblasts

As with the myocyte-fibroblast system, the myocyte-myofibroblast system can also be further explored by exploiting the fast and slow subsystems. Again, by fitting the analytical equations of the resting potentials (Equations (7.4)) to data from DNSs from Section 6.4 (as seen in Figure 6.12) the membrane conductances values can be chosen, specifically $G_{\text{m}} = 2.0$nS and $G_{\text{f}} = 1.5$nS. Using these values of the membrane conductances, the critical value of N can be found by substituting them into Equation (7.11), which can be seen in Figure 7.6. For the intercell conductance, $G_{\text{gap}} = 0.5$nS, the critical value of N is $N_{\text{crit}} \approx 1.9$. As with the fibroblast-myocyte case, the predicted critical value is close to the critical value of the DNSs, where $N_{\text{crit}} = 2$. As expected from the direct numerical simulations, the critical values for N is far less than in the myocyte-fibroblast case.

7.4 Discussion of the Reduced Model

To explain the direct numerical simulation results presented in Chapter 6 asymptotic theory is applied to the case of uniform fibroblast distribution, based on earlier work by Simitev and Biktashev [103]. Action potential biomarkers values are obtained as hybrid analytical-numerical solutions of coupled fast-time and slow-time periodic boundary value problems and compare well to direct numerical simulations. The boundary of absolute refractoriness is determined solely by the fast-time problem and is found to depend on the values of the myocyte potential and the slow inactivation variable of the sodium current ahead of the propagating front of the action potential. These quantities are in turn estimated from the slow-time problem using a regular perturbation expansion to find the steady state of the coupled myocyte-fibroblast kinetics. The asymptotic theory captures, with remarkable accuracy, the block of propagation in the pres-

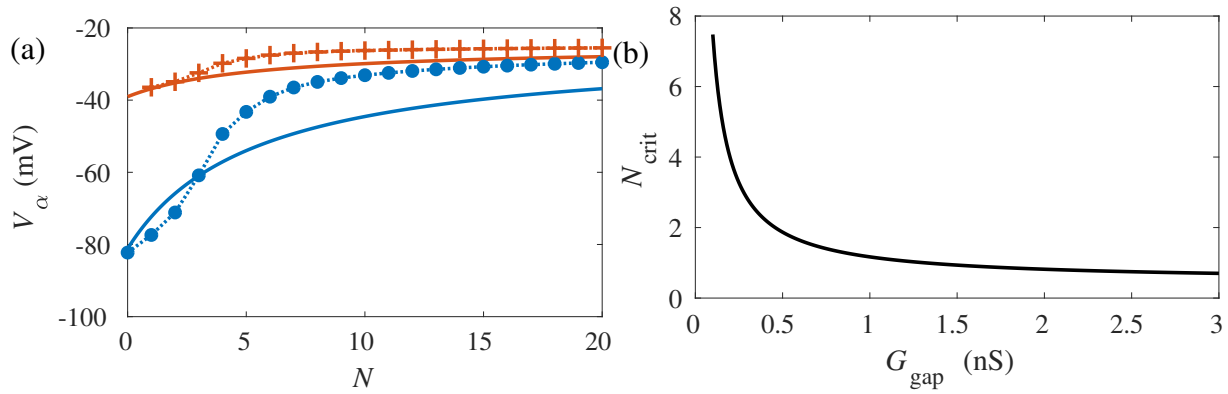

Figure 7.6: Fast and slow subsystem results in the myocyte-myofibroblast case. a) The resting (pre-front) myocyte potential V_m^α (solid blue curve) and myofibroblast potential V_f^α (solid orange curve) as functions of the number of fibroblasts per myocyte, N, evaluated from Equations (7.4). Dotted curves with blue circle markers and with orange plus-sign markers show values of V_m^α and V_f^α, respectively, measured from direct numerical simulations of (5.30) as discussed in Section 6.4. Fitted with the membrane conductance values of $G_m = 2.0$nS and $G_f = 1.5$nS. b) Minimal number of coupled fibroblasts necessary for propagation N_{crit} computed from equation (7.11).

ence of fibroblasts. This method of the reducing the model could be further applied to other combinations of myocyte and fibroblast models to find key information about the critical value of propagation and AP potential and speed, before any expensive direct numerical simulation would need to be performed. In future work, an asymptotic theory for the cases of non-uniform distributions $n(x,y)$ will lead to a set of spatially dependent ordinary differential equations for the steady state of the coupled myocyte-fibroblast model.

Chapter 8

Stem Cell Derived Cardiomyocytes Coupled with Human Embryonic Kidney Cells

In this chapter, the method of coupling multiple EP models will be applied in the final piece of work presented in this thesis, in which an electrophysiology model of human induced pluripotent stem cell derived cardiomyocytes (hiPSC-CM) is coupled to a novel model of a human embryonic kidney cell (HEK cell). This coupling considered the problem presented in work by A. da Silva Costa [17].

8.1 Introduction

Human iPSC-CMs have the potential to be used as an alternative to cardiomyocytes taken from animal tissue, in a range of fields, for example pharmatoxicity and regenerative medicine [9, 13, 39, 57, 60, 119]. A key feature of hiPSC-CMs is the spontaneous electrical activity which is considered to be an immature electrical phenotype [5, 39], rather than waiting to be triggered by an external stimulus, like with an adult ventricular cardiomyocyte. This is due to the presence of the pacemaker (or funny) current, I_{f}, [119] and a lack of the inward rectifying current, I_{K1}, [39, 40, 119], which maintains a stable resting transmembrane potential [22, 40]. With a normal adult level of expression of inward rectifier the resting potential is held close to the equilibrium potential of K^+ (E_{K}) [31].

In work by A. da Silva Costa et al [17], the hiPSC-CMs were co-cultured with HEK-293 cells in two cases. With the HEK cells that are not expressing the inward rectifying current, I_{K1} (known as wildtype HEK cells, HEK-WT), and with HEK cells expressing I_{K1} (HEK-K1). This was done in an attempt to find out whether the connections to the HEK-K1 cells could introduce sufficient I_{K1} to overcome the spontaneous nature of the hiPSC-CMs. The two cells were co-cultured and had recordings taken over a range of ratios of HEK cells to hiPSC-CMs,

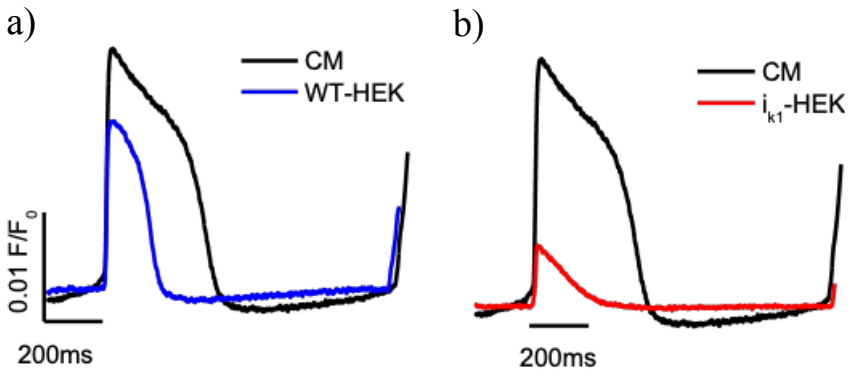

Figure 8.1: Examples of the fluorescence traces with HEK-WT and HEK-K1, relative to their diastolic fluorescence (F_0) from [17].

specifically 1:30, 1:10, 1:3 and 1:1. These were compared with a baseline case, the culture with only hiPSC-CMs. From these experiments, the action potentials were assessed by a fluorescent dye, FluoVolt^{TM} and the fluorescence traces were recorded. The cells were dyed with the FluoVolt^{TM}, which while being shone with a excitation light source, will emit light that is dependent on the potential of the culture. The recorded traces of the fluorescence are dependent on the culture, for example, the co-cultured arrays have an increased fluorescence amplitude (or the diastolic fluorescence, F_0). An increase in the fluorescence relates to an increase in potential, with the AP traces being recorded as the change in this fluorescence over the time of the action potential.

8.2 Experimental Results

Examples of the recorded fluorescence traces (relative to their diastolic fluorescences, F_0), are seen in Figure 8.1, in which traces from cultures in which hiPSC-CMs were co-cultured with HEK-WT and CMs with HEK-K1 are compared to the fluorescence traces from purely hiPSC-CM cultures. These traces have been averaged to remove the noise from the AP traces and show a reduced amplitude in fluorescence, and a variation in the time course when the hiPSC-CMs are co-cultured with either variety of the HEK cells. While the fluorescent dye does not give a precise value for the amplitude of the action potential, or the transmembrane potential, the time course is accurate, and values such as the APDs and the cycle times can be reliably recorded. In Figure 8.2, the APDs of the three cultures at 20%, 50% and 90% repolarisation are shown. When the CMs are co-cultured with the HEK-WT cells the APDs all decrease. Whereas when the hiPSC-CMs are cultured with the HEK-K1, the APD_{20} and APD_{50} decrease even further, but the APD_{90} is larger than the APD_{90} in the HEK-WT case. This reflects a more triangular AP shape in the HEK-K1 culture, as seen in Figure 8.1.

Another key value is the cycle length, the time between individual APs. The percentage of

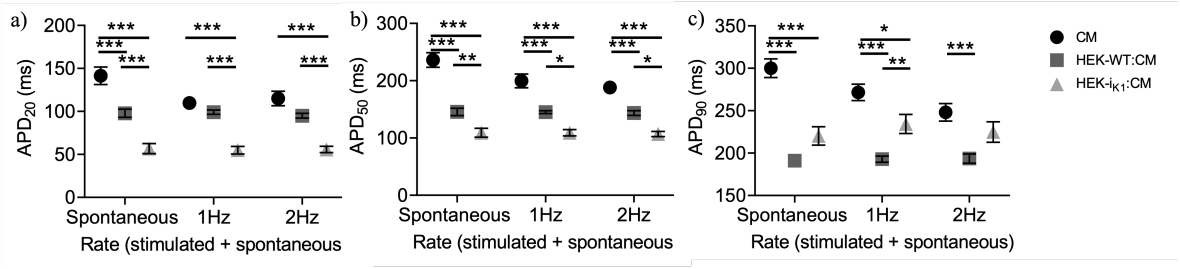

Figure 8.2: Action potential durations from a)purely CM culture, b)CM and HEK-WT cultures, and c) CM and HEK-K1 culture, [17].

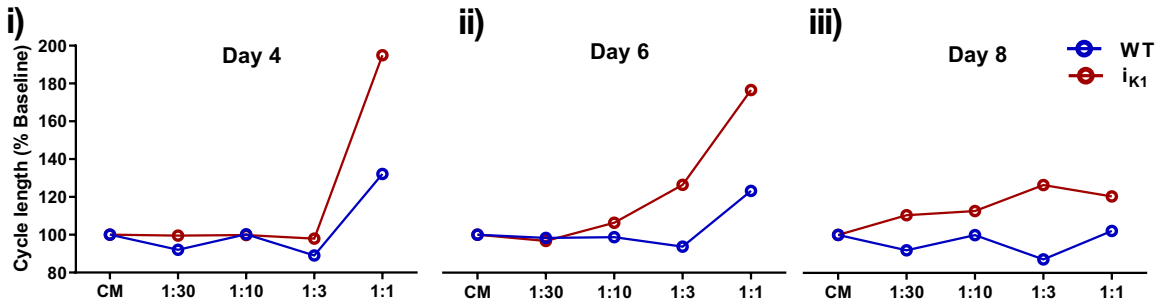

Figure 8.3: Examples of the cycle lengths, as percentages, the CM only culture as the standard cycle length on three different days with HEK-WT and HEK-K1 co-cultures, relative to the CM only cycle times, from [17].

the cycle lengths of the cultures were recorded over 8 days in the CM only culture (the baseline case, set to be 100%) and the HEK-WT and HEK-K1 cultures, for a range of CM to HEK ratios, (1:30, 1:10, 1:3, and 1:1). Examples of the average recorded cycle times on days 4, 6, and 8 are seen in Figure 8.3. These results show that, as theorised, the cycle lengths increase when the CMs co-cultured with HEK expressing I_{K1} and increases as the ratio changes from 1:30 to 1:1. However, the presence of the HEK-K1 cells does not entirely stop the spontaneous action potential activation of the hiPSC-CMs. When the CMs are co-cultured with wildtype HEK cells the cycle lengths stay at approximately at 100%, except when the ratio reaches 1:1, where the cycle length increases [17].

8.3 Mathematically Modelling the Electrophysiology of hiPSC-CMs with HEK cells

In this section the mathematical models of the hiPSC-CM and HEK cells are introduced. These models will then be coupled at the single cell level, using the same method that was described in Section 5.5, with multiple cardiomyocytes coupled to a single HEK cell. Unlike the work with the myocytes and fibroblasts, the number of each type of cell will be considered as a ratio, to better reflect the experimental results. In the experiments there are more cardiomyocytes than HEK cells and so N defines the number of cardiomyocytes per HEK cell and it is this that is used

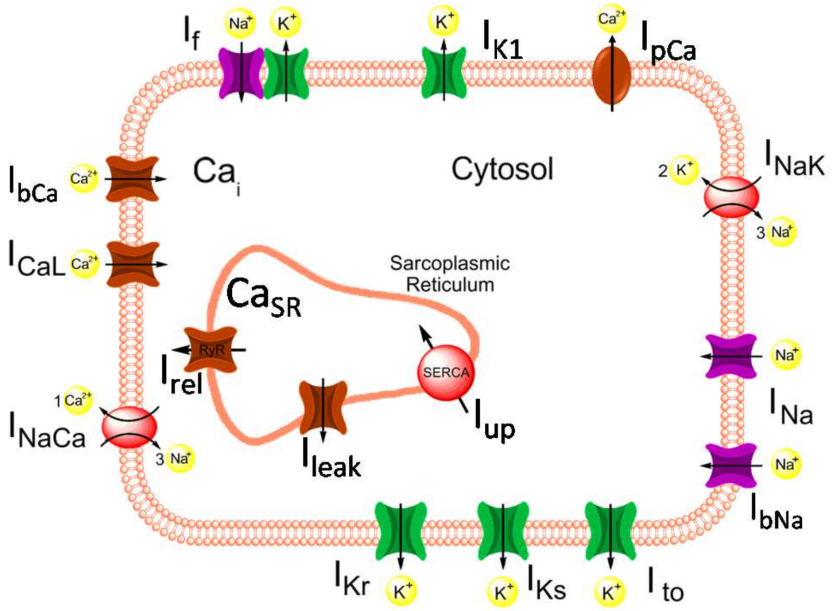

Figure 8.4: Schematic diagram of the currents and subcellular regions included in the EP model of hiPSC-CMs by Paci et al. [75].

to define this ratio of cardiomyocytes to HEK cells, for example, if N=30, the myocyte to HEK cell ratio is 30:1. In this form of the system, there is only ever one HEK cell. To go beyond a 1:1 ratio, to have more myocytes than HEK cells, N is inverted, so for a CM to HEK cell ratio of 2:1 we would define N=1/2. This form also means there is no intercell-cell connection between the cardiomyocytes, although it is assumed that there is no intercell variation and thus the work does not require connections between the cardiomyocytes or any spatial variation.

8.3.1 Mathematical Model of hiPSC-CMs

There is a well established model of the stem cell derived cardiomyocytes by Paci et al [75]. This is an ion current model of the transmembrane potential. This model includes 12 ion currents, namely, the fast sodium current, I_{Na}, the L-type calcium current, $I_{\text{Ca,L}}$, hyperpolarisation-activated cyclic nucleotide-gated funny current, I_{f}, the transient outward I_{to}, the rapid and slow delayed rectifier currents, I_{Kr} and I_{Ks} respectively, the inward rectifier current, I_{K1}, the sodium-calcium exchanger, I_{NaCa}, sodium-potassium pump, I_{NaK}, the sarcolemmal calcium pump current, I_{pCa}, and the background currents I_{bNa} and I_{bCa}, respectively. A schematic of these channels can be seen in Figure 8.4.

8.3.2 Mathematical Model of HEK cells

There is no established EP model of HEK cells, with or without the expression I_{K1}. However, a novel model of the HEK cell has been formulated using existing forms of the relevant ion channels and data from studies of the cells. The HEK cells in the experiments by da Silva Costa

et al. [17] can be assumed to have two currents, the wild type current, I_{WT}, and the inward-rectifying potassium current, I_{K1}. The wild type current is a background current, which are traditionally defined in mathematical models with a linear relationship. In a paper by Thomas and Smart [112] the transmembrane current of the wildtype HEK is recorded when the cell is held constant over a range of potentials. Thus, they have data for a current-voltage relationship, to which the linear relationship of the wildtype current can be fitted to. Their data measures the HEK cell to be at rest (a current of 0pA/pF) when the voltage is approximately at -10mV. However, in literature it is established that the wild type HEK cell is at rest of -30mV [17]. Thus, the linear relationship of the wildtype current is set to pass through the point of no current when -30mV, and the gradient of this relationship is derived by fitting the line to the data from Thomas and Smart (2005) [112]. This current voltage relationship can be seen in Figure 8.5a). It should be noted that the data of the current has been normalised and thus the physiological magnitude cannot be found from this data. However, the magnitude can be estimated from data of HEK cells that are expressing I_{K1}, from Boer et al (2006) [20], which has data of the transmembrane current of an HEK-K1 cell and is discussed further below.

In order to derive a current-voltage relationship of the I_{K1} current in an HEK cell, data from Boer et al [20] is used. These data are the transmembrane current of the whole cell and thus is the summation of the wild type current as well as the K1 current. There is an established form for the I_{K1} IV curve, namely that for negative potentials, the current has a positive gradient, that comes to a peak as the potential increases, the decreases monotonically, tending to 0pA/pF as the potential increases further. Thus, by looking at the data from Boer et al. (seen in Figure 8.5b), for the large positive potentials, the current begins to increase again, thus we know this is solely from the wildtype current. Thus the HEK-WT current can be normalised about the largest potential and the IV curve that is only due to the I_{K1} current can be found. Also, since the Boer et al data is not normalised, this process also gives a physiological magnitude to I_{WT}.

The form of the I_{K1} current equation is established in many mathematical electrophysiological models [63] and so using the data by Boer et al [20] and the wild type current the parameters can be found by fitting the curve to the data. This fitted current is shown in Figure 8.5b), along with the wild type current and the total current.

$$C_{\mathrm{m}}\frac{dV_{\mathrm{m}}}{dt} = -\left(I_{\mathrm{m}} + G_{\mathrm{gap}}\left(V_{\mathrm{m}} - V_{\mathrm{H}}\right)\right), \tag{8.1}$$

$$C_{\mathrm{H}}\frac{dV_{\mathrm{H}}}{dt} = -\left(I_{\mathrm{WT}} + I_{\mathrm{K1}} + nG_{\mathrm{gap}}\left(V_{\mathrm{H}} - V_{\mathrm{m}}\right)\right), \tag{8.2}$$

$$I_{\mathrm{WT}} = 0.0726\left(V_{\mathrm{H}} + 30\right), \tag{8.3}$$

$$I_{\mathrm{K1}} = G_{K1}\frac{V_{\mathrm{H}} + 78.3651}{1 + 2.5156e^{\frac{V_{\mathrm{H}}+65.8558}{12.9710}}}, \tag{8.4}$$

where the m and H subscripts refer to the CMs and HEK cells, respectively. The capacitances

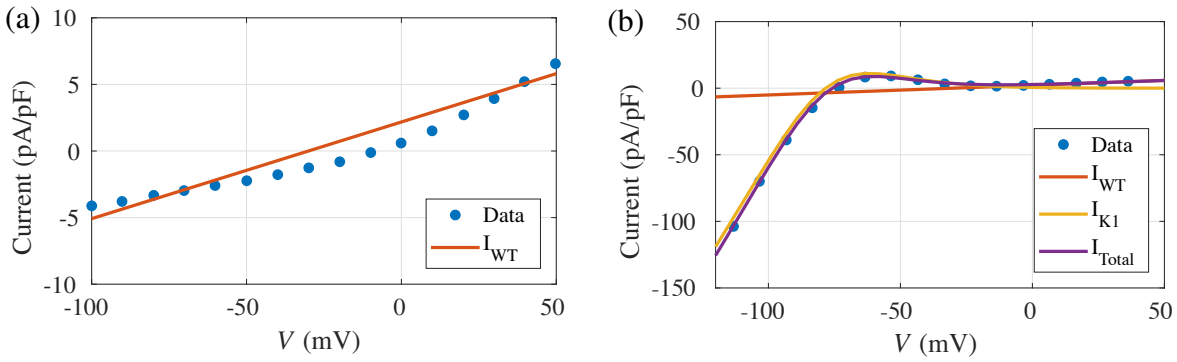

Figure 8.5: a) The wild-type current, I_{WT} fitted to data from Thomas and Smart [112]. Note that the units of the currents have been rescaled to match those in the HEK-K1 data. b) The wild-type current, I_{WT}, inward rectifying current I_{K1}, and the total current I_{Total} fitted to data from Boer et al [20].

are denoted, C_*, is the capacitance of the cardiomyocyte where G_{K1} is the I_{K1} conductance and is estimated to be 2.9710S/F, from the Boer et al data [20]. I_{m} is the total of the myocyte currents, as defined by [75].

8.3.3 Measuring Results from the Potential of the Coupled System

The mathematical model of the coupled cells produce values for the potential in both cell types. However, it should be noted that the fluorescence recordings do not distinguish between the hiPSC-CM potential and the HEK cell potentials, and instead the experimental data is from an average of the two potentials. Thus, to compare the potentials the simulated APs are averaged taking into account the ratio of HEK cells to CM. It is this averaged potential that will be analysed in subsequent discussion. Examples of averaged potentials (at a 1:1 ratio) can be seen in Figure 8.9. For N cardiomyocytes per HEK cell, the average potential, V, is,

$$V = \frac{NV_{\mathrm{m}} + V_{\mathrm{H}}}{N+1}. \tag{8.5}$$

Also, when recording the action potential durations from the coupled system, it should be noted that the profiles of the hiPSC-CM action potentials have a very different shape compared other adult myocytes. Crucially due to its spontaneous behaviour, the initial depolarisation can start very gradually making it difficult to determine the “start" of the AP. So when measuring the action potential durations, the start of the action potential is defined to be when the potential is half of its maximum potential, i.e. the threshold that measures APD_{50}.

8.4 Simulation Results

In this section the results of the mathematical model are presented.

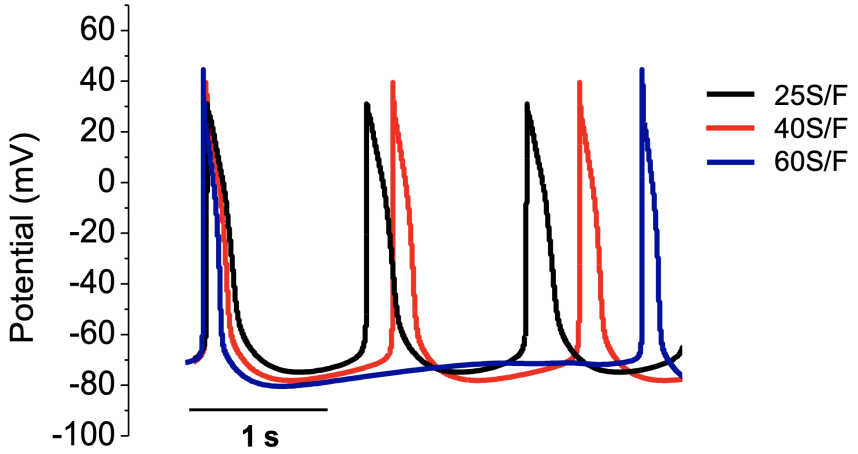

Figure 8.6: Action potentials, with G_{K1}=25, 40, 60S/F over multiple cycles.

8.4.1 Results from the Uncoupled hiPSC-Cardiomyocytes

Before coupling the two cell types, the properties of the baseline hiPSC-CM only case can be explored. In particular, how its behaviour is dependent on the strength of the existing inward rectifying current of the hiPSC-CM, I_{K1}. The strength of this current is changed by varying the channel conductance. In Figure 8.6, action potentials with three different values of G_{K1} are plotted over multiple cycles. This figure shows that the inward rectifying current impacts the AP time-course of the AP and also increases the time between the different action potentials, the cycle length. Figure 8.7 shows a range of EP dynamics, specifically the frequency of the APs, as well as the APDs, the amplitude of the APs and the maximum calcium concentration. These results show that as G_{K1} increases APD_{20}, APD_{50}, and APD_{90} all decrease. Although the amplitude of the AP and the maximum calcium concentration both increase as the current strength increases. However, most significantly as G_{K1} increases the frequency of the APs decrease, until it reaches 65S/F at which point the spontaneous behaviour ends and the action potentials are not produced.

8.4.2 Results from the Coupled System

There are no recorded values for an appropriate coupling strength, G_{gap}, between the hiPSC-CM and HEK cells. However, it can be chosen by fitting the model to the simplest case and the most accurate recorded values, specifically the APD_{20} and APD_{50} in the HEK-WT case. G_{gap} is varied with a ratio of 1:1, the results are seen in Figure 8.8. Using these results, the coupling strength, $G_{gap} = 0.7\,\text{nS}$, is chosen for the intercell coupling strength. It should also be noted that if the intercell conductance is increased sufficiently in the HEK-K1 case, the cycle length increases until eventually the spontaneous excitation ends and the system comes to a rest, as originally theorised. However, the spontaneous activity also eventually ends in the HEK-WT case, but without a significant increase in the cycle length. Although, it should be noted that,

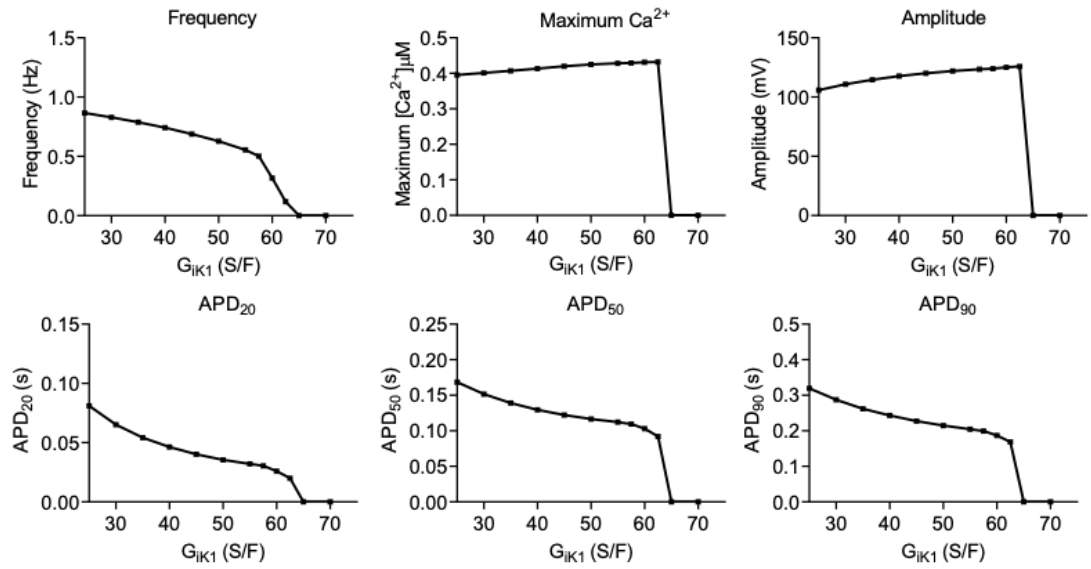

Figure 8.7: Results from varying G_{K1} in an uncoupled hiPSC-CM.

unlike the HEK-K1 case, the HEK-WT AP amplitude reduces significantly as G_{gap} increases, which may be the reason the spontaneous activity stopped. This can be seen in Figure 8.8.

Figure 8.9 shows the APs of the cardiomyocytes, the HEK cells, and the average AP, at a 1:1 ratio. When the HEK cells express I_{K1}, as seen in Figure 8.9b), the resting potential is reduced to approximately -80mV, compared to the resting of the HEK-WT, which is approximately -50mV. This has the effect of both keeping the resting potential down, compared to the HEK-WT, which quickly reaches a minimum value, but then begins to slowly increase until, ultimately, the next action potential if activated. This is a feature that is seen in the experimental AP profiles seen in Figure 8.1. From these AP traces it is also clear that the HEK potentials have a very small amplitude, compared to the amplitude of the hiPSC-CM potentials.

The dependence on the ratio of HEK cells to hiPSC-CM, is shown in Figure 8.11. Here the hiPSC-CM only case is represented by the ratio of 1:100 HEK cells to CMs. Unlike the experimental results (seen in Figure 8.3) with the wild type HEK cells, the cycle times decrease as the ratio changes to 1:1. However the cycle times relatively constant, with the HEK-K1 cells, and crucially is greater than those in the HEK-WT case. The difference increases as the Ratio varies to 1:1 and beyond. Although we do not have access to recordings of the calcium concentration, APDs, or the potential amplitudes, V^{amp}, for a range of ratios, Figure 8.11 displays these values. Notably, the APDs are all less than the 1:100 (or hiPSC-CM only case) and the APDs, when HEK-K1 cells are coupled, are less that their equivalent APDs when the wild-type HEK cells are couple. In the case of the APD_{90}, this contradicts what is seen in the experimental results.

The mathematical model and experimental results agree that the spontaneous nature can not be overcome in the current conditions. However, the mathematical model can be used to show that is the coupling strength, G_{gap} is increased, then if it is assumed that not all of the hiPSC-

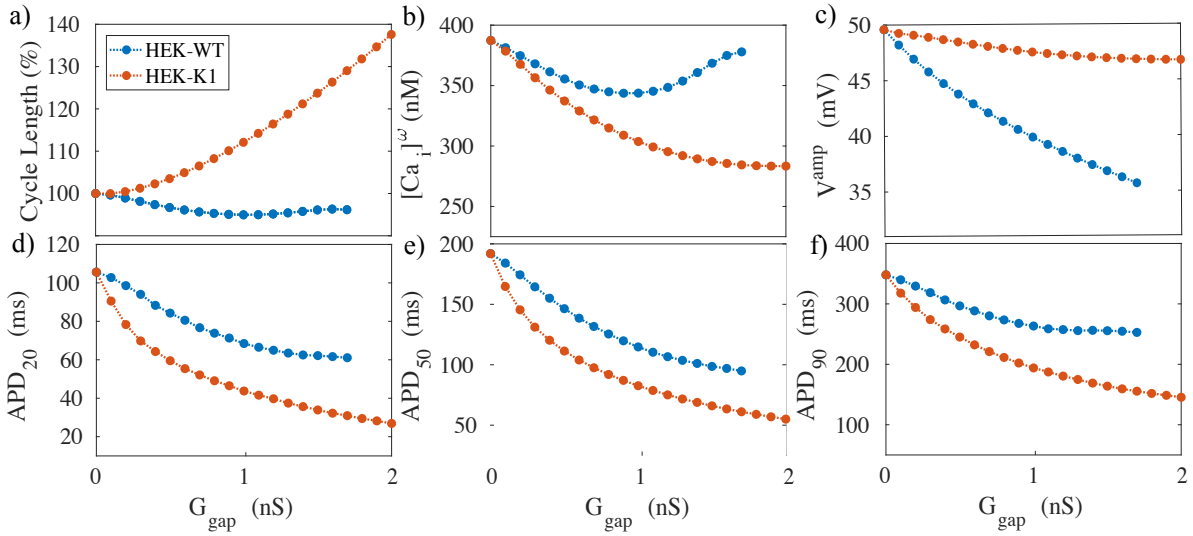

Figure 8.8: Results from varying G_{gap} with hiPSC-CM coupled with HEK-WT (blue) and HEK-K1 (orange) at a 1:1 ratio, a) the cycle lengths of the APs, b) the maximum calcium concentration c) the AP amplitude d) the APD_{20} e) the APD_{50} and f) the APD_{90}.

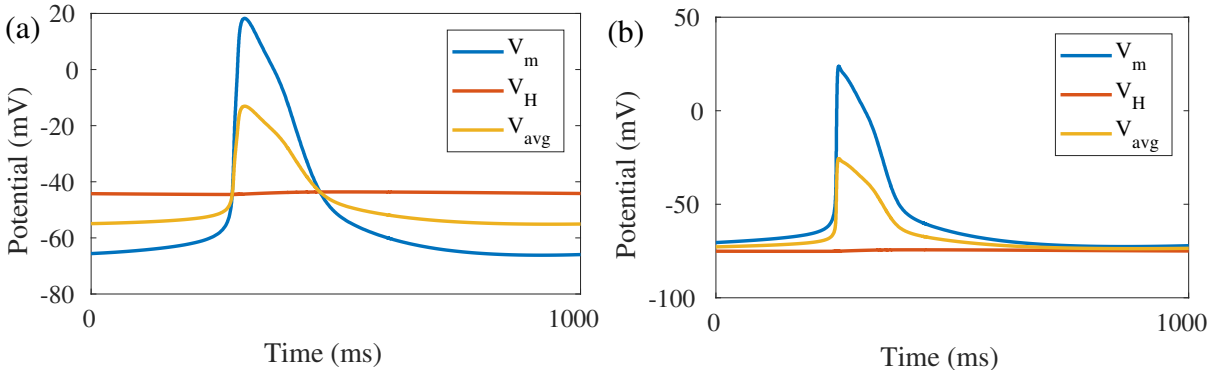

Figure 8.9: Action potential traces, when hiPSC-CM are coupled with HEK cells at a 1:1 ratio a) when the cardiomyocytes are coupled with wild-type HEK cells b) when the cardiomyocytes are coupled with HEK cells expressing I_{K1}.

CM are successfully be stimulated (as may well be the case) then, as seen in Figure **??**, the spontaneous nature can be overcome.

8.5 Discussion

The work done by da Silva Costa [17] developed an experimental model, co-culturing a partner cell (HEK cell) to the culture, coupling them with the cardiomyocytes. This work found that coupling to wild type HEK alone caused APD shortening. Coupling the hiPSC-CM to HEK cells expressing I_{K1} caused further shortening, but not in the APD_{90}. It was also shown that the presence of the HEK-K1 cells caused the cycle lengths to increase, and although the cells are less excitable, the spontaneous nature of the hiPSC-CM was not stopped entirely. In order to explore this phenomenon, a mathematical model has been created to see if it can be explained.

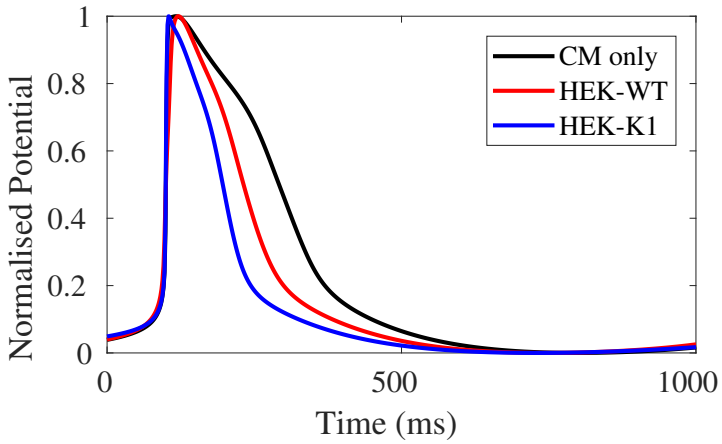

Figure 8.10: Normalised action potential traces from the CM only (black), HEK-WT (red), and HEK-K1 (blue) cases.

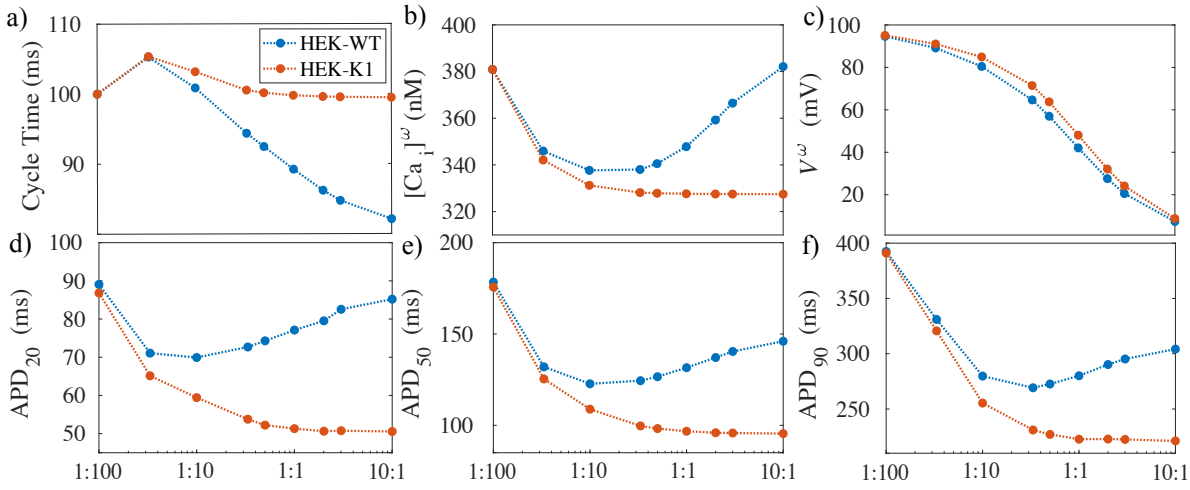

Figure 8.11: Results from varying the ratio of HEK cells to hiPSC-CM, with $G_{\text{gap}} = 0.7\,\text{nS}$, with HEK-WT in blue and HEK-K1 in orange, a) the cycle lengths of the APs, b) the maximum calcium concentration c) the AP amplitude d) the APD_{20} e) the APD_{50} and f) the APD_{90}.

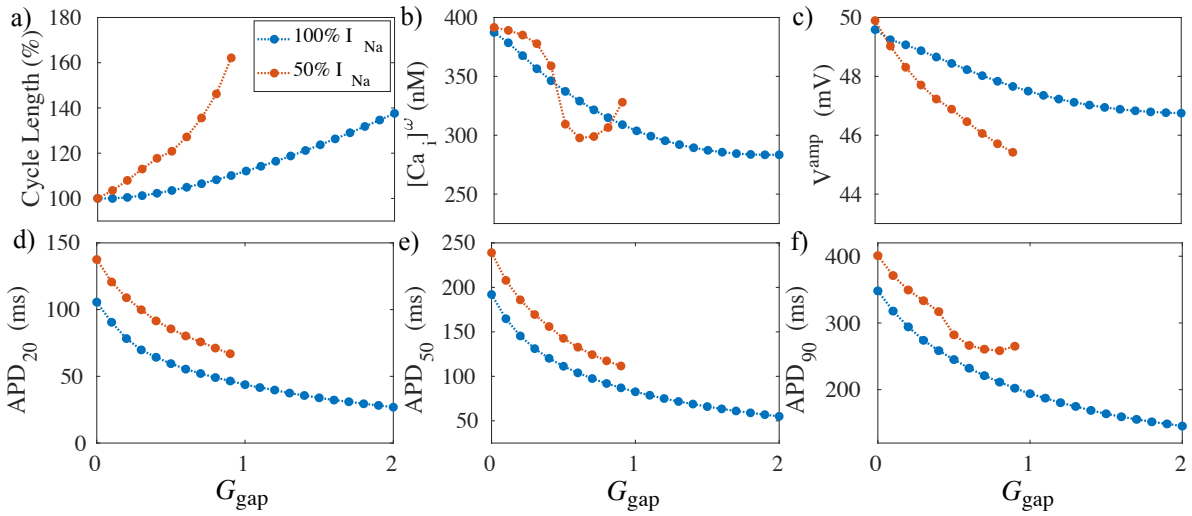

Figure 8.12: Results from varying G_{gap} with hiPSC-CM coupled with HEK-K1 at a 1:1 ratio, with regular (blue) sodium current and the sodium current reduced by 50% (orange). a) the cycle lengths of the APs, b) the maximum calcium concentration c) the AP amplitude d) the APD_{20} e) the APD_{50} and f) the APD_{90}.

Coupling of these types of cells has not been reported in the literature and an electrophysiology model the HEK cell does not exist. However, using data from previous studies [20, 112] and accepted forms of existing current models for the background current and the inward rectifying current, a mathematical model of the HEK cells with and without the inward rectifying current was constructed. The equations defining the currents are fitted to the data and fit well, although no further verification of the model could be completed since there is no further recorded electrophysiology of HEK cells that could be used for comparison. Another part of setting up the model is the coupling strength between the cells. As there are no previous studies on the coupling of these cells, the intercell conductance that is appropriate for these cells is unknown. By coupling the hiPSC-CM with HEK-WT (at a 1:1 ratio) for a range of intercell conductance values and comparing the APD_{20}s and APD_{50}s with the experimental results, the appropriate conductance is chosen.

Before exploring the effects of the coupling, the uncoupled hiPSC-CM is considered for a range of inward rectifying current conductances. These results showed that with sufficient strength in I_{K1}, the spontaneous activity can be suppressed, as theorised. When the cells are coupled, the mathematical model of hiPSC-CM and HEK cells recapitulates many of the features seen in the experimental results. Firstly, when the cells are coupled at a 1:1 ratio the system using the HEK-K1 have an increased cycle length, in comparison to the system with the wild-type HEK cells. Secondly, when coupling of HEK cells to hiPSC-CMs is at a 1:1 ratio the values of APD_{20} and APD_{50} are less than the case with a CM to HEK ratio of 100:1. However, while the model predicts a decreased APD_{90}, whereas the experimental data indicate a prolongation of APD_{90}. The source of this disagreement between the experimental work and the mathematical work is unknown, but may be based in the very approximate estimates of the

baseline electrophysiology of the HEK cell which may contain conductances that are accessed by the very polarised potentials of these cells. However, it may also speak to more complex behaviour happening in the original experiments which would need to be further explored. The mathematical model also shows that the presence of the inward rectifying current from the HEK cells can cause an increase in the length of the cycles, and even inexcitability when the sodium current in the hiPSC-CM model is reduced to 50% of its usual level, which reflects a culture of hiPSC-CM that may not all be becoming excited.

This new model successfully recapitulates many of the experimental results and suggests that there may be a more complex system at play in the cultures. The model also suggests that if a cell that expresses a stronger inward rectifying current were to be used, then the spontaneous activation could be overcome. Future work in this project would work with the experimental researchers to design a new set of experiments that may lead to desired outcome of a quiescent stem cell derived cardiomyocyte.

Chapter 9

Discussion

The work presented in this thesis highlights many of the forms of intercellular connections that appear in cardiac cells, and how these connections affect the mechanical and electrophysiological properties of these cells. Specifically, three novel pieces of research are presented. Firstly, based on experiments performed by Huethorst et al. [41], the Rice model is repeatedly coupled in series to create a chain of contractile units, in order to explore how the contraction of a monolayer of cardiomyocytes is dependent on the rigidity of the substrate that they are attached to. Secondly, electrophysiological models of myocytes and fibroblasts (and also myofibroblasts) are coupled to show how the presence of the fibroblasts can stop the action potential propagation, particularly in three fundamental patterns of fibroblast distribution. Finally, based on work by A. da Silva Costa [17], human induced stem cell derived cardiomyocytes (hiPSC-CM) are coupled with human embryonic kidney cells (HEK cells) to explore if the spontaneous activation of the cardiomyocytes can be overcome if the HEK cells are expressing the stabilising inward rectifying current. All three of these pieces of research show that the intercell connections have a significant effect on the properties of the cells and can cause them to fail in their primary functions.

9.1 Project 1: Cardiomyocyte Contraction on a Substrate

The first novel piece of work presented is a mathematical model of a chain of contractile units suspended between two springs, to represent a monolayer of contracting hiPSC-CM attached to a substrate. This work successfully replicates the key characteristics seen in the experimental results. Specifically, as the substrate (or spring) stiffness increases, multi-peaked behaviour begins to appear. This feature becomes more prominent when intercell variation in the calcium profiles is introduced to the system, the more intercell variation the more enhanced the multi-peaked behaviour becomes. This work effectively links the multi-peaked behaviour seen in the contraction and the stiffness of there attachments holding them in place.

An interesting result of these simulations is that for longer chains of contractile units, there

is a dependence on the location within the chain. When the units are identical, the units in the centre of the chain are unable to move and the contraction of the units at the edges cause a wave to appear, shortening those units in the middle even after the calcium has left the system and there is no active force. As a result the total length change of the chain is relatively small, compared to the length of the chain. The same behaviour appears when calcium variation is introduced into the system, and although the cells in the middle are able to move more, any additional contraction is counteracted by adjacent units being stretched. Thus, again, there is little change in the length of the chain. This behaviour does not appear in nature. However, the wave can be removed by breaking up the chain by introducing springs between groups of contracting units. However, by introducing springs into the system the total length change of the chain is further reduced.

Although this model successfully exhibits the key phenomena observed in the experiments, there are still some differences. Specifically, in the experimental results, the profiles exhibiting multi-peaked behaviour have a similar shape to the profiles with the single-peaked profiles. Whereas, in the mathematical model the cases with increased rigidity in the springs, the multi-peaked behaviour has a much more triangular time-course. Although, the triangular profile of the positions is alleviated slightly when the a high level of variation in the calcium profiles introduced, with the average of the average positions having greater amplitudes, greater durations and less triangular shapes, than those in the case with identical units. The cause of the differences between the simulated and experimental position (or motion) profiles could be attributed to the following reasons. Firstly, the experimental measurements are performed on cardiomyocytes, whereas the mathematical model of the contractile units is a model of sarcomere contraction, which does not include many of the features of the myocyte, such as the intra-cellular structures which will contribute passive forces. It should be noted that in the experiments, although the profile shape is reliable, the experimental motion traces may not reliably capture the amplitude. This work also suggests that there may be a short coming in the formulations of the active force, which, like the contractile length changes, also produces a much more triangular profile in the coupled system, although this is unsurprising as the two values are dependent on each other. A second key difference is that the problem has been simplified to a one-dimensional problem, while the motion results of the experiments are taken from a two-dimensional area, which may be contributing to the shape of the motion and the multi-peaked behaviour. So, it would be of interest to upscale this system to a 2-dimensional system of contracting units, this would notably be closer to the system seen in the experiments, and may shed further light on mechanisms in play. This would be of great interest if this work were to be continued.

Beyond addressing differences between the simulated and experimental results, another area of interest to be explored when continuing this work is using the system with periodic boundary conditions. This would remove the dependence on the location of the unit is within the chain. However, to use the periodic boundary conditions a suitable mechanism to represent an attach-

ment to the substrate would be required. This would be an opportunity to introduce a passive force that is dependent on the position of the end of the units, rather than purely the unit length, which would prevent cells being pushed or pulled too far away from their original positions. In order to do this, the definition of the system would need to be reconsidered so that the unit lengths are defined by the positions as well as their internal forces. In the current system the positions are defined by the unit lengths and do not impact the results.

9.2 Project 2: Action Potential Propagation with Coupled Myocytes and Fibroblasts

The second piece of work presented is concerned with the pattern and density of fibroblast distribution and how they can cause the action potential to fail to propagate. This work considers a mathematical model of fibrous atrial tissue formulated in terms of a set of cardiac monodomain equations including a myocyte-fibroblast coupling current. Following the works of Xie et al. [122] and Qiao [79] an "attachment" approach is adopted to couple the human atrial myocyte model, by Courtemanche et al. [16], to the mammalian fibroblast model, by Morgan et al. [63]. A key advantage of the "attachment" approach is that it can be easily employed within a homogenised continuum model such as the monodomain equations and a variety of fibroblast distributions can be prescribed simply and acutely. To model the myocyte in the system the atrial model of [16] is chosen as partial asymptotic results were readily available from earlier work [101] for this specific kinetics and because the numerical code is already validated in this case against the benchmark of [71] and is reported in work by Mortensen et al. [64]. For direct numerical simulations of the monodomain equations the Strang operator splitting method is used.

Using this setup, three fundamental fibroblast distributions: uniform distribution, fibrosis barrier distribution and myocyte strait distribution, are investigated. It is hypothesized that these fundamental distributions are the constituent blocks of realistic fibroblast distributions. Essential action potential biomarkers that are typically measured in electrophysiological cardiac tissue experiments including conduction velocity, maximum potential, action potential duration, and triangulation index are estimated from direct numerical simulations for all idealised distributions. Failure of action potential propagation is found to occur at certain critical values of the parameters that define each of the idealised fibroblast distributions and these critical values are accurately determined. In the case of uniform fibroblast distribution, it is found that electrical excitation fails to propagate when 10 or more fibroblasts are coupled per myocyte at the standard parameter values of the simulations. As fibroblast count increases from zero, peak potential decreases while conduction velocity slightly increases for mild fibrosis and then as the degree of fibrosis becomes more severe block occurs. The values of APD_{90} increase as the fibroblast count, N, increases until close to the propagation threshold when APD_{90} decreases rapidly. Sim-

ilarly, the calcium concentration stays relatively constant as N increases from N =0, until $N = 8$, after which it also falls off rapidly. In the case of fibroblast barrier where “healthy" tissue is separated by a region of fibrosis, the direct numerical simulations show that propagation block is determined by both the width of the fibrotic barrier and the number of fibroblasts coupled to each myocyte within it, N. For example, the more severe the fibrosis within the region the thinner it must be to allow successful AP propagation cross the barrier. From these simulations over a range of barrier widths, and values of N a threshold curve of fibroblast count versus width that splits propagation from failure. This curve is akin to strength-duration curves that are used elsewhere to determine the amplitude and the duration of a stimulus current that is needed to trigger excitation. Unlike in the first and third fibroblast distribution cases in this second case, the AP in the barrier is not appropriate to measure biomarkers as the fibrotic region not big enough. In the case of myocyte strait where channel of “healthy" tissue between two regions of fibrosis it was demonstrated that successful action potential propagation depends on both the width of the strait and the fibroblast count in the adjacent regions. For instance, the more severe the fibrosis of the surrounding region is, the wider the strait must be to admit the AP down it. Similarly, to the second case a threshold curve of the fibroblast count versus strait width that splits propagation from failure, is constructed. Although unlike in case 2, the action potentials were able to come to a constant form in the healthy strait and so the peak amplitude, the wave speed and APD_{90} could all be recorded. When the strait width is held constant, as the fibroblast density in the adjacent regions increases the wave speed, peak potential and the peak calcium concentration all decrease.

These tests were then repeated with the fibroblast model being redefined to be a model of myofibroblast electrophysiology, specifically by increasing the capacitance to C_f=50pF, to account for the increased size of the myofibroblast, and secondly by altering the inward rectifying current conductance to increase the uncoupled resting potential to -25mV [106]. In making these changes there is a significant effect on the quantitative results, although there is little change in the qualitative results. Most significantly the resting potential of the coupled cells increases much faster as the number of myofibroblasts increases. As a result when the myocyte-myofibroblasts system is applied to the uniform case (C1), the critical number of myofibroblasts that would allow propagation is 2. In cases with a fibrotic barrier and the myocyte strait (C2 and C3, respectively), even with the critical value being so low, the fibrotic barrier had to be much thinner than in the fibroblast case seen earlier, and the myocyte strait had to be much wider. These changes in the quantitative results in the experiments give much more physiological dimensions and cell ratios.

To explain these direct numerical simulation results asymptotic theory from earlier works [103] were extended and applied to the case of uniform fibroblast distribution. Action potential biomarkers values are obtained as hybrid analytical-numerical solutions of coupled fast-time and slow-time periodic boundary value problems and compare well to direct numerical simulations.

The boundary of absolute refractoriness is determined solely by the fast-time problem and is found to depend on the values of the myocyte potential and the slow inactivation variable of the sodium current ahead of the propagating front of the action potential. These quantities are in turn estimated from the slow-time problem using a regular perturbation expansion to find the steady state of the coupled myocyte-fibroblast kinetics. The asymptotic theory captures, with remarkable accuracy, the block of propagation in the presence of fibroblasts.

This work does not consider the effect of collagen formed in the fibrotic scar. This has been excluded as collagen is not electrically active and thus its main contribution is to alter the value of the effective potential diffusivity and this can be accounted for by simply rescaling the spatial variables in the governing equations. While this is, in theory, straightforward to account for realistic fibrosis distributions the collagen effect and the effects of tissue anisotropy are difficult to separate from the biomarker changes that are reported and so it should be included in simulations. This work also shows that for a large number coupled fibroblasts, the maximum internal myocyte calcium concentration is significantly less than in the fibroblast-free case, and, as discussed in Chapter 3, it is the calcium profile that triggers the myocyte contraction. Also, along with reduced calcium levels, the fibroblasts also increase the collagen density which will increase the passive forces in the system. So, the inclusion of fibroblasts is important when modelling cardiac muscle contraction.

There are multiple avenues for future work. Firstly, as discussed the presence of fibroblasts in tissue will undoubtedly impact the contraction of the tissue, due to both the increased collagen and the changes in the calcium concentrations, thus to mathematically model the contraction of a piece of fibrotic tissue, the fibroblasts must be included. Another piece of future work would involve combining the fundamental fibrotic patterns. For example, how will the propagation threshold be impacted by a fibrotic barrier within a myocyte strait? Also, is it possible to construct a theoretical scarred region that would cause arrhythmic patterns, to investigate if a complex fibrotic pattern is enough to prompt the arrhythmia. Another extension to the uniform fibrosis case could be further explored with a circular mesh, or alternatively a simpler 1D mesh with periodic boundary conditions. By setting up a wave travelling in one direction there will be a minimum circumference (or length) that will allow the AP to propagate, without it catching up to its own tail. However, as it is now known that increased levels of fibroblasts reduces the speed of the wave, the minimum circumference may be dependent on the fibroblast density. There is likely a threshold between the number of fibroblasts, N, and the mesh circumference, which may help in the understanding of tachycardia that can appear as a result of the scar being formed. Also, an asymptotic theory for the cases of non-uniform distributions $n(x,y)$ will lead to a set of spatially dependent ordinary differential equations for the steady state of the coupled myocyte-fibroblast model and will also be subject for further studies.

9.3 Project 3: Human Induced Pluripotent Stem Cell Derived Cardiomyocytes Coupled with Human Embryonic Kidney Cells

The final piece of work couples mathematical models of hiPSC-CM electrophysiology with an EP model of HEK cells, in order to investigate the problem presented by the work done by Costa et al. [17] who developed an experimental model, co-culturing a partner cell (HEK cell) to the culture, coupling them with the cardiomyocytes. This work found that coupling to wild type HEK alone caused APD shortening. Coupling the CM to HEK cells expressing I_{K1} caused further shortening, but not in the APD_{90}. It is also shown that the presence of the HEK-K1 cells caused the cycle lengths to increase, and although the cells are less excitable, the spontaneous nature of the hiPSC-CM is not stopped entirely. In order to explore this phenomenon, a mathematical model has been created to see if it can be explained.

Coupling of these types of cells has not been reported in the literature and a detailed electrophysiology model the HEK cell does not exist. However, using data from previous studies [20, 112] and accepted forms of existing ion current models for the back ground current and the inward rectifying current, equations defining the currents are fitted to the data and fit well, although no further verification of the model could be completed. Another part of setting up the model is the coupling strength between the cells. As there are no previous studies on the coupling of these cells, the intercell conductance that is appropriate for these cells is unknown. By coupling the hiPSC-CM with HEK-WT for a range of intercell conductance values and comparing the values of APD_{20} and APD_{50} with the experimental results, the appropriate intercell conductance, G_{gap}, is chosen.

Before exploring the effects of the coupling, the uncoupled hiPSC-CM is considered for a range of inward rectifying current conductances. These results proved that with sufficient strength in I_{K1}, the spontaneous activity can be suppressed. When the cells are coupled, the mathematical model of hiPSC-CM and HEK cells recapitulates many of the features seen in the experimental results. Firstly, when the cells are coupled at a 1:1 ratio the system using the HEK-K1 have an increased cycle length, in comparison to the system with the wild-type HEK cells. Secondly, when coupling of HEK cells to hiPSC-CMs is at a 1:1 ratio the values of APD_{20} and APD_{50} are less than the case with a CM to HEK ratio of 100:1. However, while the model predicts a decreased APD_{90}, whereas the experimental data indicate a prolongation of APD_{90}. This source of this disagreement between the experimental work and the mathematical work is unknown, but may be based in the very approximate estimates of the baseline electrophysiology of the HEK cell which may contain conductances that are accessed by the very polarised potentials of these cells. However, it may also speak to more complex behaviour happening in the original experiments which would need to be further explored. The mathematical model also shows that the presence of the inward rectifying current from the HEK cells can cause an increase in the

length of the cycles, and even inexcitability when the sodium current in the hiPSC-CM model is reduced to 50% of its usual level, which reflects a culture of hiPSC-CM that may not all be becoming excited.

This new model successfully recapitulates many of the experimental results and suggests that there may be a more complex system at play in the cultures. The model also suggests that if a cell that expresses a stronger inward rectifying current were to be used, then the spontaneous activation could be overcome. Future work in this project would work with the experimental researchers to design a new set of experiments that may lead to desired outcome of a quiescent stem cell derived cardiomyocyte.

9.4 Conclusion

The ultimate aim of this work is to outline the significance of intercell interactions that appear in cardiac tissue and that these interactions must be considered to properly model cardiac behaviour. Both electrophysiological and mechanical models are used in the work presented. As well as informing on the nature of the cells' behaviours, all three pieces of work show that is if these interactions are imbalanced the primary function of AP propagation or muscle contraction can be affected to the extent of failing to perform.

All three of the pieces of research highlight the impact of the intercell connections. The first piece of work showed that coupling contracting units in series caused multi-peaked behaviour. The second showed that pattern and the density of regular fibroblasts (or myofibroblasts) coupled myocytes with can cause the action potential to fail to propagate. And finally, the work of coupling hiPSC-CM cells with HEK cells the spontaneous activation of the hiPSC-CM can be overcome by the presence of HEK cells expressing I_{K1}. Not only do these pieces of work show that intercell connections have a profound impact on the behaviour of a system and should be carefully considered when researching these systems, but they also inform on the future research outside of mathematical models.

Bibliography

[1] Global, regional, and national incidence, prevalence, and years lived with disability for 310 diseases and injuries, 1990–2015: a systematic analysis for the global burden of disease study 2015. *Lancet*, 388:P1545–1602, 2016. doi: 10.1016%2FS0140-6736(16)31678-6.

[2] V. A. Barnett. *Cardiac Myocytes*, pages 113–121. Humana Press, Totowa, NJ, 2005. doi: 10.1007/978-1-59259-835-9_8.

[3] J. Baum and H. S. Duffy. Fibroblasts and myofibroblasts: What are we talking about? *Cardiovasc Pharmacol*, 57(4):376–379, 2011. doi: 10.1097/FJC.0b013e3182116e3.

[4] D. M. Bers. Altered cardiac myocyte ca regulation in heart failure. *Physiology*, page 380–387, 2006. doi: 10.1152/physiol.00019.2006.

[5] G. C. L. Bett, A. D. Kaplan, A. Lis, T. R. Cimato, E. S. Tzanakakis, Q. Zhou, M. J. Morales, and R. L. Rasmusson. Electronic "expression" of the inward rectifier in cardiocytes derived from human-induced pluripotent stem cells. *Heart Rhythm*, 10(12):1903–1910, 2013. doi: 10.1016/j.hrthm.2013.09.061.

[6] V. N. Biktashev, R. Suckley, Y. E. Elkin, and R. D. Simitev. Asymptotic analysis and analytical solutions of a model of cardiac excitation. *Bulletin of Mathematical Biology*, 70(2):517–554, 2008. doi: 10.1007/s11538-007-9267-0.

[7] S. D. Boothe, J. D. Myers, S. Pok, J. Sun, Y. Xi, R. M. Nieto, J. Cheng, and J. G. Jacot. *Cell Biochem Biophys*, 74(4):527–535, 2016. doi: 10.1007/s12013-016-0758-1.

[8] S. L. K. Bowers, I. Banerjee, and T. A. Baudino. The extracellular matrix: At the center of it all. *J Mol Cell Cardiol*, 48(3):474–482, 2010. doi: 10.1016/j.yjmcc.2009.08.024.

[9] P. W. Burridge, G. Keller, J. D. Gold, and J. C Wu. Production of de novo cardiomyocytes: human pluripotent stem cell differentiation and direct reprogramming. *Cell Stem Cell*, 10 (1):16–28, 2012. doi: 10.1016/j.stem.2011.12.013.

[10] P. Camelliti, T. K. Borg, and P. Kohl. Structural and functional characterisation of cardiac fibroblasts. *Cardiovascular Res*, 65.

[11] J. G. Canto, C. I. Kiefe, W. J. Rogers, E. D. Peterson, P. D. Frederick, W. J. French, M. Gibson, C. V. Pollack Jr, J. P. Ornato, R. J. Zalenski, J. Penney, A. J. Tiefenbrunn, and P. Greenlan. Number of coronary heart disease risk factors and mortality in patients with first myocardial infarction. *JAMA*, 306(16):2120–2127, 2011. doi: 10.1001/jama.2011.1654.

[12] K. Cardona, J. F. Gómez. J. M. Ferrero, S. Rajamani J. Saiz, and B. Trénor L. Belardinelli. Simulation study of the electrophysiological mechanisms for heart failure phenotype. *Computing in Cardiology*, 38:461–464, 2011.

[13] S. Casini, A. O. Verkerk, and C. A. Remme. Human ipsc-derived cardiomyocytes for investigation of disease mechanisms and therapeutic strategies in inherited arrhythmia syndromes: Strengths and limitations. *Cardiovasc. Drugs Ther.*, 31(3):325–344, 2017. doi: 10.1007/s10557-017-6735-0.

[14] L. Chilton, S. Ohya, D. Freed, E. George, V. Drobic, Y. Shibukawa, K. A. MacCannel, Y. Imaizumi, R. B. Clark, I. M. C. Dixon, and W. R. Giles. K^+ currents regulate the resting membrane potential, proliferation, and contractile responses in ventricular fibroblasts and myofibroblasts. *AJP Heart Circ Physiol*, 288:H2931–H2939, 2005. doi: 10.1152/ajpheart.01220.2004.

[15] M. A. Colman, M. Varela, J. C. Hancox, H. Zhang, and O. V. Aslanidi. Evolution and pharmacological modulation of the arrhythmogenic wave dynamics in canine pulmonary vein model. *Europace*, 16:416–423, 2014. doi: 10.1093/europace/eut349.

[16] M. Courtemanche, R. J. Ramirez, and S. Nattel. Ionic mechanisms underlying human atrial action potential properties: insights from a mathematical model. *American Journal of Physiology*, 275(1):H301 – H321, 1998. doi: 10.1152/ajpheart.1998.275.1.H301.

[17] A. da Silva Costa. *Investigation into the mechanisms determining spontaneous activity in human-induced pluripotent stem cell-derived cardiomyocyte*. PhD thesis, University of Glasgow, 2019.

[18] G. R. Dagenais, D. P. Leong, S. Rangarajan, F. Lanas, P. Lopez-Jaramillo, R. Gupta, R. Diaz, A. Avezum, G. B. F. Oliveira, A. Wielgosz, S. R. Parambath, P. Mony K. F. Alhabib, A. Temizhan, N. Ismail, J. Chifamba, K. Yeates, R. Khatib, O. Rahman, K. Zatonska, K. Kazmi, L. Wei, J. Zhu, A. Rosengren, K. Vijayakumar, M. Kaur, V. Mohan, A. H. Yusufali, R. Kelishadi, K. K Teo, P. Joseph, and S. Yusuf. Variations in common diseases, hospital admissions, and deaths in middle-aged adults in 21 countries from five continents (pure): a prospective cohort study. *The Lancet*, 2019. doi: 10.1016/S0140-6736(19)32007-0.

[19] M. Daniels, M. I. Noble, H. E. ter Keurs, and B. Wohlfart. Velocity of sarcomere shortening in rat cardiac muscle: relationship to force, sarcomere length, calcium and time. *J Physiol*, 355:367–381, 1984. doi: 10.1113/jphysiol.1984.sp015424.

[20] T. P. de Boer, T. A. B. van Veen, M. J. C. Houtman, J. A. Jansen, S. C. M. van Amersfoorth ND P. A. Doevendans, M. A. Vos, and M. A. G. van der Heyden. Inhibition of cardiomyocyte automaticity by electrotonic application of inward rectifier current from kir2.1 expressing cells. *Med Biol Eng Comput*, 44:537–542, 2006. doi: 10.1007/s11517-006-0059-8.

[21] E. D.van Deel, A. Najafi, D. Fontoura, E. Valent, M Goebel, K Kardux, I. Falcão-Pires, and J. van der Velden. In vitro model to study the effects of matrix stiffening on ca2+ handling and myofilament function in isolated adult rat cardiomyocytes. *J of Physiol*, 595 (14):4597–4610, 2017. doi: 10.1113/JP274460.

[22] A. S. Dhamoon and J. Jalife. The inward rectifier current (ik1) controls cardiac excitability and is involved in arrhythmogenesis. *Heart Rhythm*, 2:316–324, 2005. doi: 10.1016/j.hrthm.2004.11.012.

[23] A. J. Engler, C. Carag-Krieger, C. P. Johnson, M. Raab, H. Y. Tang, D. W. Speicher, J. W. Sanger, J. M. Sanger, and D. E. Discher. Embryonic cardiomyocytes beat best on a matrix with heart-like elasticity: scar-like rigidity inhibits beating. *J Cell Sci*, 121(22): 3794–3802, 2008. doi: 10.1242/jcs.029678.

[24] A. M Esfahani, J. Rosenbohm, K. Reddy, X. Jin, T Bouzid, B. Riehl, E Kim, J. Y. Lim, and R. Yang. Tissue regeneration from mechanical stretching of cell–cell adhesion. *Tissue Engineering Part C: Methods*, 25(11):631–640, 2019. doi: 10.1089/ten.tec.2019.0098.

[25] T. K. Feaster, A. G. Cadar, L. Wang, C. H. Williams, Y. Wook Chun, J. E. Hempel, N. Bloodworth, W. D. Merryman, C. C. Lim, J. C. Wu, B. C. Knollmann, and C. C. Hong. Matrigel mattress: A method for the generation of single contracting human-induced pluripotent stem cell-derived cardiomyocytes. *Circulation Research*, 117(12): 995–1000, 2015. doi: 10.1161/CIRCRESAHA.115.307580.

[26] R. Fitzhugh. Impulses and physiological states in theoretical models of nerve membrane. *Biophysical Journal*, 1(6):445–466, 1961.

[27] British Heart Foundation. British heart foundation. https://www.bhf.org.uk/heart-health/conditions/heart-failure, 2017.

[28] Y. C. Fung. Comparison of different models of the heart muscle. *J. Biomechanics*, 4: 284–295, 1971. doi: 10.1016/0021-9290(71)90035-2.

[29] Y. C. Fung. *Biomechanics: Mechanical Properties Of Living Tissues*. Springer-Verlag, second edition, 1993.

[30] B. Geiger, J. P. Spatz, and A. D. Bershadsky. Environmental sensing through focal adhesions. *Nat Rev Mol Cell Biol*, 10(1):21–33, 2009. doi: 10.1038/nrm2593.

[31] B. Goversen, N. Becker, S. Stoelzle-Feix, A. Obergrussberger, M. A. Vos, T. A. B. van Veen, N. Fertig, and T. P. de Boer. A hybrid model for safety pharmacology on an automated patch clamp platform: Using dynamic clamp to join ipsc-derived cardiomyocytes and simulations of ik1 ion channels in real-time. *Frontiers in Physiology*, 8, 2018. doi: 10.3389/fphys.2017.01094.

[32] C. O. Heras-Bautista, A. Katsen-Globa, N. E. Schloerer, S. Dieluweit, O. M. Abd El Aziz, G. Peinkofer, W. A. Attia, M. Khalil, K. Brockmeier, J. Hescheler, and K. Pfannkuche. The influence of physiological matrix conditions on permanent culture of induced pluripotent stem cell-derived cardiomyocytes. *Biomaterials*, (26):7374–7385, 2014. doi: 10.1016/j.biomaterials.2014.05.027.

[33] A. V. Hill. The heat of shortening and the dynamic constants of muscle. *Proc. R. Soc. Lond.*, 126:136–195, 1938. doi: 10.1098/rspb.1938.0050.

[34] A. L. Hodgkin and A. F. Huxley. Currents carried by sodium and potassium ions through the membrane of the giant axon of logio. *J. Physiol*, 116:449–472, 1952.

[35] A. L. Hodgkin and A. F. Huxley. The components membrane conductance in the giant axon of logio. *J. Physiol*, 116:473–496, 1952.

[36] A. L. Hodgkin and A. F. Huxley. The dual effect of membrane potential on sodium conductance in the giant axon of logio. *J. Physiol*, 116:497–506, 1952.

[37] A. L. Hodgkin and A. F. Huxley. A quantitative description of membrane current and its application to conduction and excitation in nerve. *J. Physiol*, 117:500–544, 1952.

[38] A. L. Hodgkin, A. F. Huxley, and B. Katz. Measurement of current-voltage relations in the membrane of the giant axon of logio. *J. Physiol*, 116:424–448, 1952.

[39] M. Hoekstra, C. L. Mummery, A. A. M. Wilde, C. R. Bezzina, and A. O. Verkerk. Induced pluripotent stem cell derived cardiomyocytes as models for cardiac arrhythmias. *Front. Physiol.*, 3:346, 2012. doi: 10.3389/fphys.2012.00346.

[40] A. Horváth, M. D. Lemoine, A. Löser, I. Mannhardt, F. Flenner, A. U. Uzun, C. Neuber, K. Breckwoldt, A. Hansen, E. Girdauskas, H. Reichenspurner, S. Willems, N. Jost, E. Wettwer, T. Eschenhagen, and T. Christ. Low resting membrane potential and low

inward rectifier potassium currents are not inherent features of hipsc-derived cardiomyocytes. *Stem Cell Reports*, 10:822–833, 2018.

[41] E. Huethorst. *Rigid substrates negatively affect the contractility time-course of human induced pluripotent stem cell derived cardiomyocytes*. PhD thesis, 2021. (In preparation).

[42] A. F. Huxley. Muscle structure and theories of contraction. *Prog. Biophys Chem*, 7: 255–318, 1957. doi: 10.1016/s0096-4174(18)30128-8.

[43] M. J. Ivey and M. D. Tallquist. Defining the cardiac fibroblast. *Circulation Journal*, 80 (11):2269–2276, 2016. doi: 10.1253/circj.cj-16-1003.

[44] J. G. Jacot, A. D. McCulloch, and J. H. Omens. Substrate stiffness affects the functional maturation of neonatal rat ventricular myocytes. *Biophys J*, 95(7):3479–87, 2008. doi: 10.1529/biophysj.107.124545.

[45] J. Keener and J. Sneyd. *Mathematical Physiology I: Cellular Physiology*. Springer, second edition, 2009.

[46] J. Keener and J. Sneyd. *Mathematical Physiology II: Systems Physiology*. Springer, second edition, 2009.

[47] E. L. King and C. Altman. A schematic method of deriving the rate laws for enzyme-catalyzed reactions. *J. Phys. Chem.*, 1956. doi: 10.1021/j150544a010.

[48] B. S. Kirk, J. W. Peterson, R. H. Stogner, and G. F. Carey. libmesh: a c++ library for parallel adaptive mesh refinement/coarsening simulations. *Engineering with Computers*, 22(3-4):237–254, 2006. doi: 10.1007/s00366-006-0049-3.

[49] P. Kohl and P. Camelliti. Fibroblast–myocyte connections in the heart. *Heart Rhythm*, 9 (3):461–464, 2012. doi: 10.1016/j.hrthm.2011.10.002.

[50] P. Kohl, A. G. Kamkin, I. S. Kiseleva, and D. Noble. A mathematical model of electrotonic interactions between ventricular myocytes and fibroblasts. *Experimental Physiol*, 79:943 – 956, 1994. doi: 10.1113/expphysiol.1994.sp003819.

[51] S. Land, S Holohan, N. Smith, C dos Remedios, J. Kentish, and S. Niederer. A model of cardiac contraction based on novel measurements of tension development in human cardiomyocytes. *Journal of Molecular and Cellular Cardiology*, 106:68–83, 2017. doi: doi:10.1016/j.yjmcc.2017.03.008.

[52] K. A. MacCannell, H. Bazzazi, L. Chilton, Y. Shibukawa, R. B. Clark, and R. Giles W. A mathematical model of electrotonic interactions between ventricular myocytes and fibroblasts. *Biophysiol J*, 92:4121 – 4132, 2007. doi: 10.1529/biophysj.106.101410.

[53] A. Mahajan, Y. Shiferaw, D. Sato, A. Baher, R. Olcese, L. Xie amd M. Yang, P. Chen, J. G. Restrepo, A. Karma, A. Garfinkel, Z. Qu, and J. N. Weiss. A rabbit ventricular action potential model replicating cardiac dynamics at rapid heart rates. *Biophysical Journal*, 94:392–410, 2008.

[54] J. Marïn-Garcïa. *Heart Failure: Bench to Bedside*. Springer New York Dordrecht Heidelberg London, first edition, 2010.

[55] F. Martini, J. Nath, and E. Bartholomew. Pearson Education, Limited, global edition edition, 2018. URL https://ebookcentral.proquest.com/lib/gla/detail.action?docID=5186130.

[56] *MATLAB version 9.3.0.713579 (R2017b)*. The Mathworks, Inc., Natick, Massachusetts, 2017.

[57] E. Matsa, P. W. Burridge, and J. C. Wu. Human stem cells for modeling heart disease and for drug discovery. *Sci. Transl. Med.*, 6(239), 2014. doi: 10.1126/scitranslmed.3008921.

[58] M. P. Maxwell, D. J. HEARSE, and D. M. YELLON. Species variation in the coronary collateral circulation during regional myocardial ischaemia: a critical determinant of the rate of evolution and extent of myocardial infarction. *Crdio Res*, 21:737–746, 1987.

[59] Michele Miragoli, Giedrius Gaudesius, and Stephan Rohr. Electrotonic modulation of cardiac impulse conduction by myofibroblasts. *Circulation Research*, 98(6):801–810, 2006. doi: 10.1161/01.res.0000214537.44195.a3.

[60] N. M. Mordwinkin, A. S. Lee, and J. C. Wu. Patient-specific stem cells and cardiovascular drug discovery. *J. of the American Med. Ass.*, 310(19):2039–2040, 2013. doi: 10.1001/jama.2013.282409.

[61] A. M. Moretti, A. Bellin, C. B. Welling, J. T. Jung, L. Lam, T. Bott-Flügel, A. Dorn, C. Goedel, F. Höhnke, M. Hofmann, D. Seyfarth, A. Sinnecker, A. Schömig, and K.-L. Laugwitz. Patient-specific induced pluripotent stem- cell models for long-qt syndrome. *N. Engl. J. Med*, 363.

[62] R. Morgan, M. Colman, M. Kruger, G. Seemann, K. Rhode, and O. Aslanidil. Evaluating effects of fibrosis in atrial arrhythmogenesis using 3d computational modelling. *Comp. in Cardiol.*, 41:765–768, 2014.

[63] R. Morgan, M. A. Colman, H. Chubb, G. Seemann, and O. V. Aslanidi. Slow conduction in the border zones of patchy fibrosis stabilizes the drivers for atrial fibrillation: Insights from multi-scale human atrial modeling. *Frontiers in Physiology*, 7(474), 2016. doi: 10.3389/fphys.2016.00474.

[64] P. Mortensen, M. H. B. N. Aziz, H. Gao, and R. Simitev. Modelling and simulation of electrical propagation in transmural slabs of scarred left ventricle tissue. In *6th European Conference on Computational Mechanics (ECCM 6), 11–15 June 2018, Glasgow*, 2018.

[65] P. Mortensen, H. Gao, G. Smith, and R. Simitev. Action potential propagation and block in a model of atrial tissue with myocyte-fibroblast coupling. *Mathematical Medicine and Biology*, 2021. doi: 10.1093/imammb/dqaa014.

[66] R. Myles. *The relationship between repolarisation alterans and the production of ventricular arrhythmia in heart failure*. PhD thesis, University of Glasgow, 2009.

[67] R. Myles, O. Bernus, F. Burton, S. Cobbe, and G. L. Smith. Effect of activation sequence on transmural patterns of repolarization and action potential duration in rabbit ventricular myocardium. *American Journal of Physiology-Heart and Circulatory Physiology*, 299 (6):1812–1822, 2010. doi: 10.1152/ajpheart.00518.2010. URL https://doi.org/10.1152/ajpheart.00518.2010.

[68] A. R. Nayak, T. K. Shajahan, A. V. Panfilov, and R. Pandit. Spiral-wave dynamics in a mathematical model of human ventricular tissue with myocytes and fibroblasts. *PLoS ONE*, 8(9):e72950, 2013. doi: 10.1371/journal.pone.0072950.

[69] T. P. Nguyen, Y. Xie, A. Garfinkel, Z. Qu, and J. N. Weiss. Arrhythmogenic consequences of myofibroblast–myocyte coupling. *Cardiovascular Research*, 93:242–251, 2012. doi: doi:10.1093/cvr/cvr292.

[70] T. P. Nguyen, Z. Qu, and J. N. Weiss. Cardiac fibrosis and arrhythmogenesis: The road to repair is paved with perils. *J Mol Cell Cardiol*, 70:83–91, 2014. doi: 10.1016/j.yjmcc.2013.10.018.

[71] S. A. Niederer, E. Kerfoot, A. P. Benson, M. O. Bernabeu, O. Bernus, C. Bradley, E. M. Cherry, R. Clayton, F. H. Fenton, A. Garny, E. Heidenreich, S. Land, M. Maleckar, P. Pathmanathan, G. Plank, J. F. Rodriguez, I. Roy, F. B. Sachse, G. Seemann, O. Skavhaug, and N. P. Smith. Verification of cardiac tissue electrophysiology simulators using an n-version benchmark. *Philosophical Transactions of the Royal Society A: Mathematical, Physical and Engineering Sciences*, 369(1954):4331–4351, 2011. doi: 10.1098/rsta.2011.0139.

[72] D. Noble. Cardiac action and pacemaker potentials based on the hodgkin-huxley equations. *Nature*, 188:495 –497, 1960.

[73] D. Noble. A modification of the hodgkin—huxley equations applicable to purkinje fibre action and pacemaker potentials. *Journal of Physiology*, 160(2):317–352, 1962.

[74] *The NAG Fortran Library Manual — Mark 21*. The Numerical Algorithms Group Ltd., Wilkinson House, Jordan Hill Rd, Oxford, OX2 8DR, 2005. URL http://www.nag.co.uk/numeric/fl/manual/html/FLlibrarymanual.asp.

[75] M. Paci, J. Hyttinen, K. Aalto-Setälä, and S. SeverI. Computational models of ventricular- and atrial-like human induced pluripotent stem cell derived cardiomyocytes. *A of Biomed Eng*, 41(11):2334–2348, 2013. doi: 10.1007/s10439-013-0833-3.

[76] P. Pandey, W. Hawkes, J. Hu, W. V. Megone, J. Gautrot, N. Anilkumar, M. Zhang, L. Hirvonen, S. Cox, E. Ehler, J. Hone, M. Sheetz, and T. Iskratsch. Cardiomyocytes sense matrix rigidity through a combination of muscle and non-muscle myosin contractions. *Dev Cell*, (3):326–336, 2018. doi: 10.1016/j.devcel.2017.12.024.

[77] J. Pellman, J. Zhang, and F. Sheikh. Myocyte-fibroblast communication in cardiac fibrosis and arrhythmias: Mechanisms and model systems. *J Mol Cell Cardiol*, 94:22–31, 2016. doi: 10.1016/j.yjmcc.2016.03.005.

[78] W. H. Press, S. A. Teukolsky, W. T. Vetterling, and B. P. Flannery. *Numerical Recipes in C*. Cambridge University Press, second edition, 1992.

[79] L Qiao. *Development of Cellular and Tissue Models to Simulate the Effect of Fibroblast-Myocyte Coupling on Cardiac Pacemaking and Conduction*. PhD thesis, School of Physics and Astronomy, 2016.

[80] Z. Qu and A. Garfinkel. An advanced algorithm for solving partial differential equation in cardiac conduction. *IEEE Transactions on Biomedical Engineering*, 46:1166–1168, 1999. doi: 10.1109/10.784149.

[81] W. Rall. Membrane time constant of motoneurons. *Science*, 126:454, 1957. doi: 10.1126/science.126.3271.454.

[82] W. Rall. Branching dendritic trees and motoneuron membrane resistivity. *Experimental Neurology*, 1:454, 1959. doi: 10.1016/0014-4886(59)90046-9.

[83] W. Rall. Membrane potential transients and membrane time constant of motoneurons. *Experimental Neurology*, 2:491 – 527, 1960. doi: 10.1016/0014-4886(60)90029-7.

[84] W. Rall. Time constants and electronic length of membrane cylinders and neurons. *Biophysical Journal*, 9:1483–1508, 1969. doi: 10.1016/S0006-3495(69)86467-2.

[85] S. Ramadan and N. Paul H. E. Naguib. Standardized static and dynamic evaluation of myocardial tissue properties. *Biomed Mater*, 12(2):025013, 2017. doi: 10.1088/1748-605X/aa57a5.

[86] A. J. S. Ribeiro, Y. S. Ang, J. D. Fu, R. N. Rivas, T. M. A. Mohamed, G. C. Higgs, D. Srivastava, and B. L. Pruitt. Contractility of single cardiomyocytes differentiated from pluripotent stem cells depends on physiological shape and substrate stiffness. *Proc Natl Acad Sci*, 112(41):12705–12710, 2015. doi: 10.1073/pnas.1508073112.

[87] M. C. Ribeiro, R. H. Slaats, V. Schwach, J. M. Rivera-Arbelaez, L. G. J. Tertoolen, B. J. van Meer, R.t Molenaar, C. L. Mummery, M. M. A. E. Claessens, and R. Passier. A cardiomyocyte show of force: A fluorescent alpha-actinin reporter line sheds light on human cardiomyocyte contractility versus substrate stiffness. *J Mol Cell Cardiol*, 141: 54–64, 2020. doi: 10.1016/j.yjmcc.2020.03.008.

[88] J. J. Rice, D. M. Bers F. Wang, and P. P. de Tombe. Approximate model of cooperative activation and crossbridge cycling in cardiac muscle using ordinary differential equations. *Biophysical Journal*, 95:2368–2390, 2008.

[89] W. J. Richardson, S. A. Clarke, T. A. Quinn, and J. W. Holmes. Physiological implications of myocardial scar structure. *Comprehensive Physiology*, page 1877–1909, 2015. doi: 10.1002/cphy.c140067.

[90] W. J. Richardson, S. A. Clarke, T. A. Quinn, and J. W. Holmes. Physiological implications of myocardial scar structure. *Compr Physiol*, 5:1877–1909, 2016. doi: 10.1002/cphy.c140067.

[91] M. Rienks, A. Papageorgiou, N. G. Frangogiannis, and S. Heymans. Myocardial extracellular matrix: An ever-changing and diverse entity. *Circ Res*, 114:872–888, 2014. doi: 10.1161/CIRCRESAHA.114.302533.

[92] A. G. Rodriguez, S. J. Han, M. Regnier, and N. J. Sniadecki. Substrate stiffness increases twitch power of neonatal cardiomyocytes in correlation with changes in myofibril structure and intracellular calcium. *Biophys J*, (10):2455–2464, 2011. doi: 10.1016/j.bpj.2011.09.057.

[93] S. Rossi and B. Griffith. Incorporating inductances in tissue-scale models of cardiac electrophysiology. *Chaos: An Interdisciplinary Journal of Nonlinear Science*, 27(9): 093926, 2017.

[94] F. A. Sachse. *Computational Cardiology*. Springer, Berlin, Heidelberg, Salt Lake City, UT, 2004. doi: 10.1007/b96841.

[95] L. Sala, B. J. van Meer, L. G. J. Tertoolen, J. Bakkers, M. Bellin, R. P. Davis, C. Denning, M. A. E. Dieben, T. Eschenhagen, E. Giacomelli, C. Grandela, A. Hansen, E. R. Holman, M. R. M. Jongbloed, S. M. Kamel, C. D. Koopman, Q. Lachaud, I. Mannhardt, M. P. H. Mol, D. Mosqueira, V. V. Orlova, R. Passier, M. C. Ribeiro, U. Saleem, G. L. Smith,

F. L. Burton, and C. L. Mummery. Musclemotion. *Circulation Research*, 122(3):e5–e16, 2018. doi: 10.1161/CIRCRESAHA.117.312067.

[96] A. M. Samarel. Costameres, focal adhesions, and cardiomyocyte mechanotransduction. *Am J Physiol Heart Circ Physiol*, 289(6):H2291–H2301, 2005. doi: 10.1152/ajpheart.00749.2005.

[97] R. Santoro, G. L. Perrucci, A. Gowran, and G. Pompilio. Unchain my heart: Integrins at the basis of ipsc cardiomyocyte differentiation. *Stem Cells Int*, 2019. doi: 10.1155/2019/8203950.

[98] G. Savarese and L. H. Lund. Global public health burden of heart failure. *Card Fail Rev*, 3(1), 2017. doi: 10.15420/cfr.2016:25:2.

[99] L. F. Shampine and M. W. Reichelt. The matlab ode suite. *SIAM Journal on Scientific Computing*, 18:1–22, 1997.

[100] T. R. Shannon, F. Wang, J. Puglisi, C. Weber, and D. M. Bers. A mathematical treatment of integrated ca dynamics within the ventricular myocyte. *Biophysical Journal*, 87:3351–3371, 2004.

[101] R. D. Simitev and V. N. Biktashev. Conditions for propagation and block of excitation in an asymptotic model of atrial tissue. *Biophys J*, 90:2258 – 2269, 2006. doi: 10.1529/biophysj.105.072637.

[102] R. D. Simitev and V. N. Biktashev. An analytically solvable asymptotic model of atrial excitability. In Deutsch et al., editor, *Mathematical Modeling of Biological Systems, Volume II*, pages 289–302. Birkhaeuser Boston, 2008. doi: 10.1007/978-0-8176-4556-4_26.

[103] R. D. Simitev and V. N. Biktashev. Asymptotics of conduction velocity restitution in models of electrical excitation in the heart. *Bulletin of Mathematical Biology*, 73(1):72–115, 2011. doi: 10.1007/s11538-010-9523-6.

[104] C. A. Souders, S. L. K. Bowers, and T. A. Baudino. Cardiac fibroblast: the renaissance cell. *Circulation Research*, 105(12):1164–1176, 2009. doi: 10.1161/CIRCRESAHA.109.209809.

[105] T. M. Spencer, R. F. Blumenstein, K. M. Pryse, S. Lee, D. A. Glaubke, B. E. Carlson, E. L. Elson, and G. M. Genin. Fibroblasts slow conduction velocity in a reconstituted tissue model of fibrotic cardiomyopathy. *ACS Biomater Sci Eng*, 3:3022 – 3028, 2017. doi: doi:10.1021/acsbiomaterials.6b00576.

[106] S. Sridhar, N. Vandersickel, and A. V. Panfilov. Effect of myocyte-fibroblast coupling on the onset of pathological dynamics in a model of ventricular tissue. *Sci Reports*, 2017. doi: 10.1038/srep40985.

[107] A. Stevens and J. S. Lowe. *Human Histology*. London, Mosby, second edition, 1997.

[108] G. Strang. On the construction and comparison of difference schemes. *SIAM J. Numer. Anal.*, 5:506–517, 1968. doi: 10.1137/0705041.

[109] J. Sundnes, G. T. Lines, X. Cai, B. F Nielsen, K. Mardal, and A. Tveito. *Computing the Electrical Activity in the Heart*. Springer Berlin Heidelberg, 2006. doi: 10.1007/3-540-33437-8.

[110] K. H. W. J. ten Tusscher and A. V. Panfilov. Alternans and spiral breakup in a human ventricular tissue model. *Am J Physiol Heart Circ Physiol*, 291:H1088–H1100, 2006.

[111] K. H. W. J. ten Tusscher, D. Noble, P. J. Noble, and A. V. Panfilov. A model for human ventricular tissue. *American Journal of Physiology-Heart and Circulatory Physiology*, 286(4):H1573–H1589, 2004. doi: 10.1152/ajpheart.00794.2003.

[112] P. Thomas and T. Smart. Hek293 cell line: A vehicle for the expression of recombinant proteins. *J of Pharma and Toxico Methods*, 51:187–200, 2005. doi: 10.1016/j.vascn.2004.08.014.

[113] J. M. T. Thompson, P. Kohl, D. Noble, R. L Winslow, and P. J. Hunter. Computational modelling of biological systems: tools and visions. *Philosophical Transactions of the Royal Society of London. Series A: Mathematical, Physical and Engineering Sciences*, 358(1766):579–610, 2000. doi: 10.1098/rsta.2000.0547.

[114] K. Thygesen, J. S. Alpert, A. S. Jaffe, M. L. Simoons, B. R. Chaitman, and H. D. White. Third universal definition of myocardial infarction. *Circ*, 126:2020–2035, 2012. doi: 10.1161/CIR.0b013e31826e1058.

[115] A. N. Tikhonov. Systems of differential equations, containing small parameters at the derivatives. *Mat. Sbornik*, 31(3):575–586, 1952.

[116] V. Timmermann, A. G. Edwards, S. T. Wall, 3 J.oakim Sundnes, 2, and Andrew D. McCulloch3. Arrhythmogenic current generation by myofilament-triggered ca2d release and sarcomere heterogeneity. *Biophys J*, 117:2471–2485, 2019. doi: 10.1016/j.bpj.2019.11.009.

[117] J. G. Travers, F. A. Kamal, J. Robbins, K. E. Yutzey, and B. C. Blaxall. Cardiac fibrosis. *Circulation Research*, 118(6):1021–1040, 2016. doi: 10.1161/CIRCRESAHA.115.306565.

[118] S. W. M. van den Borne, J. Diez, M. Blankesteijn, J. Verjans, L. Hofstra, and J. Narula. Myocardial remodeling after infarction: the role of myofibroblasts. *Nat Rev Cardiol*, 7 (1):30–37, 2010. doi: 10.1038/nrcardio.2009.199.

[119] A. O. Verkerk, C. C. Veerman, J. G Zegers, I. Mengarelli, C. R Bezzina, and R. Wilders. Patch-clamp recording from human induced pluripotent stem cell-derived cardiomyocytes: Improving action potential characteristics through dynamic clamp. *Int. J. Mol. Sci.*, 18(9), 2017. doi: 10.3390/ijms18091873.

[120] M. Ward and T. Iskratsch. Mix and mismatch - the mechanosensing machinery in the changing environment of the developing, healthy adult and diseased heart. *Biochim Biophys Acta Mol Cell Res*, 1867(3):118436, 2020.

[121] Y. Xie, A. Garfinkel, P. Camelliti, P. Kohl, J. N. Weiss, and Z. Qu. Effects of fibroblast-myocyte coupling on cardiac conduction and vulnerability to reentry: A computational study. *Heart Rhythm*, 6(11):1641–1649, 2009. doi: 10.1016/j.hrthm.2009.08.003.

[122] Y. Xie, A. Garfinkel, J. N. Weiss, and Z Qu. Cardiac alternans induced by fibroblast-myocyte coupling: Mechanistic insights from computational models. *AJP Heart Circ Physiol*, 297:H775 – H783, 2009. doi: 30.209.236.096.

[123] K. Yamamura, D. Yuen, E. J Hickey, X. He, R. R Chaturvedi, M. K Friedberg, L. Grosse-Wortmann, K. Hanneman, F. Billia, M. E Farkouh, and R. M Wald. Electrotonic myofibroblast-to-myocyte coupling increases propensity to reentrant arrhythmias in two-dimensional cardiac monolayers. *Heart*, 108:855–863, 2018. doi: 10.1136/heartjnl-2018-313961.

[124] S. Yonemura, Y. Wada, T. Watanabe, A. Nagafuchi, and M. Shibata. α-catenin as a tension transducer that induces adherens junction development. *Nat Cell Biol*, 12(6): 533–42, 2010.